Trapping Ultracold Atoms in Submicron Period Magnetic Lattices

Tien Duy Tran

Presented in fulfillment of the requirements

of the degree of Doctor of Philosophy

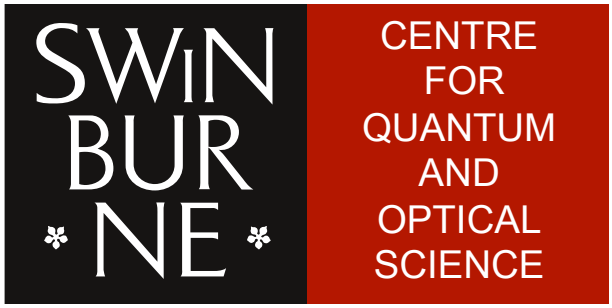

Centre for Quantum and Optical Science

Faculty of Science, Engineering and Technology

Swinburne University of Technology

Melbourne, Australia

May 2018

"Imagination is more important than knowledge. Knowledge is limited. Imagination encircles the world."

Albert Einstein

Abstract

Periodic arrays of magnetic microtraps patterned on a magnetic film provide a potential complementary tool to conventional optical lattices. Such magnetic lattices allow a high degree of design flexibility, low technical noise and state-selective trapping of atoms. This thesis reports the trapping of ultracold ^{87}Rb atoms in 0.7 μm-period triangular and square magnetic lattices integrated on an atom chip as a step towards using magnetic lattices as a platform for simulating condensed matter and quantum many-body phenomena in nontrivial lattice geometries.

The new generation sub-micron period magnetic lattices are produced by patterning a Co/Pd multi-atomic layer magnetic film deposited on a silicon substrate using electron-beam lithography and reactive ion-etching. The magnetic microstructures include 0.7 μm-period 2D square and triangular lattices and 1D 0.7 μm-period and 5 μm-period lattices. The four magnetic microstructures are mounted on an atom chip containing two Z-shaped and two U-shaped current-carrying wires fabricated by chemical etching on a direct bonded copper (DBC) board. The current-carrying wires are required for initial preparation of the ultracold ^{87}Rb atoms, allowing the creation of a Bose-Einstein condensate in a Z-wire trap and loading into the magnetic lattice.

The magnetic lattice potential is produced by applying a bias magnetic field to the magnetic lattice structures which in the case of the 0.7 μm-period lattice produce extremely tight magnetic microtraps with trap frequencies up to about 800 kHz and trap bottoms at estimated distances down to about 90 nm from the chip surface. The atom-surface interaction is studied by measuring the atom loss when atoms in the Z-wire magnetic trap are brought to various distances very close to the chip surface. The interaction of the atoms with the magnetic trapping potential is investigated by launching the Z-wire trap cloud vertically towards the magnetic lattice structures under different bias magnetic fields.

The key results presented in this thesis are the successful loading of ultracold atoms into the 0.7 μm-period 2D triangular and square magnetic lattices. The mea-

sured trap lifetimes range from 0.4 to 2.5 ms, and increase approximately linearly with increasing distance from the chip surface. The relatively short trap lifetimes are attributed mainly to losses due to surface-induced thermal evaporation when loading into the tight magnetic lattice traps rather than to fundamental loss processes such as three-body recombination or spin-flips due to Johnson noise from the chip surface. The Casimir-Polder interaction starts to become significant at distances less than about 100 nm from the chip surface.

To the best of my knowledge, these results represent the first reported realization of trapping of atoms in a sub-micron period magnetic lattice. This is considered to be a significant step towards employing magnetic lattices for the simulation of condensed matter and many-body phenomena in nontrivial lattice geometries.

Acknowledgements

This thesis could not have been completed without constant help and support from my colleagues, friends and family members and now, with a grateful heart, I would like to express my appreciation to all of them.

First and foremost, my sincerest gratitude is to my supervisor Emeritus Professor Peter Hannaford who has provided valuable guidance and encouragement, as well as constant motivations to me throughout my research. I will always remember his helping hand from my very first steps in the PhD program to the final writing of this thesis. I feel truly lucky to have the opportunity to do my PhD studies under his supervision.

Next, I wish to say thank you to my co-supervisor Professor Russell McLean and Professor Andrei Sidorov for all of their involvements in my research. Without their precious discussions, suggestions and contributions, I doubt I could have gone this far.

I would also like to express my thanks to Prof. Saulius Juodkazis, Armandas Balcytis and Pierrette Michaux from the Centre for Micro-Photonics at Swinburne for their contributions to the fabrication of the magnetic lattice atom chip; to Prof. Shannon Whitlock at the University of Strasbourg for his fruitful suggestions and contributions to the project; to Prof. Manfred Albrecht at the Universität Augsburg, Germany for supplying the state-of-art Co/Pd multi-atomic layer film; and to Dr. James Wang for his support and guidance during the characterization of the patterned Co/Pd films.

I appreciated the help of Dr. Ivan Herrara, one of the best former postdoc fellows in our group. From the time I was very new to the lab, I have benefited so much from the experience and knowledge that Ivan has kindly passed on to me to improve the quality of my research. Besides, it would be a huge remiss without mentioning Yibo Wang, the former PhD student in our group, who has been a great colleague, as well as a close friend since I first came to the lab.

I would like to thank Professor Lap Van Dao, Dr Khuong Dinh and former PhD

students Prince Surendran, Alessandro Brolis and Smitha Jose for sharing their insightful view and critical comments on the experiments. Also, I would like to thank other people in the Centre, especially Research Support Coordinator Tatiana Tchernova for assistance with all administrative work.

Last but not least, I wish to send my sincere appreciation to my family for all their love and support. Their encouragement, advice and guidance has been invaluably precious from the very early stage of my studies.

Declaration

The work presented in this thesis entitled "Trapping Ultracold Atoms in Submicron Period Magnetic Lattices" has been carried out in the Centre for Quantum and Optical Science (CQOS) at Swinburne University of Technology in Melbourne, Australia between October 2014 and May 2018. The thesis contains no material that has been accepted for the award of any other degree or diploma. To the best of my knowledge, the thesis contains no material previously published or written by another author, except where due reference is made in the text of the thesis.

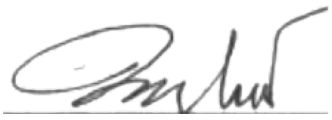

Tien Duy Tran

Melbourne, Victoria, Australia

27 August 2018

Contents

List of Figures

List of Tables

CHAPTER 1

Introduction

1.1 Introduction to magnetic lattices

In atomic physics, quantum simulation with ultracold atoms is currently one of the most promising methods to better understand unsolved quantum Hamiltonian systems and other complex phenomena in many-body physics at the quantum scale. In recent years, ultracold atoms trapped in periodic lattices have attracted much attention as a simulator for condensed matter systems because of the ability to confine, manipulate and precisely control the ultracold atoms [1]. Thanks to advances in the controllability of experimental parameters such as dimensionality, atomic interactions, level of purity, disorder, etc., experiments on ultracold quantum gas systems have opened the way to simulate the behaviour of complex systems that are normally difficult to control and understand.

Following the discovery of laser cooling and trapping techniques in the 1980s [2–4], optical lattices produced by interfering laser fields have been used extensively to trap periodic arrays of ultracold atoms and quantum degenerate gases, including Bose-Einstein condensates and degenerate Fermi gases. Applications of optical lattices range from quantum simulations of exotic condensed matter phenomena [5] to high precision atomic clocks [6], quantum gas microscopes [7] and storage registers and

quantum gates for quantum information processing [8,9]. One advantage of an optical lattice system is the high controllability of system parameters including geometric lattice structures and interaction between the particles, which make it an attractive system to study condensed matter phenomena such as Josephson junctions [10], the quantum Hall effect [11], Anderson localization [12,13], the superfluid to Mott insulator transition [5], low-dimensional quantum systems [14,15] and the Ising spin model [16]. Despite their broad range of applications, optical lattices still have certain limitations such as a low degree of design flexibility, difficulty in generating arbitrary trap geometries, restrictions on the lattice spacing imposed by the optical wavelength, presence of spontaneous emission, non-uniformity, scalability, etc. [17].

Trapping of periodic arrays of ultracold atoms can also be performed using lattices consisting of periodic arrays of magnetic microtraps. Such magnetic lattices can be created in various ways including patterning a periodic array of current-carrying wires [18–20] and patterning permanent magnetic films [17,21–35] or by producing vortex arrays of superconducting films [36], pulsed gradient magnetic fields [37,38] and nano-magnetic domain walls [39].

Investigations have demonstrated that magnetic lattices created by permanent magnetic microstructures on an atom chip can provide a potentially powerful alternative approach to optical lattices for trapping periodic arrays of ultracold atoms and quantum degenerate gases [24]. For magnetic lattices, the trap geometries and lattice spacing are not restricted by the requirement of interfering laser fields or by the optical wavelength, which consequently makes it possible in principle to generate almost arbitrary trap geometries and lattice periods [28]. Additionally, magnetic lattices have highly stable trapping potentials, they have inherently no spontaneous emission, low heating rates and low technical noise, and they are ideally suited for mounting on an atom chip [40]. Importantly, atoms trapped in magnetic lattices are state-selected which allows radiofrequency evaporative cooling to be carried out in the lattice itself and the trapped atoms in the lattice to be characterized by radio frequency spectroscopy [26,33]. Such characteristics make magnetic lattices involving ultracold bosonic or fermionic atoms potentially attractive to simulate

condensed matter phenomena such as the superfluid to Mott insulator quantum phase transition [5, 41] and graphene-like states in honeycomb magnetic lattices.

1.2 Review of one-dimensional and two-dimensional magnetic lattices

After the first magnetic traps to confine neutral atoms were reported in 1985 by Midgall *et al.* [42] and Lovelace *et al.* [43], Opat *et al.* [44] in 1992 proposed the use of a periodic array of magnets of alternating polarity and a periodic array of current-carrying wires as magnetic mirrors for reflecting beams of laser cooled atoms. In 1995, Roach *et al.* [45] demonstrated the retroflection of laser-cooled rubidium atoms from a periodically magnetized audiotape. In 1996, Sidorov *et al.* [46] observed specular reflection and multiple bounces of laser-cooled caesium atoms from a magnetostatic mirror based on a periodic array of rare-earth magnets with a period of 2 mm.

In 1998, Sidorov *et al.* [47] reported the fabrication of a grooved 10 μm period magnetic structure using electron beam lithography. This structure exhibits the same magnetic field pattern as a periodic array of magnets of alternating polarity proposed by Opat *et al.* [44], but it permits the fabrication of small micron-scale period magnetic structures. In 1999, a periodic magnetic mirror fabricated using optical lithography was reported by Lau *et al.* [48]. This mirror was based on an array of current-carrying conductors of periodicity 330 μm mounted on a silicon wafer. As all wires in the array carry the same current, the magnetic flux created by this magnetic mirror should in principle be more uniform allowing the creation of a flatter mirror for reflection than a magnetostatic mirror. Additionally, through adjustment of the current, the mirror can be rapidly switched on or off or modulated.

By applying a suitable uniform bias field, a magnetic mirror can be turned into a one-dimensional lattice of magnetic microtraps through the interference with the rotating magnetic field of the periodic array. In 2002, Yin *et al.* [18] proposed two

schemes for creating 1D and 2D periodic arrays of magnetic microtraps using a static magnetic field from current-carrying wires. In 2003, another 2D array trapping scheme using two overlayed layers of crossed current-carrying wires was proposed by Grabowski and Pfau [49]. In 2006, the Swinburne group [50] proposed a scheme to create 1D and 2D magnetic lattices using periodic arrays of permanent magnetic films. By applying bias magnetic fields to periodic arrays of magnetic films, a 2D square magnetic lattice with non-zero potential minima can be created using two crossed layers of parallel rectangular magnets and also by utilizing a single layer of square-shaped magnets with three different thicknesses. In the same year, Yun and Yin [51] proposed a scheme to produce 2D arrays of magnetic traps with non-zero potential minima using current-carrying conductors with the ability to vary the barrier height.

In 2005, a periodic array of 1D magnetic traps with a period of 106 μm was created by Sinclair *et al.* [52] using a sinusoidally magnetized videotape plus bias fields. The group successfully produced a Bose Einstein condensate (BEC) in a one of the traps. In 2007, the MIT group [53] produced a 1D periodic array of magnetic traps from a CoCrPt magnetic film on a hard disk platter written with a period of 100 μm. This group successfully produced a BEC in one of the traps and demonstrated a method to detect imperfections in the trapping potential using BECs.

In 2008, Singh *et al.*, from our Swinburne group successfully trapped ^{87}Rb atoms in the $|F = 2, m_F = 2\rangle$ low-field seeking state in $\sim$ 150 sites of a 10 μm-period 1D magnetic lattice comprising a grooved TbGdFeCo permanent magnetic film mounted on a current-carrying wire structure atom chip plus a bias field [22]. They subsequently studied the dynamics and the effect of temperature on the reflection of ultracold atoms from the trapping potential [54, 55]. Meanwhile, in 2007, a 2D rectangular magnetic lattice with 22 μm and 36 μm spacing in orthogonal directions was created by the Amsterdam group [25]. ^{87}Rb atoms in the $|F = 2, m_F = 2\rangle$ state were successfully trapped in multiple sites at about 10 μm from the surface with a trap lifetime of more than 1 second. In 2009, the atoms were loaded into

more than 500 lattice sites and further cooled to near the critical temperature for condensation [26]. However, they were unable to reach BEC due to large three-body recombination losses.

In 2014 and 2015, Jose *et al*. [32] and Surendran *et al*. [33] from our group successfully produced a 1D periodic array of BECs across ∼100 lattice sites using the above TbGdFeCo magnetic lattice [22] by preparing ^{87}Rb atoms in the $|F = 1, m_F = -1\rangle$ low-field seeking state and providing additional axial confinement for the lattice traps. Use of the $|F = 1, m_F = -1\rangle$ state helps to reduce the three-body loss rate of atoms in the traps by up to three times and also allows the confining traps to be less tight [56, 57]. *In situ* RF spectra measurement of ultracold atoms in individual lattice sites showed the evolution from a thermal Boltzmann distribution to a pronounced bimodal distribution consisting of a narrow BEC distribution plus a thermal cloud as the atom clouds were cooled in the lattice to lower temperature. The RF spectra measurement also indicated a remarkable uniformity across the magnetic lattice, with small site-to-site variations of atom temperature, condensate fraction, chemical potential, atom number and trap bottom [33].

In 2010, Schmied *et al*. [28] introduced an algorithm for designing various periodic arrays of magnetic traps based on patterned magnetic films. This code can produce desired lattice geometries with optimized properties in both 2D and 1D, and generates output that is straightforward for fabrication, overcoming the complexity of design and fabrication in earlier proposals [24, 50]. Using this algorithm, in 2011 the Amsterdam group fabricated 10 μm-period square and triangular magnetic lattices for trapping ^{87}Rb atoms [30]. The lattice structure was fabricated using UV lithography on a FePt magnetic film. In 2014, the same group successfully loaded atoms into hundreds of sites in these lattices [34]. In 2015, our Swinburne group fabricated 0.7 μm-period 1D and 2D triangular and square magnetic lattice structures using electron-beam lithography and reactive ion etching techniques [17]. Such magnetic lattices with sub-micron period are designed for quantum tunnelling experiments such as the simulation of Hubbard physics [1].

1.3 Overview of thesis

In previous works of our group, a one-dimensional magnetic lattice structure with a period of 10 μm [22, 32, 33] was used. However, according to our calculations, the quantum tunnelling time of atoms between lattice sites would be much too long compared with the lifetime of the atoms in the lattice traps. In order to perform quantum tunnelling experiments, it is required to use magnetic lattice structures with submicron periods.

This thesis reports the loading and trapping of ultracold ^{87}Rb $|F = 1, m_F = -1\rangle$ atoms in a 0.7 μm-period triangular magnetic lattice and a 0.7 μm-period square magnetic lattice on an atom chip at a distances down to $\sim$ 90 nm from the chip surface. This represents new territory for trapping ultracold atoms. The trapping in the triangular magnetic lattice has recently been published in [35].

The lattice trapping experiment was performed on the modified laser optical setup built by former students in our group: Mandip Singh, Smitha Jose, Prince Surrendran and Yibo Wang [58–61]. The Direct Bonded Copper atom chip and the sub-micron magnetic lattice film were designed by Dr. Ivan Herrera and Yibo Wang and fabricated by Armandas Balcytis from the Centre for Micro-Photonics at Swinburne University of Technology [17]. The characterization of the fabricated magnetic film and the installation of the atom chip and sub-micron period magnetic lattice film was carried out jointly with Yibo Wang. My independent personal contribution to the magnetic lattice trapping experiments is that I created different protocols for successful trapping ^{87}Rb in the sub-micron period magnetic lattice and realized the trapping of ultracold atoms in the sub-micron period magnetic lattice as reported in the paper [35] and in this thesis (Figures 5.8, 5.9, 5.10, 5.11, 5.12, 5.16, 5.17).

The layout of the thesis is as follows:

Chapter 2 summarizes the theoretical background relevant for the interpretation of the experimental results. The atom-surface interaction when an atom cloud is trapped close to a surface is discussed. In the final part, the theoretical framework

for the design of a sub-micron period 2D magnetic lattice is presented.

Chapter 3 presents the design and fabrication of the magnetic lattice atom chip including the patterned Co/Pd magnetic film and the Direct Bonded Copper (DBC) atom chip. The characterization and quality test results of the fabricated microstructures are described. Additionally, the fabrication of an improved new generation direct bonded copper atom chip for future experiments is presented.

Chapter 4 presents the experiment setup including the laser setup, the ultra-high vacuum chamber, the electronic control system and the experimental procedure to obtain Bose Einstein condensation in the Z-wire magnetic trap used to load the magnetic lattices.

Chapter 5 reports the experimental results for the trapping of ultracold ^{87}Rb atoms in the 0.7 μm-period triangular and square magnetic lattices at a distances down to $\sim$ 90 nm from the surface of the atom chip. These are the key results of the thesis.

Chapter 6 summarizes the work and discusses some possible experiments for the future.

CHAPTER 2

Theoretical background

This chapter describes the theoretical background for the trapping of ultracold atoms in a magnetic lattice atom chip and for producing Bose-Einstein condensation. Also, the atom-surface interactions and the theoretical framework for creating submicron-period 2D magnetic lattices are discussed. My calculations shown as simulated plots and tables in this chapter were performed using Mathematica software.

2.1 Trapping of neutral atoms in a magnetic field

The potential energy of an atom in an inhomogeneous magnetic field is given by:

$$U(x, y, z) = -\mu_B g_F m_F |B(x, y, z)|, \tag{2.1}$$

where (x, y, z) is the position of the atom in the magnetic field, m_F is the magnetic quantum number, g_F is the Landé g-factor of the atomic state $|F, m_F\rangle$ and μ_B is the Bohr magneton. For a field gradient $\nabla|B(x, y, z)|$, the atom experiences a Stern-Gerlach force:

$$F(x, y, z) = \mu_B g_F m_F \nabla|B(x, y, z)|. \tag{2.2}$$

• If $m_F g_F > 0$, the atom is in a weak-field seeking state. In this state, the atom experiences a potential minimum, which increases with increasing magnetic

field strength allowing it to be trapped. For ^{87}Rb atoms, the trappable states are $|F = 1, m_F = -1\rangle$, $|F = 2, m_F = 2\rangle$ and $|F = 2, m_F = 1\rangle$.

• If $m_F g_F < 0$, the atom is in a high-field seeking state and experiences a driving force toward the higher magnetic field regions. In this state, there is no trapping since the potential energy of the atom is higher than the local field minimum. As according to Maxwell's equation it is not possible to create a local magnetic field maximum in free space [62], we require a magnetic field minimum to trap atoms in a magnetic trap. This can be done with a configuration consisting of a pair of parallel anti-Helmholtz coils which creates a quadrupole trap with a zero-field minimum. This setup can produce a magnetic field strength $|B(x, y, z)|$ that increases linearly in all directions.

• If $m_F g_F = 0$, there is no interaction to first order between the atom and the magnetic field.

When confined in a magnetic trap, an atom oscillates around the local trap minimum of the magnetic field experiencing a change in the field direction and magnitude. If the atom's magnetic moment does not adiabatically follow the field direction, this will induce atom loss due to flipping to other magnetic states. Thus, for stable trapping, it is required not only that the trap depth is much larger than the thermal energy of the atom but also that the precessing atomic spin should adiabatically follow the change in the magnetic field direction. In order to satisfy the adiabatic condition, the rate of change $\frac{d\theta}{dt}$ of the field's direction needs to be slower than the precession in the magnetic field [63]:

$$\frac{\mathrm{d}\theta}{\mathrm{d}t} \ll \omega_L = \frac{g_F m_F \mu_B B}{\hbar}, \tag{2.3}$$

where ω_L is the Larmor frequency at which the magnetic moment of the atom precesses around the magnetic field.

In a region of zero or small magnetic field, the adiabatic condition is violated. In these regions, the change in the atom's precession angle induces transitions between m_F levels, which can transfer atoms to untrappable states so that they become lost [64]. Thus, to avoid Majorana spin flips it is important to trap atoms in a

magnetic field pattern in which a non-zero trap minimum can be maintained [65].

Spin-flip losses are the main drawback of a quadrupole trap, which has a zero-field minimum and cannot be used for stable magnetic trapping. One way to overcome this problem is to use an Ioffe-Pritchard trap with a non-zero minimum. For Ioffe-Pritchard traps, the probability of an atom having a Larmor frequency smaller than the orbital frequency at the non-zero trap minimum is dramatically reduced. These traps usually contain four current-carrying bars and two pinch coils. The 2D quadrupole field created by the bars and the non-uniform field created by the coils can produce a 3D trap with a magnetic field minimum B_0. It is required to provide a magnetic field minimum large enough for stable trapping since the spin-flip transition rate is significantly reduced thanks to the large Larmor frequency.

A cloud of spin-half trapped atoms with a thermal Boltzmann distribution at temperature T has a spin-flip transition rate [66]:

$$\Gamma = 2\pi\omega \tanh\left(\frac{\hbar\omega}{2k_BT}\right) \exp\left[-\frac{2E_0}{\hbar\omega}\tanh\left(\frac{\hbar\omega}{2k_BT}\right)\right], \tag{2.4}$$

where ω is the trap oscillator frequency for negligible axial confinement, k_f is the momentum of the final state and $E_0 = \hbar^2 k_f^2/2m = 2\mu_B B_0 + \hbar\omega$ is the kinetic energy of the atom after a spin-flip transition occurs and. At the high temperature limit $k_BT \gg 2\hbar\omega$, the spin-flip transition rate reduces to:

$$\Gamma \approx \left(\frac{\hbar\omega^2}{k_BT}\right) \exp[-\frac{E_0}{k_BT}]. \tag{2.5}$$

2.2 Magnetic trapping of neutral atoms on an atom chip

The basic trapping potential is created by passing a DC current I through a straight wire and adding a constant homogeneous bias field $\boldsymbol{B}_b$ perpendicular to the wire, which produces a total magnetic field:

$$\boldsymbol{B} = \boldsymbol{B}_{wire} + \boldsymbol{B}_b, \tag{2.6}$$

where $\boldsymbol{B}_{wire}$ is the magnetic field created by a infinitely thin long straight wire and μ_0 is the vacuum permeability. Due to the cancellation of the magnetic fields from the wire and the bias field, Figure 2.1 (c), the total magnetic field reaches zero at a distance $r_0 = \dfrac{\mu_0 I}{2\pi B_b}$ [67–69]. This creates a two-dimensional quadrupole trap with a zero magnetic field minimum and a field gradient [67, 69]:

$$\frac{\partial |\boldsymbol{B}|}{\partial r_0} = -\frac{\mu_0 I}{2\pi r_0^2}. \tag{2.7}$$

To avoid Majorana spin-flip loss at the zero field minimum, another magnetic field B_0 parallel to the wire is employed. This offset magnetic field also adds harmonicity to the trapping potential. The trapping frequency of an atom in this harmonic trapping potential is given by:

$$\omega = \left(\frac{2\pi}{\mu_0}\right) \frac{B_b^2}{I} \sqrt{\frac{g_F m_F \mu_B}{m B_0}}, \tag{2.8}$$

where m is the atom mass.

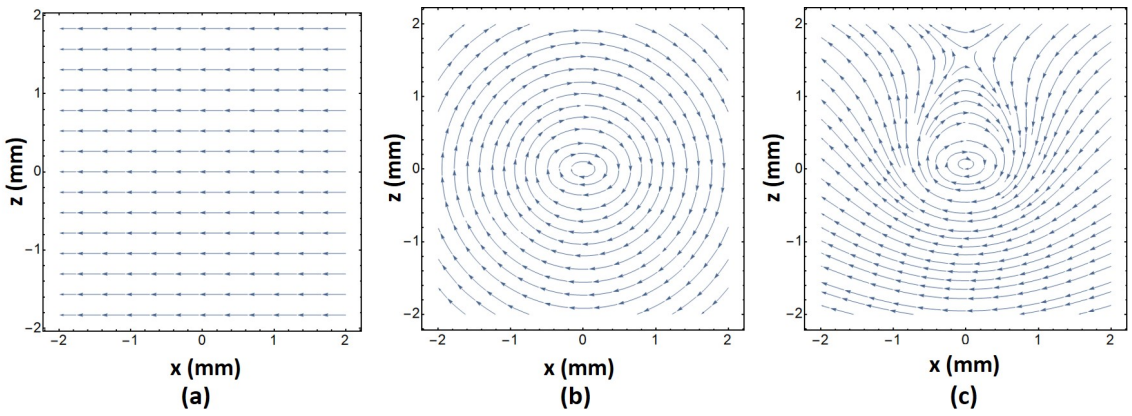

Figure 2.1: Field-line plots from a uniform bias field (a), radial field from a straight wire (b) and the combined field (c).

In our experimental setup, the atom chip is designed with planar rectangular cross-section U-shaped and Z-shaped wires with thickness $t = 0.127\,\text{mm}$ and width $w = 1\,\text{mm}$. By passing current through the wires and adding a uniform bias field B_x,

different trapping potentials are created. For the U-shaped wire, the bias field and the middle section $L = 5\,\text{mm}$ of the U-wire creates a two-dimensional quadrupole field while the two magnetic fields created by the two opposite currents running in the end segments in the x-direction are cancelled out at the trap centre $y = 0$. This configuration produces a three-dimensional quadrupole trap [42, 70] with a zero field minimum at position $(x_0, 0, z_0)$. This configuration can be employed to create a magneto-optical trap close to the reflecting surface of the atom chip without the use of external coils; this is known as a Compressed Mirror MOT (CMOT) [71, 72].

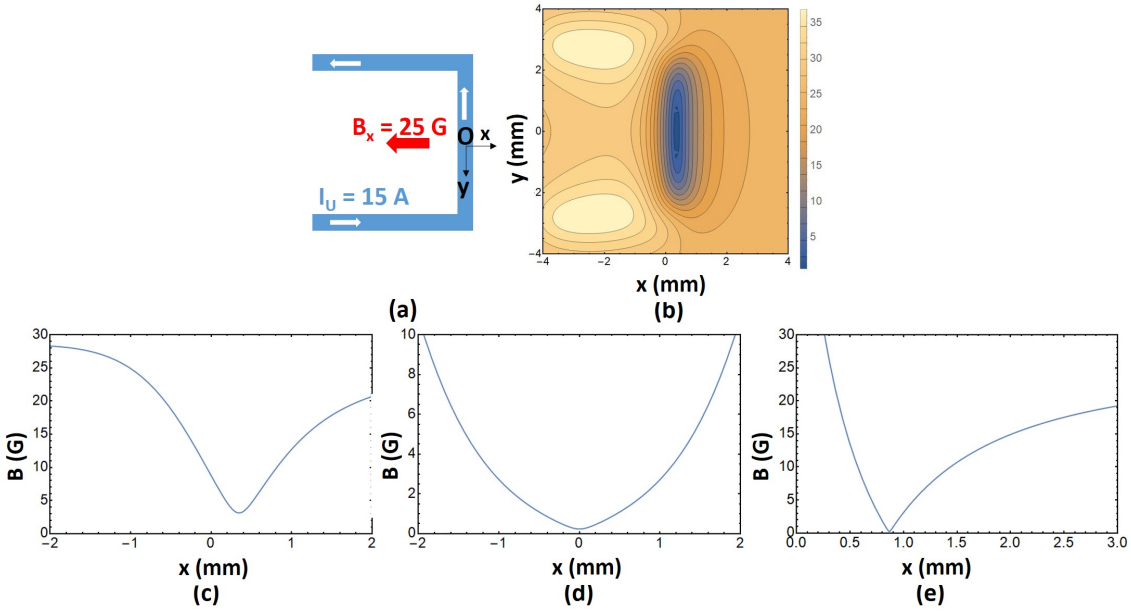

Figure 2.2: (a) U-wire trap with wire length $L = 5\,\text{mm}$, (b) calculated contour plot of the U-wire magnetic field and (c)(d)(e) calculated magnetic field cross-sections of the U-wire trap for $I_U = 15\,\text{A}$, $B_x = 25\,\text{G}$ and wire thickness $t = 0.127\,\text{mm}$.

A trapping field with a zero field minimum cannot be used for stable trapping due to Majorana spin-flip losses. A Ioffe-Pritchard type trap with a non-zero minimum field can be created by utilizing the Z-shaped wire on the atom chip. In the Z-wire, since the currents in the two end-segments are in the same direction, a non-zero field minimum is created. The field strength at the minimum can be controlled by the strength of a uniform bias field B_y along the middle section of the wire. Contour plots of the simulated trapping fields for U-wire and Z-wire traps calculated with

the help of the Radia coding package from the European Synchrotron Radiation Facility [73] are shown in the Figure 2.2 and 2.3 .

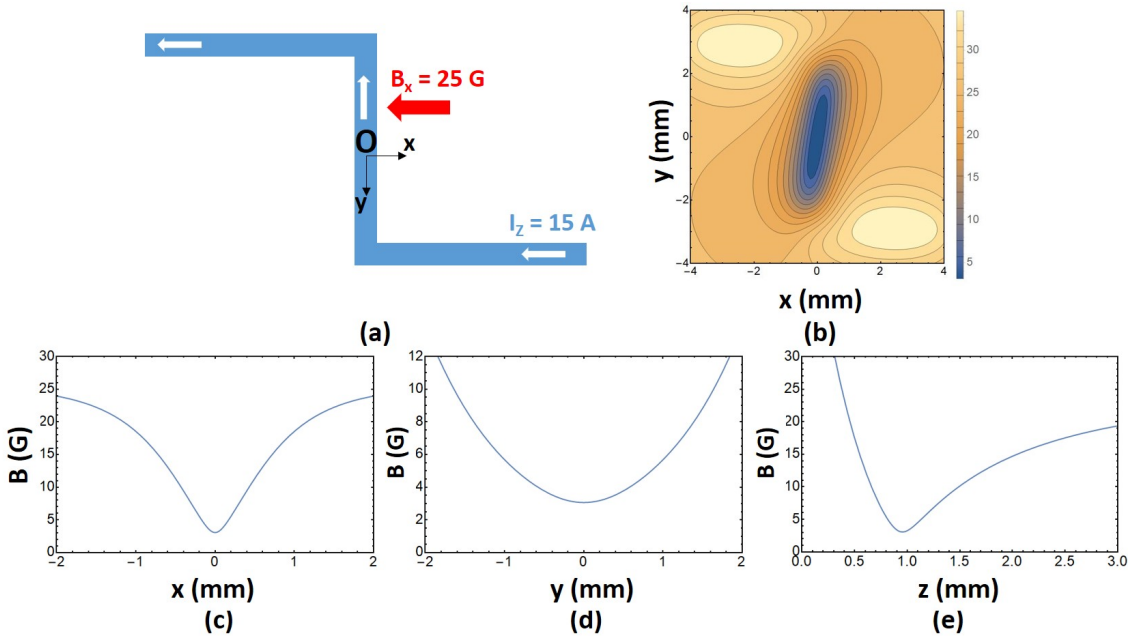

Figure 2.3: (a) Z-wire trap with wire length $L = 5\,\text{mm}$, (b) contour plot of the Z-wire magnetic field and (c)(d)(e) magnetic field cross-sections of a Z-wire trap for $I_Z = 15\,\text{A}$, $B_x = 25\,\text{G}$, $B_y = 0$ and wire thickness $t = 0.127\,\text{mm}$.

2.3 Theory of Bose-Einstein condensation

Bose-Einstein condensation (BEC) is defined as a state of a trapped bosonic gas in which a macroscopic occupation of the lowest quantum state occurs when the gas is cooled below a critical temperature close to absolute zero. In a BEC system, the bosonic atoms become indistinguishable as their inter-particle spacing becomes comparable with their matter wavelength. Atoms in a BEC system are described by Bose-Einstein statistics rather than Maxwell-Boltzmann statistics and are characterized by a sharp peak in the density distribution.

Consider N atoms trapped in a harmonic potential $U(x, y, z)$ given by:

$$U(x, y, z) = \frac{m}{2}(\omega_x^2 x^2 + \omega_y^2 y^2 + \omega_z^2 z^2), \tag{2.9}$$

where ω_x, ω_y and ω_z are the trapping frequencies in the x, y and z-directions. Neglecting atom-atom interactions, the many-body Hamiltonian can be rewritten as a sum of single-particle Hamiltonians with eigenvalues:

$$E_{n_x,n_y,n_z} = \left(n_x + \frac{1}{2}\right)\hbar\omega_x + \left(n_y + \frac{1}{2}\right)\hbar\omega_y + \left(n_z + \frac{1}{2}\right)\hbar\omega_z, \tag{2.10}$$

where n_x, n_y and n_z are positive integers.

In the grand-canonical ensemble the total number of particles at temperature T is given by [74]:

$$N = \sum_{n_x,n_y,n_z} \left[\exp\left[\beta(E_{n_x,n_y,n_z} - \mu)\right] - 1\right]^{-1}, \tag{2.11}$$

where $\beta = \dfrac{1}{k_B T}$ and μ is the chemical potential, and the total energy of the system is:

$$E = \sum_{n_x,n_y,n_z} \left[E_{n_x,n_y,n_z} \exp\left[\beta(E_{n_x,n_y,n_z} - \mu)\right] - 1\right]^{-1}. \tag{2.12}$$

In the thermodynamic limit $N \longrightarrow \infty$, as the level spacing becomes smaller and the chemical potential is equal to the energy of the lowest state $\mu = \dfrac{\hbar}{2}(\omega_x + \omega_y + \omega_z)$, the semi-classical expression for the number of atoms in excited states can be rewritten as:

$$N - N_0 = \int_0^\infty \frac{dn_x dn_y dn_z}{\exp[\beta\hbar(\omega_x n_x + \omega_y n_y + \omega_z n_z)] - 1} = \zeta(3)\left(\frac{k_B T}{\hbar\overline{\omega}}\right)^3, \tag{2.13}$$

where N_0 is the number of atoms in the ground state and $\zeta(n)$ is the Riemann zeta function, $\zeta(3) = 1.202$.

As $N_0 \longrightarrow 0$, the critical temperature of a BEC is given by:

$$T_c = \frac{\hbar\overline{\omega}}{k_B}\left(\frac{N}{\zeta(3)}\right)^{1/3}, \tag{2.14}$$

and the condensation fraction can be calculated as:

$$\frac{N_0}{N} = 1 - \left(\frac{T}{T_c^0}\right)^3. \tag{2.15}$$

In order to reach BEC, it is required that the phase space density (PSD) $\Phi = n\lambda_{dB}^3 \geq 1$, where $\lambda_{dB} = h/\sqrt{2\pi M k_B T}$ is the thermal de-Broglie wavelength of the atom cloud at temperature T and n is the atom density. The PSD is dependent on the characteristics of the trapping potential, e.g., $\Phi = \zeta(3) = 1.202$ for a 3D harmonic trap while $\Phi = \zeta(3/2) = 2.612$ for a 3D uniform (box) trap.

For a dilute bosonic gas system at low temperature, in the mean-field approach, the time-dependent Gross-Pitaevskii (GP) equation is employed to describe the system, which has the form of a nonlinear Schrodinger equation [63]:

$$i\hbar\frac{\partial}{\partial t}\psi(r,t) = \left(-\frac{\hbar^2}{2M}\nabla^2 + V(r) + g|\psi(r,t)|^2\right)\psi(r,t), \tag{2.16}$$

where $V(r)$ is the external confining potential, $g|\psi(r,t)|^2$ is the interaction potential due to the mean-field produced by the other particles in the condensate, $g = \frac{4\pi\hbar^2 a_s}{M}$ is the mean field coupling constant with the s-wave scattering length a_s . The GP equation is valid if the number of atoms in the condensate $N_c \gg 1$ and $a_s \ll d_a$, the average distance between atoms.

Substituting $\psi(r,t) = \psi(r)e^{-i\mu t/\hbar}$, the GP equation becomes:

$$\left(\frac{-\hbar^2}{2M}\nabla^2 + V(r) + g|\psi(r)|^2\right)\psi(r) = \mu\psi(r), \tag{2.17}$$

where $\psi(r)$ is the ground-state wavefunction of the condensate.

In the case where atom interactions are ignored, the scattering length $a_s = 0$ and the condensate takes a Gaussian shape. In the case where atom interactions are repulsive, the scattering length $a_s > 0$, and the kinetic energy term $-\frac{\hbar^2}{2M}\nabla^2\psi$ is neglected, the GP equation Eq.(2.17) becomes:

$$\left(V(r) + g|\psi(r)|^2\right)\psi(r) = \mu\psi(r). \tag{2.18}$$

This Thomas-Fermi approximation is valid for $Na_s/a_{ho} \gg 1$, where $a_{ho} = (\frac{\hbar}{m\omega})^{1/2}$ is the harmonic oscillator length. The trivial solution of the GP equation can be expressed as [75]:

$$\rho(r) = |\psi(r)|^2 = \frac{M}{4\pi\hbar^2 a_s}[\mu - V(r)]. \tag{2.19}$$

Solving the normalization condition $\int \rho dr = N$, the chemical potential is derived as [76]:

$$\mu = \frac{\hbar\overline{\omega}}{2}\left(\frac{15Na_s}{a_{ho}}\right)^{2/5}. \tag{2.20}$$

The density of the condensate vanishes when $\mu \geq V(r)$. For the region $\mu < V(r)$ the atom density is given by:

$$n(r)_{TF} = \psi^2(r) = \frac{\mu - V(r)}{g}. \tag{2.21}$$

For a harmonic trapping potential, the condensate takes a Thomas-Fermi inverted parabola shape with an ellipsoidal boundary for which the radius R_i is given by:

$$\mu = \frac{1}{2}M\omega_i^2 R_i^2. \tag{2.22}$$

In the case where the atom interactions are attractive, $a_s < 0$, the condensate is considered to be stable if $E_{int} < E_{kin}$, where E_{int} is the mean field interaction energy and E_{kin} is the kinetic energy. The kinetic energy acts as the main factor to prevent a "bosenova" collapse of a bosonic gas system with attractive interactions.

2.4 Atom-surface interactions

In our experiments, atoms are trapped in magnetic lattice microtraps at distances down to $\sim$ 90 nm from the chip surface at room temperature. The mean energy of a trapped atom is approximately $\sim$9 orders smaller than the mean thermal energy of the chip surface [77]. At such small distances, atoms can experience surface interaction mechanisms which can affect the behaviour of the trapped atoms. It is important to investigate the interactions systematically to see how close to a surface the trapped atoms can approach before being affected by the surface and lost. This information would also be useful for atom chip applications that require full coherent control of the trapped atoms close to the chip surface. The atom-surface interactions have been studied in detail both theoretically and experimentally in [78–82].

2.4.1 Interaction mechanisms

When trapped close to a surface, a neutral atom can interact with the surface via two fundamental coupling mechanisms, which are the interaction with the thermal and quantum-mechanical fluctuations of the electromagnetic field. The characteristics of the interactions are strongly dependent on the distance d and the nature of the surface (Figure 2.4).

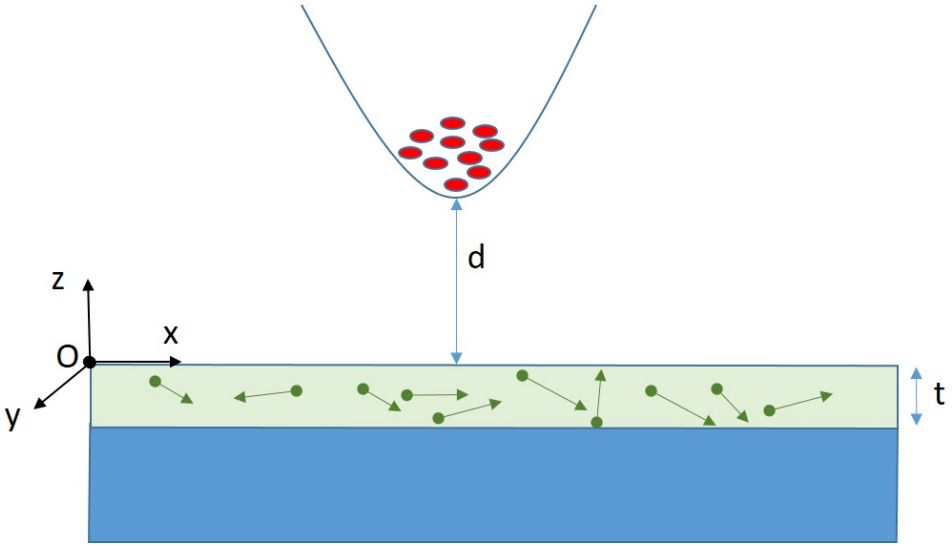

Figure 2.4: Schematic of a trapped atom cloud close to a conducting surface. Red dots represent the trapped atoms. Green circles with arrows represent thermal agitation electrons with random movements. t is the thickness of the conducting layer. Figure adapted from [77].

The interaction of the magnetic moment μ of a trapped atom with a fluctuating magnetic field can lead to spin flips, decoherence and heating of the atoms. The spin-flip results from coupling between the magnetic field components *perpendicular* to μ which drives the decoherence and loss due to transitions to untrappable states of the atoms. The coupling between the magnetic field components *parallel* to μ can lead to spin dephasing with a dephasing rate comparable to the spin-flip rate for most states. Heating and motional decoherence of atoms in the trap can occur due to the perturbation of the thermal magnetic near-field on the atom's centre of mass motion. In the surface near-field where the trap and spin-flip frequencies are < 10 GHz, the

thermal fluctuations dominate while the quantum fluctuations are negligible. This effect is negligible for dielectric surfaces. To reduce the thermal magnetic field noise, it is better to reduce the thickness and size of the conductors rather than to cool the surface as the spectral density of the magnetic field fluctuations increases as the surface temperature T decreases. Another way is to replace the conducting surface with a high resistance alloy or a superconducting material [83, 84].

Fluctuating electric fields can lead to a modification of the trapping potential through the interaction with atomic electric dipoles at optical frequencies. At these frequencies, quantum fluctuations are dominant while thermal fluctuations are negligible. In this case, the trapped atoms feel an attractive surface potential which can lead to a reduction in the trap depth of the trapping potential and hence atom losses through evaporation. This effect occurs in both conductors and dielectrics.

2.4.2 Casimir-Polder and van der Waals interactions

In the vicinity of a surface, the electric dipole of an atom in the ground state interacts with the fluctuating electromagnetic field from the surface which induces an attractive potential. As the trapped atom approaches the surface, it experiences several interaction regimes with different dominant interacting mechanisms (Figure 2.5). At large distances $z \gg \lambda_T = \hbar c/k_B T$ (the thermal photon wavelength), thermal fluctuations are dominant and the potential scales as $-T/z^3$ at thermal equilibrium. In this Lifshitz or thermal regime, quantum fluctuations are negligible. Approaching closer to the surface where $\lambda_T \gg z \gg \lambda_{opt}/2\pi$ the atom enters the Casimir-Polder regime. In this regime, quantum fluctuations are dominant while thermal fluctuations are negligible. This potential scales as $-1/z^4$. In the next regime $\lambda_{opt}/2\pi \gg z \gg a_0$ (where a_0 is the Bohr radius), the van der Waals-London regime, the potential scales as $-1/z^3$. For the final regime where $z \sim a_0$, chemical physics mechanisms which control surface field phenomena such as surface adsorption are dominant.

In our experiment setup, thermal fluctuations are negligible and ^{87}Rb atoms are trapped in the Casimir-Polder and van der Waals-London regimes. The trapping

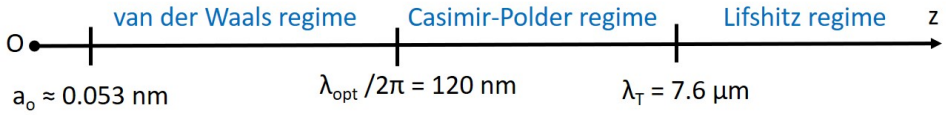

Figure 2.5: Interaction regimes for a ^{87}Rb atom trapped close to a surface. Adapted from [77].

potential can be distorted due to the attractive potential arising from the interaction of the atomic electric dipoles with the fluctuating electromagnetic field. From an atomic physics perspective, the Casimir-Polder potential originates from a change in the AC Stark effect due to the change in boundary conditions in the presence of a surface, which is treated as a macroscopic object, and thus a change in the mode spectrum of the electromagnetic field [85]. The dependence of the Casimir-Polder potential on the distance to the surface can be explained by the fact that the mode function is only affected when the condition $\lambda > z$ is satisfied, where λ is the mode wavelength. On the other hand, the van der Waals effect is considered to result from the interaction between an atomic dipole and its field which is reflected from the surface.

In the Casimir-Polder and van der Waals-London regimes, the attractive potential can be expressed as [86]:

$$V_{CP}(d) = -\frac{C_4}{d^3(d + 3\lambda_{opt}/2\pi^2)}, \tag{2.23}$$

where d is the trapping position and C_4 is the Casimir-Polder coefficient given by [87]:

$$C_4 = \frac{1}{4\pi\epsilon_0}\frac{3\hbar c\alpha_0}{8\pi}\frac{\epsilon_r - 1}{\epsilon_r + 1}\phi(\epsilon_r), \tag{2.24}$$

where ϵ_0 is the vacuum permittivity, c is the light velocity, α_0 is the static atomic polarizability which for ^{87}Rb atoms is $\alpha_0 = 5.25 \times 10^{-39}$ Fm^2 and $\phi(\epsilon_r)$ is a numerical factor which is dependent on the relative permittivity ϵ_r of the top surface layer [88].

In the presence of atom-surface interactions, a harmonically trapped atom close to the chip surface feels a combined potential given by:

$$V(z, d) = V_t(z) + V_{CP}(d), \tag{2.25}$$

where $V_t(z) = \frac{1}{2}m\omega_t^2(z-d)^2$ is the harmonic trapping potential when the atom-surface interactions are neglected. The attractive Casimir-Polder potential reduces the trap depth as the atoms get closer to the surface. At a finite distance $d > 0$, the attractive Casimir-Polder potential cancels the harmonic trapping potential making the combined trap depth zero. This is different from the case where there is no Casimir-Polder interaction, and the trap depth reaches zero at $d = 0$.

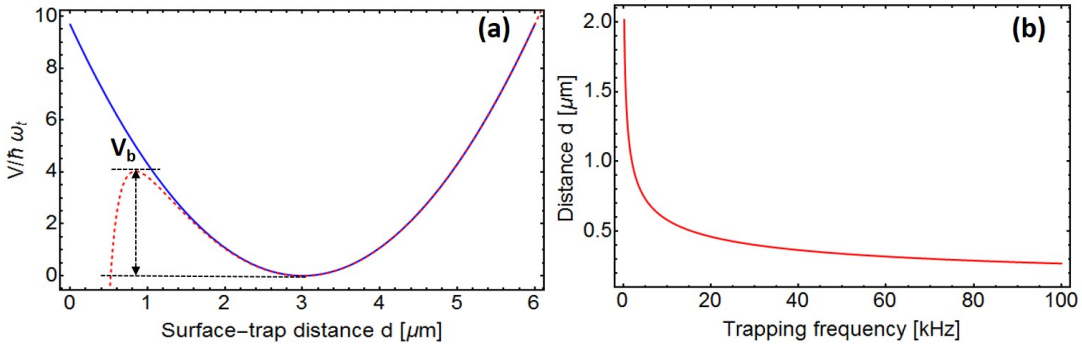

Figure 2.6: (a) Trapping potential with Casimir-Polder interaction close to a silica surface. The blue curve shows the harmonic trapping potential without the Casimir-Polder interaction. The red curve shows the effective trapping potential with the Casimir-Polder interaction. The trap position is located at $d = 3\,\mu$m from the surface for a trapping frequency $\omega_t/2\pi = 250$ Hz. (b) Calculated trap-surface distance d versus trap frequency $\omega_t/2\pi$.

Figure 2.6 (a) shows an example of the total trapping potential experienced by an atom in the presence of a silica surface where the trap depth decreases due to the attractive surface potential. In order to trap atoms with energy $E = \zeta\hbar\omega_t$, where $\zeta = 1/2$ for the lowest bound state of a harmonic trap, the condition $V_b(d_{min}, \omega_t) = \zeta\hbar\omega_t$ must be satisfied. Our calculation of d_{min} versus trapping frequency ω_t (Figure 2.6 (b)) shows that it is possible to trap atoms at a distance $d < 0.5\,\mu$m by providing a trapping frequency $\omega_t/2\pi > 20$ kHz.

2.4.3 Johnson magnetic noise

In an atom chip experiment, Johnson noise results from thermal agitation of the electrons in both the reflecting metallic surface and the current-carrying wires of the atom chip. This thermal agitation of the electrons induces current noise which consequently generates a fluctuating magnetic field and can induce spin-flip losses of atoms in the trap. This thermal magnetic noise is dominant within the near-field regime of the conductor where the magnitude is much larger than the black body radiation. This effect is considered to be the main limitation to the trap performance close to conductors [87, 89–92].

The spectral density of the magnetic field fluctuations is given by [90, 93]:

$$S_{B\alpha\beta}(\omega) = \frac{\mu_0^2 \sigma k_B T \cdot s_{\alpha\beta} \cdot g(d,t,\delta)}{16\pi d}, \qquad (\alpha,\beta = x,y,z) \tag{2.26}$$

where $s_{\alpha\beta} = diag\left(\frac{1}{2}, 1, \frac{1}{2}\right)$ is a tensor which is diagonal in the coordinate system of Figure 2.4, $g(d,t,\delta)$ is a dimensionless function of the distance d from the conducting surface, t is the thickness of the conducting film, $\delta = \sqrt{2/(\sigma\mu_0\omega)}$ is the skin depth and σ is the electrical conductivity of the conducting film.

The function g is dependent on the geometry and the frequency ω and has the expressions [87, 94]:

$$g = \begin{cases} 1, & \text{for d}\ll \delta \ll t, \\ 3\delta^3/2d^3, & \text{for } \delta \ll min(\delta,t), \\ \frac{t/d}{1+[4dt/(\pi^2\delta^2)]^2}, & \text{for } t \ll min(\delta,d), \\ \frac{t}{t+d}, & \text{for } \delta \gg max(\delta,d), \\ \frac{tw}{(t+d)(w+2d}, & \text{for } \delta \gg max(\delta,d)\ and\ finite\ w, \end{cases} \tag{2.27}$$

where w and t are the width and thickness of the conducting film, respectively.

The mean square fluctuation of the magnetic field components is given by:

$$\langle B_\alpha^2(d)\rangle = \frac{1}{\pi}\int_0^\infty S_{B\alpha\alpha}(\omega)d\omega. \tag{2.28}$$

For a transition between adjacent magnetic sublevels $|F=1, m_F=-1\rangle$ and $|F=1, m_F=0\rangle$ at the Larmor frequency, the transition rate γ_s is given by [77]:

$$\gamma_s = g(d,t,\delta)\cdot\frac{3\mu_0^2\mu_B^2\sigma k_B T}{256\hbar^2\pi d}. \tag{2.29}$$

For $\delta \gg \max\{d,t\}$, the dimensionless function g can be approximated by $g(d,t,\delta) \simeq t/(t+d)$ which gives the Johnson noise spin flip lifetime:

$$\tau_s = \gamma_s^{-1} = \frac{d(t+d)}{t}\cdot\frac{256\pi\hbar^2}{3\mu_0^2\mu_B^2\sigma k_B T}. \tag{2.30}$$

For example, for a gold reflecting film with $t = 0.05$ μm, $d = 0.28$ μm, $T = 300$ K, we obtain a thermal spin-flip lifetime $\tau_{Au} \approx 180$ ms. The spin-flip lifetime could be increased if required by using a reflecting film with higher resistivity, such as palladium ($\rho_{Pd} = 1.05 \times 10^{-7}$ Ωm), for which the spin-flip lifetime becomes $\tau_{Pd} \approx$ 870 ms [17].

2.4.4 Atom-adsorbate effect

For atom trapping experiments using atom chips, it is normal that atoms are adsorbed on the chip surface. The adsorbed atoms generate a small electric dipole moment μ_e perpendicular to the chip surface through their electron redistribution. The quadratic Stark effect, which results from the interaction between the trapped atoms and the combined electric fields from the adsorbed atoms, creates an attractive potential [95]:

$$V_a(r) = -\frac{\alpha_0|E_0(r)|^2}{2}, \tag{2.31}$$

where $E_0(r)$ is the combined electric fields from the adsorbed atoms and α_0 is the atomic polarizability. The magnitude of $V_a(r)$ depends on the surface material and the spatial distribution of the adsorbed atoms. The adsorbed atoms, if distributed inhomogeneously, can lead to a corrugated trapping potential produced by the current-carrying wire or magnetic lattice structures on the chip. To reduce the negative effect of atom adsorbates, coating the chip surface with a thin layer of SiO_2 to reduce μ_e, is sometimes used [96].

2.4.5 Hitting effect

When trapped very close to the surface, atoms can be lost by hitting the hot surface of the atom chip. This effect results from the fact that atoms with energies comparable to the barrier height can tunnel through the barrier of the traps. For atoms with low energies, this effect is negligible. In our experiments, the Z-wire trap is designed so that the trap depth is at least 10 times larger than the average temperature of the trapped atoms in order to limit hitting losses. However, when atoms are trapped in magnetic lattice traps with small barrier heights, some fraction of the trapped atoms can be lost due to hitting losses.

2.4.6 Stray light effect

When trapped close to the gold reflecting surface of the atom chip, atoms in a magnetic trap are prone to stray resonant light which can induce spin-flip losses through optical pumping. The loss rate γ_{sl} can be expressed as:

$$\gamma_{sl} = \Gamma \frac{I_{bg}}{I_s}, \tag{2.32}$$

where Γ is the linewidth of the strong dipole transition, I_s is the saturation intensity and I_{bg} is the intensity of the stray light.

2.5 Collisional trap loss

In our atom chip experiments, atoms are trapped with large trapping frequencies, from several hundred Hz (in the Z-wire magnetic trap) up to a few hundred kHz (in the magnetic lattice traps). Therefore, even for a small total atom number N, the atoms can be confined at a very high density n. At this high density, inelastic collisions can occur and cause trap losses. The collisional trap loss rate is given by [63]:

$$\frac{1}{N}\frac{dN}{dt} = -\gamma_{bg} - K\langle n\rangle - L\langle n^2\rangle, \tag{2.33}$$

where γ_{bg} is the background collision loss rate, $K\langle n\rangle$ describes inelastic two-body collisions while $L\langle n^2\rangle$ represents three-body recombination.

The background collision loss occurs due to collisions of the trapped atoms with the residual gas inside the ultra high vacuum chamber. The background loss rate is independent of the atom density n but proportional to the residual gas density.

Three-body recombination loss is defined as an inelastic collision where three trapped atoms are involved. At first, two trapped atoms combine to form a molecule. The kinetic energy of this molecule, gained from the conversion of excess binding energy, is shared by a third atom through conservation of energy and momentum. Normally, this kinetic energy is larger than the barrier height of the trapping potential and all three atoms are lost by escaping out of the trap. The three-body recombination loss rate γ_{3b} is given by [63]:

$$\gamma_{3b} = L\langle n^2\rangle \propto \omega_{ho}^{12/5} N^{4/5}, \tag{2.34}$$

where ω_{ho} is the harmonic oscillator trapping frequency and N is the total number of atoms in the trap for a BEC with a Thomas-Fermi distribution. At high density, the three-body recombination loss rate for ^{87}Rb atoms in the $|F=1, m_F=-1\rangle$ and $|F=2, m_F=2\rangle$ states is dominant with the BEC rate constants $L_{|F=1,m_F=-1\rangle} = 5.8(1.9)\times 10^{-30}$ and $L_{|F=2,m_F=2\rangle} = 1.8(0.5)\times 10^{-29}$ [56, 57].

For ^{87}Rb atoms in the $|F=1, m_F=-1\rangle$ and $|F=2, m_F=2\rangle$ states, inelastic two-body collisions, which occur by weak spin-dipole interaction due to spin exchange collisions, are forbidden due to conservation of energy and angular momentum rules [63, 97, 98]. The two-body loss rate γ_{2b} is given by:

$$\gamma_{2b} = K\langle n\rangle \propto \omega_{ho}^{6/5} N^{2/5}. \tag{2.35}$$

Normally, for these states $\gamma_{3b} + \gamma_{bg} \gg \gamma_{2b}$, and so the two-body loss rate is neglected in our experiments.

2.6 Theoretical framework of the design of the sub-micron 2D magnetic lattice

2.6.1 Optimization algorithm

The concept of a 1D magnetic lattice is based on the early work of our group on magnetic mirrors. By applying a bias field B_y perpendicular to the magnets, a magnetic mirror with flat equipotentials can be converted into a corrugated structure comprising a 1D array of magnetic traps. Such a 1D magnetic lattice may be extended to 2D by various methods described in [24, 25, 28, 31]. However, these methods are complicated and limited to certain trapping geometry and lattice periods. Therefore, for our lattice structures, a programming algorithm developed by Schmied et al. [28] for designing almost arbitrary configurations of magnetic traps based on patterned magnetic films is employed. The advantage of this method is it gives much more freedom for the design of complex patterns such as triangular, honeycomb, etc. which is limited in other methods.

This algorithm can produce finite or infinite single-layer magnetization patterns with perpendicular magnetization that can satisfy desired lattice symmetries, geometry, period and surface-trap distance and especially Ioffe-Pritchard traps to avoid Majorana spin-flip losses. Basically, the algorithm generates a binary image which encodes the magnetic versus non-magnetic regions within one unit cell, so that the generated pattern has pixels with either zero or maximal magnetization. This image is then exported to a format suitable for the lithographic patterning software. Thanks to the binary nature of the pattern, the lithography procedure is rather straightforward by etching away the pixels with zero magnetization.

To obtain an optimized magnetic lattice for a magnetic film with thickness t and magnetization M_z, at first a scalar magnetic potential generated in the xy plane is defined as:

$$\Phi(x,y,z) = \frac{\mu_0 t M_z}{2}\int_P m(x',y')G(x-x',y-y',z)dx'dy', \tag{2.36}$$

where μ_0 is the free space permeability, $G(x,y,z) = \frac{z}{2\pi(x^2+y^2+z^2)^{3/2}}$ is the Green's function and $m(x,y)$ is a dimensionless function describing the spatial dependence of the magnetization current which varies from 0 to 1.

We assume that $\vec{r}^{(l)}$ is the desired trapping positions; $\vec{u}^{(l)} = -\vec{\mathbf{B}}(\vec{r}^{(l)})$ is the local magnetic field vector at the trap positions with components u_i^l; $\vec{v}^{(l)}$ are the local magnetic field tensors with components $v_{i,j}^{(l)}$ such that $v_{1,1}^{(l)} + v_{2,2}^{(l)} + v_{3,3}^{(l)} = 0$; and the $\vec{w}^{(l)}$ are the local magnetic field curvature tensors with components $w_{i,j,k}^{(l)}$ such that $w_{i,1,1}^{(l)} + w_{i,2,2}^{(l)} + w_{i,3,3}^{(l)} = 0$ for all i integers varying from 1 to 3.

Then the scalar magnetic potential around the trap points can be expressed as:

$$\begin{aligned}\Phi(\vec{r}) = \Phi_0^l + \sum_{i=1}^{3} u_i^l(r_i - r_i^l) + \frac{1}{2}\sum_{i,j=1}^{3} v_{i,j}^{(l)}(r_i - r_i^l)(r_j - r_j^l) \\ + \frac{1}{6}\sum_{i,j,k=1}^{3} w_{i,j,k}^{(l)}(r_i - r_i^l)(r_j - r_j^l)(r_k - r_k^l) + ...,\end{aligned} \tag{2.37}$$

where $(r_1, r_2, r_3) = (x, y, z)$ are the Cartesian coordinates.

In order to obtain Ioffe-Pritchard traps, it is required that the eigenvalues of the gradient tensors associated with the traps v^l are zero and $v^l.\vec{B}_I = 0$, where $\vec{B}_I$ is the Ioffe field. For equal trap depths of all trapping potentials, it is required that v^l is well aligned with the Ioffe axes for all $\vec{r}^l$. For desired trapping potential shapes, orientations and aspect ratios, further constraints on the eigenvalues of v^l, $\vec{u}^{(l)}$ and $\vec{w^{(l)}}$ are required.

For optimizing the magnetization pattern, the atom chip surface is first subdivided into N small domains, where the number of domains N determines the resolution of the magnetization pattern. The total scalar magnetic potential and its derivatives are then expressed as:

$$\begin{aligned}\Phi(\vec{r}) &= \frac{1}{2}\mu_0\delta M_z \sum_\alpha m_\alpha \phi_\alpha(\vec{r})\frac{\partial\Phi(\vec{r})}{\partial r_i} \\ &= \frac{1}{2}\mu_0\delta M_z \sum_\alpha m_\alpha \frac{\partial\phi_\alpha(\vec{r})}{\partial r_i},\end{aligned} \tag{2.38}$$

where $\phi_\alpha(x,y,z) = \int_{A_\alpha} G(x-x', y-y', z)dx'dy'$ are the scalar magnetic potentials induced by the domains α covering an area A_α, and the components m_α of vector $\vec{m}$ are equal to 1 for fully magnetic domains or 0 for non-magnetic domains. A matrix equation which takes into account all constraints is defined as:

$$\mathbf{A}.\vec{m} = C\vec{b}, \tag{2.39}$$

where the prefactor C is maximized to gain the highest Zeeman pseudopotential possible.

The main limitation of this algorithm is that it does not consider the shape of the Zeeman pseudopotentials between the Ioffe-Pritchard traps. This is negligible for ion trapping experiments while for neutral atom trapping experiments, points with zero magnetic fields can lead to trap losses due to tunnelling between Ioffe-Pritchard traps and Majorana spin-flip losses [21].

2.6.2 Optimized square and triangular magnetization pattern

Our 2D square and triangular magnetic lattice structures are designed with one Ioffe-Pritchard trap per unit cell at $\{0, 0, h\}$ with a Ioffe axis { sinϕ, cosϕ, 0}. Our nominal lattice trapping height is chosen to be $a/2$, which is one half of the inter-trap distance. For this design, the second derivative of the scalar magnetic potential is constrained as

$$\Phi_{\zeta,\phi(\vec{r})} = \Phi\left[\alpha \sin\left(\frac{2\pi x}{a} - \frac{2\pi y}{a\tan\zeta}\right) + \sin\alpha \sin\left(\frac{2\pi y}{a\sin\zeta}\right)\right], \tag{2.40}$$

where a is the lattice period.

The magnetization pattern for a *square* lattice of Ioffe-Pritchard traps at a trapping height $h = a/2$ is produced with $\zeta = \pi/2$, where the barrier heights in the x and y-directions are equal. Due to the higher-order Fourier modes, the square magnetization pattern and the Ioffe direction do not conform to exact *cmm* symmetry [28], which consequently creates an imperfect *cmm* symmetric Zeeman pseudo-potential . However, this limitation can be overcome by slightly tuning the Ioffe field strength.

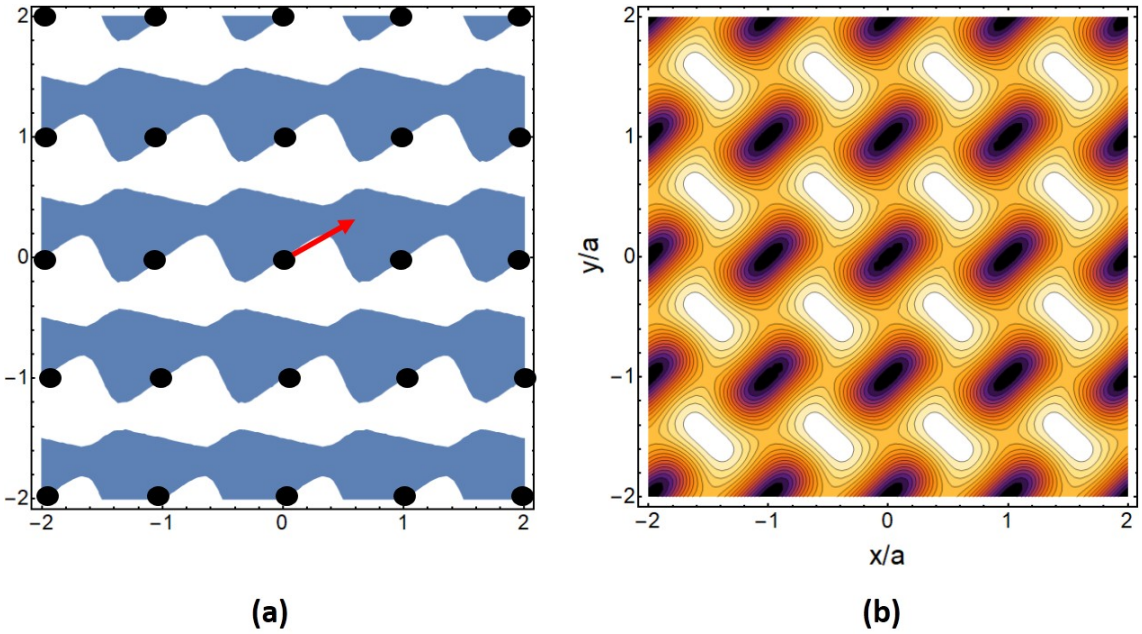

Figure 2.7: Optimized square magnetic lattice structure (a) and simulated Zeeman pseudo-potentials at the trapping plane $h = a/2$. Input parameters: $4\pi M_z = 5.9\,\mathrm{kG}$, $t_m = 10.34\,\mathrm{nm}$. Black points in (a) indicate the positions of the trap centres and the red arrow indicates the direction of the Ioffe-Pritchard field. Dark regions in (b) indicate trap minima.

The magnetization pattern for a *triangular* lattice of Ioffe-Pritchard traps at trapping height $h = a/2$ is produced with $\zeta = \pi/3$, where the barrier heights in all three lattice directions are equal. For triangular lattices, in order to obtain equivalent tunnelling in all three directions and anisotropic lattice, the Zeeman pseudo potential should be fully $p6m$ symmetric. This can cause a problem since the symmetry requires nonlinear constraint beyond the linear programming method. By providing additional linear constraints, it is possible to overcome this problem by applying additional linear constraints at the trap barrier positions [28].

By manipulating the bias magnetic fields in the parallel and perpendicular directions, one can change characteristics of the trapping potential such as the distance of the trap minima to the surface, trapping frequencies, etc. These parameters play an important role in determining the behaviour of the trapped atoms in the magnetic

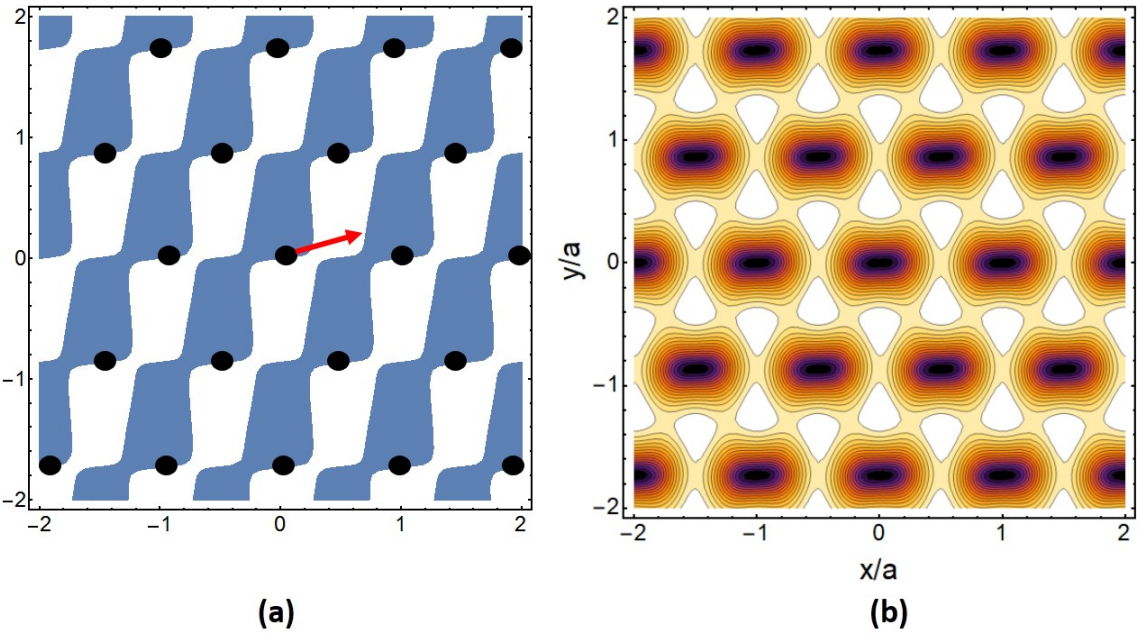

Figure 2.8: Optimized triangular magnetic lattice structure (a) and simulated Zeeman pseudo-potentials at the trapping plane $h = a/2$. Input parameters of the simulations: $4\pi M_z = 5.9\,\mathrm{kG}$, $t_m = 10.34\,\mathrm{nm}$. Black points in (a) indicate the positions of the trap centres and the red arrow indicates the direction of the Ioffe-Pritchard field. Dark regions in (b) indicate trap minima.

lattice. There are no analytic expressions for the lattice trapping magnetic fields as in the 1D case; so the numerical approach was utilized for the calculation of the trap minimum position as well as the Ioffe field trap bottom [28].

To create the optimized $0.7\,\mu$m-period square and triangular magnetic lattice traps at a trapping height $z_{min} = a/2 = 0.35\,\mu$m, it is required to provide the bias field configuration shown in Table 2.1. The resulting lattice traps have the desired 2D geometry traps with equal barrier heights in the lattice directions and non-zero trap bottoms. It is important to note that these bias field values are just for illustration since it is possible to create lattice traps with similar characteristics keeping the same ratio between the bias fields in the (x, y, z) directions. In our atom chip, the Co/Pd magnetic film stack is coated with a layer of 50 nm gold and a layer of 25 nm silica. Therefore, the optimized magnetic lattice traps are just 275 nm

Table 2.1: Calculated parameters for the optimized 0.7 μm-period square and triangular magnetic lattices at trapping height $z_{min} = 0.35\,\mu$m. Input parameters of the simulations: magnetization of the magnetic film $4\pi M_z = 5.9\,$kG, magnetic film thickness $t_m = 10.34\,$nm.

	Square Lattice	Triangular Lattice
Required bias field (B_x, B_y, B_z)	(7.86 G, −3.76 G, 0)	(0.50 G, 4.52 G, 0)
Barrier height in lattice directions	6.56 G (220 μK)	5.97 G (200 μK)
Trap depth δE_z	3.61 G (121 μK)	2.85 G (96 μK)
Trap bottom	5.11 G	1.69 G
Geometric mean trapping frequency	$\overline{\omega}/2\pi = 173\,$kHz	$\overline{\omega}/2\pi = 195\,$kHz

from the atom chip surface. At such a small distance, atoms in the lattice traps are in the region where the attractive Casimir-Polder potential effect is dominant.

2.7 Ultracold atoms in a periodic lattice

For a gas of interacting ultracold bosonic atoms confined by an external trapping potential, the many body Hamiltonian has the form [99]:

$$\begin{aligned}\hat{H} = &\int d\mathbf{r}\hat{\psi}^\dagger(\mathbf{r})\left(-\frac{\hbar}{2m}\nabla^2 + V_{ext}(\mathbf{r})\right)\hat{\psi}(\mathbf{r}) \\ &+ \frac{1}{2}\int d\mathbf{r}d\mathbf{r}'\hat{\psi}^\dagger(\mathbf{r})\hat{\psi}^\dagger(\mathbf{r}')V_{at}(\mathbf{r}-\mathbf{r}')\hat{\psi}(\mathbf{r}')\hat{\psi}(\mathbf{r}),\end{aligned} \tag{2.41}$$

where $\hat{\psi}(\mathbf{r})$ and $\hat{\psi}^\dagger(\mathbf{r}')$ are the bosonic annihilation and creation field operators, respectively and V_{at} is the interatomic scattering potential.

For a cold dilute gas, in which s-wave scattering is the main scattering process, the interatomic scattering potential $V_{at}(\mathbf{r})$ can be described as a contact interaction:

$$V_{at}(\mathbf{r}) = \frac{4\pi\hbar^2 a_s}{m}\delta(\mathbf{r}), \tag{2.42}$$

where m is the mass of the atoms and a_s is the s-wave scattering length.

In our experiments, the dynamics of bosonic atoms in a periodic lattice potential is described by a Bose-Hubbard model [99]. This simplest non trivial model is famous in solid state physics and used to describe many interesting effects such as the superfluid to a Mott insulator transition [5, 100]. The Hamiltonian for bosonic atoms in a trapping potential $V(x)$:

$$\begin{aligned}\hat{H} = &\int d^3x \hat{\psi}^\dagger(\mathbf{x}) \left(-\frac{\hbar}{2m}\nabla^2 + V(\mathbf{x})\right) \hat{\psi}(\mathbf{x}) \\ &+\frac{1}{2}\frac{4\pi\hbar^2 a_s}{m} \int d^3x \hat{\psi}^\dagger(\mathbf{x})\hat{\psi}^\dagger(\mathbf{x})\hat{\psi}(\mathbf{x})\hat{\psi}(\mathbf{x}),\end{aligned} \tag{2.43}$$

where $V(x)$ is the sum of the lattice potential $V_{lat}(x)$ and the external confinement $V_{ext}(x)$ and $\hat{\psi}(\mathbf{x})$ is a boson field operator.

The boson field operator $\hat{\psi}(\mathbf{x})$ can be expressed in the form of localized Wannier functions $w(\mathbf{x} - \mathbf{x}_i)$ of the ground state:

$$\hat{\psi}(\mathbf{x}) = \sum_i \hat{a}_i w(\mathbf{x} - \mathbf{x}_i), \tag{2.44}$$

where $\hat{a}_i$ is the annihilation operator of the lattice site i and $[\hat{a}_i, \hat{a}_j^\dagger] = \delta_{ij}$.

Equation (2.43) reduces to the Bose-Hubbard Hamiltonian [99]:

$$\hat{H} = -J \sum_{<i,j>} \hat{a}_j^\dagger \hat{a}_i + \sum_i (\epsilon_i - \mu)\hat{n}_i + \sum_i \frac{1}{2} U \hat{n}_i(\hat{n}_i - 1), \tag{2.45}$$

where $\hat{n}_i = \hat{a}_i^\dagger \hat{a}_i$ is the operator counting the atom number in lattice site i. The first term of the Bose-Hubbard Hamiltonian describes the tunnelling of atoms between lattice sites. The tunnelling strength of this term is characterized by the hopping matrix element J which is expressed as [5]:

$$J = -\int d^3x w(\mathbf{x} - \mathbf{x}_i)\left(\frac{-\hbar^2\Delta^2}{2m} + V_{lat}(x)\right) w(\mathbf{x} - \mathbf{x}_j). \tag{2.46}$$

The second term characterizes the external trapping potential which introduces an energy offset ϵ_i of the lattice site i and the chemical potential μ. The third term accounts for the repulsive interaction between two atoms in a single lattice site i and is characterized by the on-site interaction matrix element U:

$$U = \frac{4\pi\hbar^2 a_s}{m} \int |w(\mathbf{x})|^4 d^3x. \tag{2.47}$$

Depending on the ratio U/J, the Bose Hubbard Hamiltonian can have two different ground states. If $J \gg U$, the tunnelling term dominates and the atoms tend to spread out over the lattice. The system is in a superfluid state with long-range phase coherence over the lattice. In this case, the quantum fluctuation is neglected and all the atoms have the same identical Bloch states. The system is characterized by a macroscopic wave function with phase defined in each lattice site. The many-body ground state of the system is expressed as [5]:

$$|\Psi_{SF}\rangle_{U/J\approx 0} \propto \left(\sum_{i=1}^{M} \hat{a}_i^\dagger\right)^N |0\rangle, \tag{2.48}$$

where N is the total number of atoms. The variance of the Poissonian atom number distribution for a single lattice site is then expressed as:

$$Var(n_i) = \langle \hat{n^i} \rangle. \tag{2.49}$$

If $U \gg J$, the interaction term dominates and the atoms tend to localize in lattice sites. The system is characterized by localized atomic wave functions with a fixed number of atoms in each lattice site in order to minimize the interaction energy. The system is in the Mott insulator state and no longer exhibits phase coherence but exhibits strong correlations in the number of atoms in lattice sites. The many-body ground state is then expressed as a product of local Fock states in each lattice site [5]:

$$|\Psi_{MI}(n)\rangle_{J\approx 0} \propto \prod_{i=1}^{M} (\hat{a}_i^\dagger)^n |0\rangle, \tag{2.50}$$

where M is the number of lattice sites.

The ratio of U/J can be controlled by varying the lattice trap depth V_{lat}. As the ratio U/J reaches a quantum critical point, a quantum phase transition occurs in which the system changes from the superfluid state to the Mott insulator state and vice versa [5, 101]. The phase change features a change in the excitation spectrum

of the system; as the quantum critical point is crossed in the Mott insulator regime the excitation spectrum shows a gap whereas in the superfluid phase there is no gap in the excitation spectrum.

Table 2.2: Calculated tunnelling times for a 2D square lattice for different lattice periods a at the quantum critical point $(J/U)_c \approx 0.06$.

Period a	0.3 μm	0.7 μm	1 μm	3 μm	10 μm
E_r	306 nK	56 nK	28 nK	3.1 nK	275 pK
V_{lat}	2.8 mK	668 nK	362 nK	53 nK	6.3 nK
J	8.6 nK	820 pK	300 pK	14 pK	0.46 pK
U	143 nK	13.7 nK	5 nK	230 pK	7.7 pK
τ_{tunnel}	0.9 ms	9.3 ms	25 ms	0.55 s	17 s

In order to estimate the strength of the tunnelling term J and the on-site interaction term U, units of the recoil energy $E_r = \hbar^2 k^2/(2m)$ are introduced [102]. The expressions for J/E_r and U/E_r can be approximated as [102]:

$$J/E_r = \frac{4}{\sqrt{\pi}} \left(\frac{V_{lat}}{E_r}\right)^{3/4} \exp\left[(\frac{-2V_{lat}}{E_r})^{1/2}\right], \tag{2.51}$$

$$U/E_r = \frac{2\sqrt{2}ka_s}{\sqrt{\pi}} \left(\frac{V_{lat}}{E_r}\right)^{3/4}. \tag{2.52}$$

The case of the superfluid to Mott insulator transition in a magnetic lattice has been considered by Ghanbari *et. al* [41]. For a 2D square lattice with equal trap depths in all directions, which is similar to our magnetic lattice structures, the quantum critical point is expected to occur at $(J/U)_c \approx 0.06$ [103]. Table 2.2 presents calculated parameters for a 2D square lattice for different lattice periods a at the quantum critical point $(J/U)_c \approx 0.06$. As can be seen, in order to achieve reasonably short tunnelling times (*e.g.*, $< \sim$10 ms) lattices with submicron periods are required.

CHAPTER 3

The magnetic lattice atom chip

3.1 Introduction

In our Magnetic Lattice group in the Centre for Quantum and Optical Science at Swinburne, we had been using a one-dimensional 10 μm-period magnetic lattice structure mounted on a micromachined silver-foil atom chip, providing a platform to trap independent periodic arrays of ultracold atoms and Bose Einstein condensates [22, 32, 33]. A periodic microstructure consisting of one-thousand parallel grooves of 10 mm length and 10 μm spacing was etched in the centre of a silicon wafer. The grooved microstructure was coated with six layers of 160 nm-thick magneto-optical $Tb_6Gd_{10}Fe_{80}Co_4$ film, separated by 100 nm-thick non-magnetic chromium layers. A 150 nm-thick gold film (reflectivity $>$ 95 % at 780 nm) was deposited on the top for the mirror MOT and for reflective absorption imaging of the atom clouds. The TbGdFeCo microstructure was magnetized in a strong magnetic field leading to a remanent perpendicular magnetization $4\pi M_z = 3\ kG$ with a coercivity $H_c = 6\ kOe$ [22]. Trapping of ultracold ^{87}Rb $|F = 2, m_F = 2\rangle$ atoms in multiple lattice sites was demonstrated in the work of M. Singh et al. [22], and the realization of multiple BECs of ^{87}Rb $|F = 1, m_F = -1\rangle$ atoms was demonstrated in the work of Jose et al. [32] and Surendran et. al [33].

According to our calculations, the tunnelling time in a 10 μm-period magnetic lattice with a barrier height of only 0.21 mG would be about 100 s. This time is considered to be too long and all the atoms trapped in the magnetic lattice would be lost before any tunnelling could occur. In order to perform tunnelling experiments in a magnetic lattice, it is required to scale down the lattice period to less than about 1 μm. By decreasing the lattice period, one can increase the energy scales in the Hubbard model used to describe quantum gases in optical lattices [17, 26], which consequently increase the tunnelling rate and the on-site interaction [102]. Our calculations show that for a 0.7 μm-period lattice, the tunnelling times are 9 ms and 2 ms for barrier heights $V_0 \sim 12E_r$ (20 mG) and $6E_r$ (10 mG), respectively (Sect 2.7).

This chapter presents the fabrication and characterization of the new sub-micron-period magnetic lattice structures on a Co/Pd multilayer magnetic film. Also, the fabrication of a direct-bonded copper (DBC) atom chip containing current-carrying wire structures is presented. The fabricated magnetic film is glued onto the DBC atom chip to create a magnetic lattice atom chip which is the crucial component of our experiment. In the final part of this chapter, a newly fabricated improved DBC atom chip for future use is described.

The Co/Pd film was provided by M. Albrecht from the University of Augsburg in Germany. The magnetic film fabrication was performed in the nano-fabrication facility in the Centre for MicroPhotonics at Swinburne University of Technology and at the Melbourne Centre for Nanofabrication at Monash University by Pierrette Michaux, Amandas Balcytis and Saulius Juodkazis. The Monte-Carlo simulation shown in Figure 3.14 was provided by Amandas Balcytis. The fabrication quality test, the characterization of the sub-micron magnetic lattice film and the installation of the combined magnetic lattice atom chip in the experimental system was carried out jointly with Yibo Wang. I independently performed the design and the fabrication of the new improved DBC atom chip.

3.2 Direct Bonded Copper atom chip

3.2.1 Design and fabrication

On the old-generation atom chip used for the 10 μm-period 1D magnetic lattice, the designed wire structure was micromachined on a silver foil and glued on a Shapal-M machinable ceramic plate with a high vacuum thermal conductive epoxy. The advantage of this chip is the ability of the wires to carry a high current (up to 40 A) without noticeable heating. However, the thermal conductivity is limited due to the epoxy. Additionally, the silver/ceramic is not strongly bonded which can lead to delamination of the silver wire during machining. To overcome these problems, a new-generation atom chip using a Direct-Bonded Copper (DBC) substrate, a UHV compatible material, is employed [104, 105]. DBC is the direct joining of a thin sheet of pure copper to a ceramic substrate of AlN by heating to $\sim$ 1065 °C in an environment of $\sim$ 1.5% oxygen and $\sim$ 98.5% nitrogen. The DBC process is based on the fact that oxygen reduces the melting point of copper from 1083°C to 1065°C (the eutectic melting temperature). By pre-oxidizing copper foil and aluminum nitride ceramic, then injecting oxygen during high temperature annealing between 1065°C and 1080°C, a thin layer of copper-alumina-spinel forms thereby creating a direct bond between the copper and the ceramic. Compared to the silver-foil atom chip, the DBC chip provides much stronger bonding, better thermal properties and similar high current handling while the fabrication is much simpler.

At first, a mask with wire patterning is applied to the surface of a DBC board after spin-coating a 20 μm-thick layer of positive photoresist (AZ4620). Afterwards, ultraviolet (UV) photolithography is employed to transfer the wire pattern to the desired side of the DBC board. In the next step, the DBC board is immersed in a 10% ammonium persulphate solution at 60 °C for wet etching. After several hours, the copper is etched away from the exposed areas which leaves wire traces on the AlN subtrate. Finally, the board is ultrasonic cleaned with acetone.

Our fabricated DBC atom chip size is 50 mm $\times$ 55 mm which is fabricated from

a large 127 μm-thick DBC + 635 μm AlN + 127 μm-thick DBC board from Stellar Ceramics. A drawing of the front and rear of the designed DBC atom chip is shown in Figure 3.1. The chip is designed with four separated 1 mm-wide, 5 mm-long U/Z-wire structures. Different wire configurations for four lattice structures can be easily arranged by connecting the corresponding pin holes. Different U-wires and Z-wires are configured by connecting the pin holes 1, 2, 3, 5, 6, 7 and 10. In the design, two 3.4 mm-long $\times$ 0.5 mm-wide RF wires are included for the evaporative cooling procedure and RF spectra measurements. The RF wires are configured by connecting pin holes 3, 4 and 8, 9.

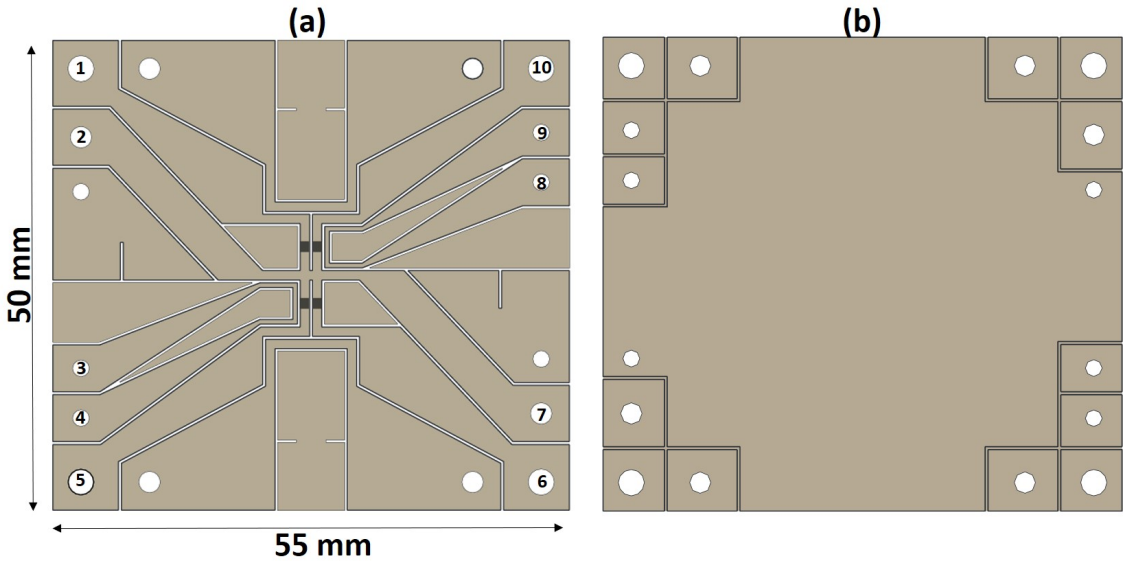

Figure 3.1: Drawing of the front (a) and rear (b) of the designed DBC atom chip.

For attaching the magnetic film onto the atom chip, two separated holes, which are not numbered in Figure 3.1, are drilled. Also, two markers for aligning the fabricated magnetic film when being glued onto the DBC atom chip are employed. In conjunction with the atom chip, a pure copper block for heat dissipation is designed to match the rear face of the atom chip while avoiding short-circuit problems.

3.2.2 Quality check and assembly

To check the fabrication quality, a UHV compatibility test and a heat dissipation measurement are performed. For the UHV test, the new chip is installed in a separate vacuum chamber and baked at $\sim 100\,^{\circ}\mathrm{C}$ for 4 days to pump out water vapour and other gases. After the chamber cooled down to room temperature, the pressure measured inside the chamber was 10^{-12} mbar which indicated a good UHV compatibility of the chip.

For the heat dissipation test, as shown in the Figure 3.2, constant currents are passed through the U/Z wires and the voltage behaviour is recorded to examine the evolution of the resistance. After 5 minutes of running high currents (40 A and 60 A) through the Z/U wires, the resistance of the wires increased by less than 20% which indicates that the temperature increase is not too high to damage the copper wires ($\Delta T = 57°\mathrm{C}$ and $82°\mathrm{C}$ for 40 A and 60 A respectively) [106].

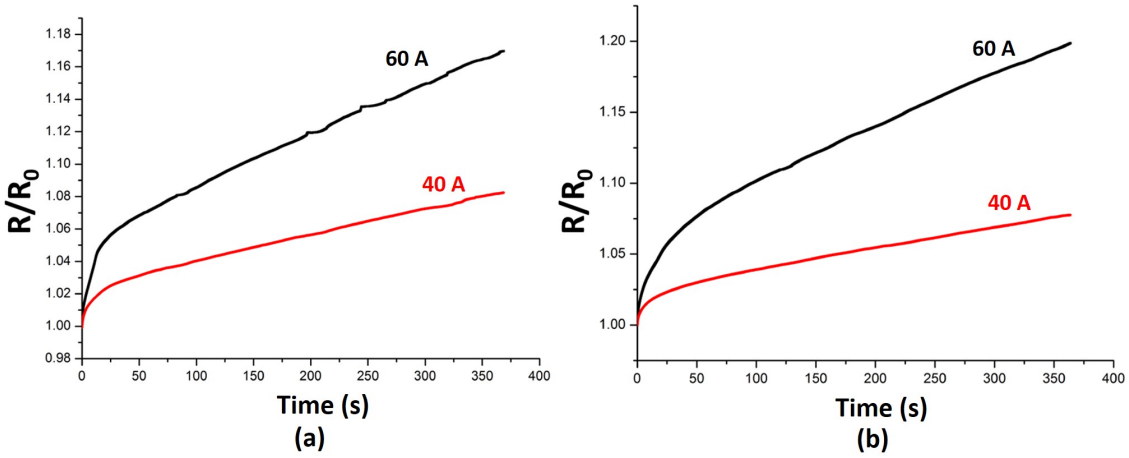

Figure 3.2: Evolution of (a) the Z-wire resistance after passing a current of 40 A (red line) and 60 A (black line) and (b) the U-wire resistance after passing a current of 40 A (red line) and 60 A (black line). The initial jump is attributed to heating of the wire and the barrel connector connection.

For assembly of the hybrid magnetic lattice chip, at first a UHV compatible glue (Epotek H77) is employed to attach the fabricated magnetic film to the DBC atom chip with an estimated error of $\pm 1\,\mathrm{mm}$. This is done by first applying a thin,

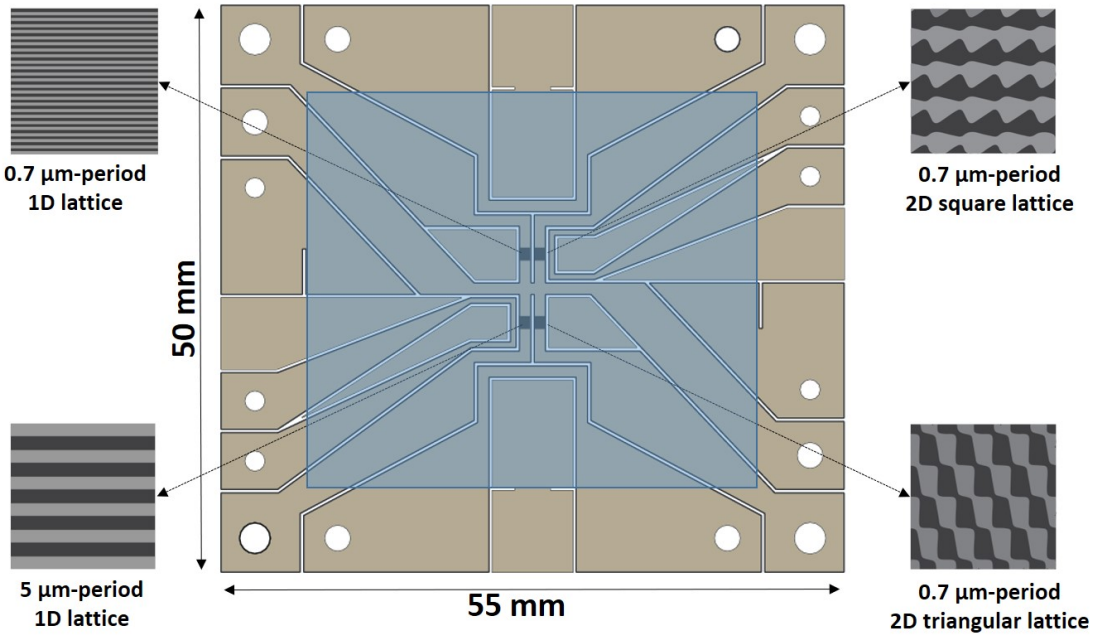

Figure 3.3: Schematic drawing of the layout of the hybrid atom chip with the magnetic lattice film.

flat layer of the epoxy to cover the desired magnetic film region. After precisely positioning the fabricated magnetic film, the whole structure is heated to $\sim 110\,^{\circ}\mathrm{C}$ for one hour to form a strong bond. The hybrid magnetic lattice chip is then pre-baked in a separate UHV chamber at $\sim 110\,^{\circ}\mathrm{C}$ for two days to remove undesired gas and water vapour. The complete hybrid atom chip system is shown in Figure 3.3.

3.3 Fabricated magnetic film characterization

After the magnetic film fabrication procedure, SEM measurements, which show the surface topology (Figures 3.4, 3.5, and 3.6), were performed. The results show satisfactory 1D, 2D square and triangular lattice patterned structures. In addition, Magnetic Force Microscope (MFM) measurements were performed for an evaluation of the magnetic field map of the fabricated magnetic film. At first, a fabricated sample is magnetized and then scanned in dynamic mode (AC mode) to increase the signal-to-noise ratio. This mode provides a measure of the phase difference

between the oscillating cantilever and the sample. The magnetic tip operating in semi-contact mode scans over the magnetized sample while oscillating at its resonant frequency with a small amplitude in the vertical direction. The tip-surface distance is set to be larger than the tip size so that the tip can be treated as a point dipole oriented along the z-direction.

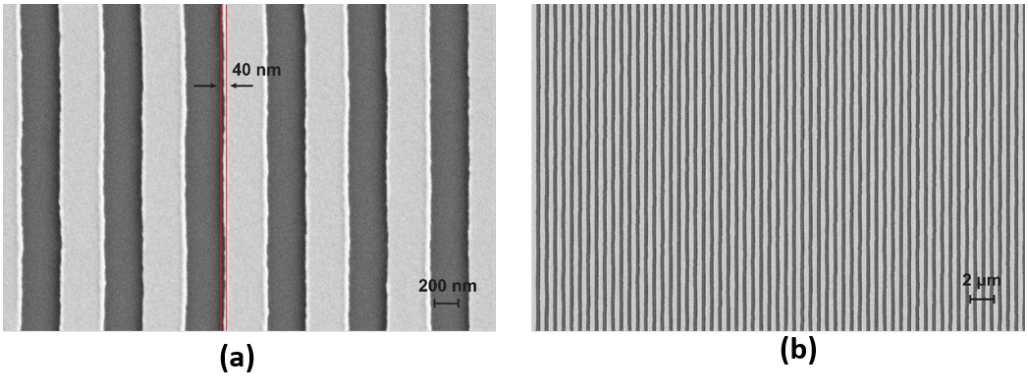

Figure 3.4: Small-scale (a) and (b) large-scale SEM images of the 1D 0.7 μm-period magnetic lattice structure showing an edge roughness of 40 nm and a multiple trench period of 688 nm [17]. Dark regions represent the etched regions and light regions represent the unetched magnetic regions.

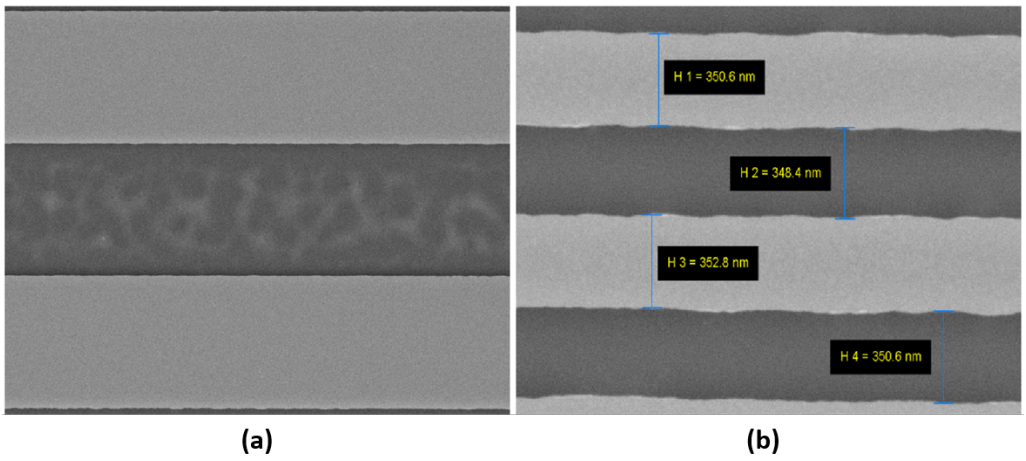

Figure 3.5: SEM images showing the patterns of the 1D 5 μm-period (a) and 1D 0.7 μm-period (b) magnetic lattice structures showing the etched (dark regions) and unetched magnetic (light regions) regions.

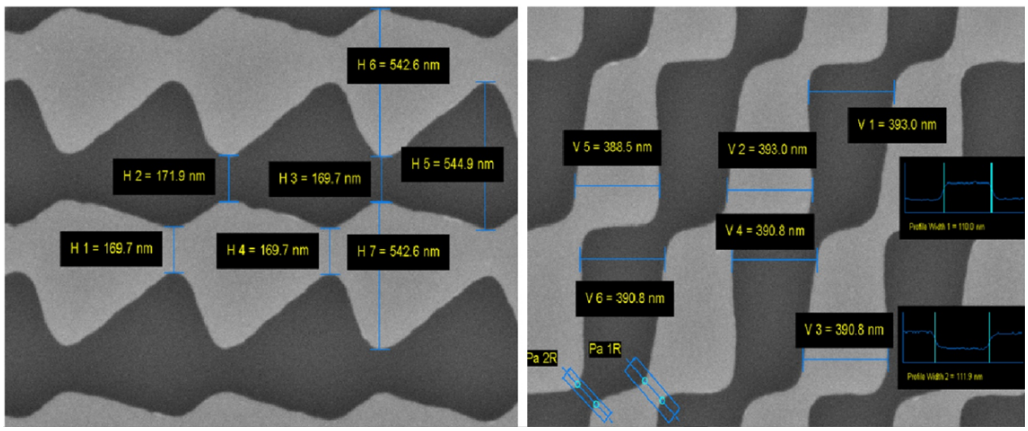

Figure 3.6: SEM images showing the patterns of the 2D 0.7 μm-period square (a) and triangular (b) magnetic lattice structures. The etched regions are the dark regions and the unetched magnetic regions are the light regions.

To lowest order, the magnetic force causes a phase shift [17]:

$$\Delta\phi \approx \frac{Q}{k_s}\frac{\partial F_z}{\partial z} \propto \frac{\partial^2 B_z}{\partial z^2}, \tag{3.1}$$

where k_s is the spring constant and Q is the cantilever quality factor. The shift in the resonant frequency caused by the tip:

$$\Delta f \approx -\frac{f_n}{2k_s}\frac{\partial F_z}{\partial z} \propto \frac{\partial^2 B_z}{\partial z^2}, \tag{3.2}$$

where f_n is the natural resonant frequency of the cantilever tip [107].

The MFM signal is proportional to the second spatial derivative of the z-component of the magnetic field, which in the case of 1D structures, is dependent on the oscillating signal in the y-direction with period given by the lattice period. As the distance from the cantilever tip to the surface of the magnetized sample increases, the amplitude of the oscillating signal decays with the decay length $k^{-1} = a/2\pi$, where a is the lattice period. The dependence of the amplitude of the oscillating MFM signal on this distance is examined for an evaluation of the magnetic quality of the structures. The oscillating profile shown in Figure 3.7 gives $a_{osc} = 651 \pm 3$ nm while the fitted decay length gives a value $a_{osc} = 662 \pm 11$ nm, where the uncertainties

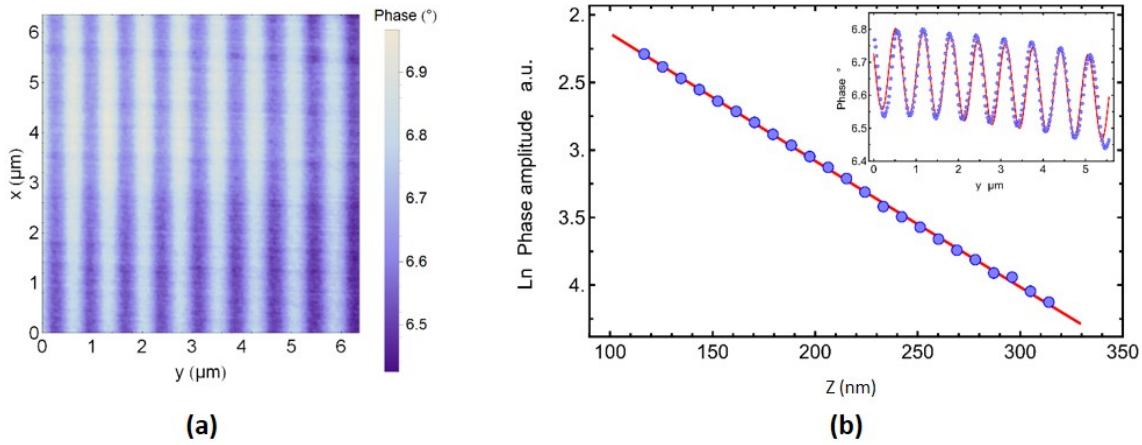

Figure 3.7: (a) MFM image of the 1D 0.7 μm-period magnetic lattice structure using a probe tip height of 50 nm. (b) Plot of the natural logarithm of the MFM signal amplitude versus tip-surface distance z showing a fitted decay curve (red line). Inset: Plot of the profile of the MFM signal in the y-direction at a tip-surface distance of 50 nm showing the fitting (red curve) of the oscillating signal [17].

represent the residuals of the fits. These values are in reasonable agreement with the SEM tests showing a measured period of 688 nm, as can be seen in Figure 3.4, which confirms the fabrication quality of the structure.

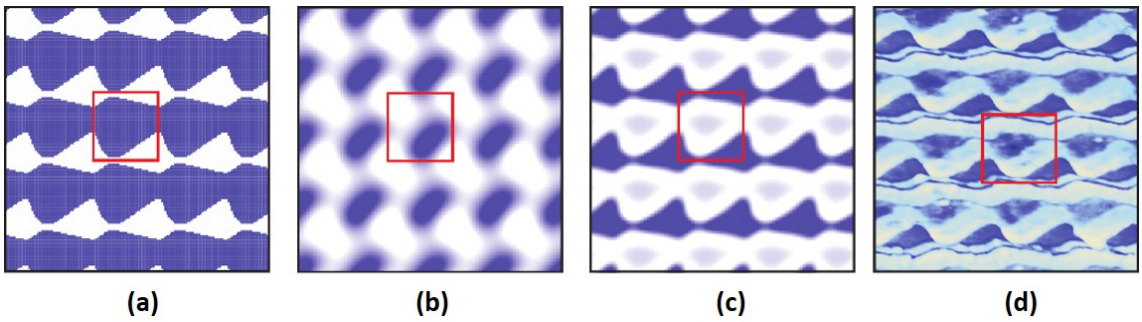

Figure 3.8: (a) Optimized pattern of the square magnetic lattice structure produced by the Schmied et al. code [28] and (b) calculated magnetic potential at a trapping height $z = a/2$. (c) Calculated second derivative of B_z. (d) MFM measurement of the 0.7 μm-period square magnetic lattice structure. The red square shows one unit cell [17].

For an evaluation of the magnetic properties of the fabricated structures, the second derivative of the calculated magnetic field is analyzed and compared with the MFM measurements of the patterned Co/Pd stack (Figure 3.8). Qualitatively, the calculated second derivative and the MFM measurement results are generally in agreement except that there are some sharp horizontal lines in the MFM measurement at some boundary edges. These are attributed to magnetic domain formations of the structure or to possible errors in the MFM measurements caused by changes in the surface topology at the edges.

3.4 Two-dimensional magnetic lattice structures

3.4.1 Co/Pd magnetic film

The fabrication of the first version of the sub-micron period magnetic film structure, a promising candidate for experiments involving quantum tunnelling, was completed in 2015 [17]. Thanks to big advances in materials science, a new state-of-the-art magnetic material comprising alternating atomic bilayers of a ferromagnetic transition metal Co and a noble metal Pd was used to replace the $Tb_{10}Gd_6Fe_{80}Co_4$ magnetic film.

Compared to the rare-earth transition metal film, the Co/Pd magnetic film has a larger perpendicular magnetic anisotropy (PMA), larger remanent magnetization, higher Curie temperature, smaller grain size (6 nm compared to ∼40 nm for $Tb_{10}Gd_6Fe_{80}Co_4$) [17] and large Kerr rotation at short wavelengths. These properties were considered for their key roles in producing smooth, homogeneous magnetic potentials and dense magnetic microtraps to trap atoms in submicron-period arrays.

For the Co/Pd structure, the thickness of the Co layer and the Pd layer and the total thickness of the stack of Co/Pd layers can be varied to obtain the desired thermomagnetic properties. For the Co magnetic layer, the thickness is chosen to be approximately two atomic layers (< 4 nm) so that its easy magnetization axis aligns perpendicularly to the structure plane and when configured with Pd layers it

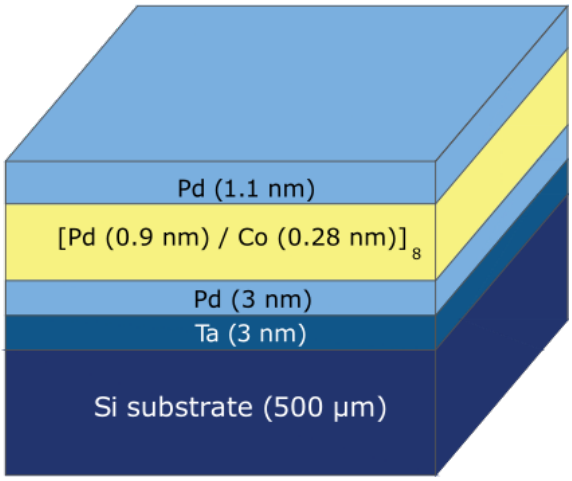

Figure 3.9: Multilayer structure of the Co/Pd magnetic film. Adapted from [17].

will create optimal interface anisotropy. For the Pd layer, the thickness is chosen to be < 1 nm so that when configured with the neighbouring Co magnetic layers on the top and bottom creates an enhanced magnetization [108]. For optimal magnetic properties of the structure, the total thickness (Co plus Pd) should be 10-30 nm.

A schematic of the new multilayer Co/Pd magnetic film is shown in Figure 3.9. The magnetic film consists of a total of 8 bilayers of alternating Co (0.28 nm) and Pd (0.9 nm) with a 1.1 nm-thick layer of Pd on the top to protect from oxidation and a 3 nm-thick layer on the bottom. The number of bilayers can be varied to obtain a high surface magnetic field or a high perpendicular magnetic anisotropy (PMA) within a trade-off relation. This stack is deposited onto a 330 μm thick Si(100) substrate through a seed layer of 3 nm-thick Ta to provide a good texture for the deposition which leads to an improvement of the PMA and the crystallographic orientation of the layers.

For the deposition of the Co/Pd multilayers at room temperature, a DC magnetron sputter-deposition method is employed in which the argon pressure was set at 3.5×10^{-3} mbar during the whole deposition procedure and the base pressure inside the deposition chamber was 1.0×10^{-8} mbar. For accurate control of the deposition thickness, a quartz microbalance was used in conjunction with X-ray reflectometry measurements on the Co/Pd samples for calibration purposes.

3.4.2 Co/Pd magnetic film characterization

The magneto-optical Kerr effect (MOKE), which measures the degree of rotation of linearly polarized light reflected from a magnetized surface, was employed for quantitative analysis of the coercivity, the remanence ratio and the perpendicular magnetization hysteresis loop. The Kerr rotation is proportional to the surface magnetic moment and is dependent on the magnetic composition, the magnetization direction, the coating layer of the film, the angle of incidence and the probe wavelength.

For the MOKE measurement setup, the film stack is magnetized in a perpendicular direction in a strong external magnetic field generated by a manually operated 1.5-inch electromagnet which can provide a maximum magnetic field up to 1 Tesla. Linearly polarized light, produced by passing the output of a diode laser source (780 nm) through polarizing optics, shines at an angle of 45^0 to the magnetic film and experiences a rotation of the polarization plane when reflected from a magnetized surface. The photodiode signal versus magnetic field strength is recorded on an oscilloscope and post-analyzed for a complete hysteresis loop as shown in Figure 3.10. The measured hysteresis loop of the Co/Pd film is almost perfectly square with a coercivity of $H_c = 1.0\,\mathrm{kOe}$.

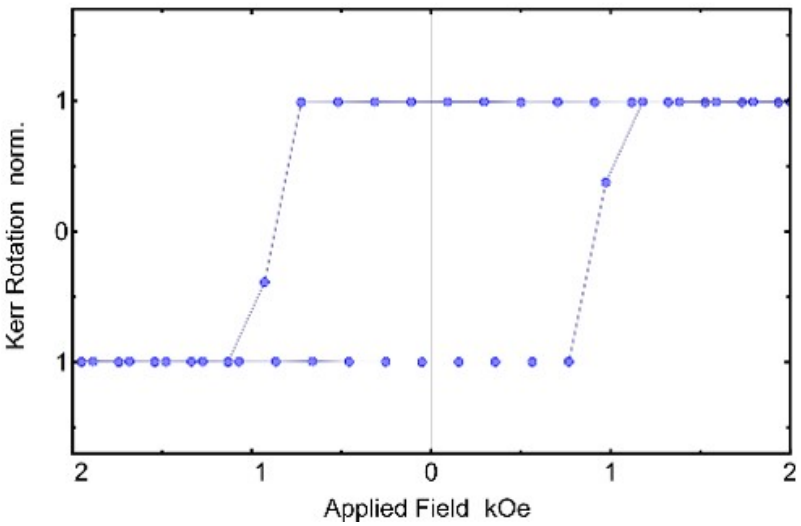

Figure 3.10: Magneto-optical Kerr effect hysteresis loop of the Co/Pd film [17].

For quantitative information of the magnetization and the in-plane hysteresis, a superconducting quantum interference device (SQUID, Quantum Design MPMS5) was employed. The result provided by staff at the University of Augsburg in Germany gives a saturation magnetization of the Co/Pd film of $4\pi M_s = 5.9\,\mathrm{kG}$.

Scanning Electron Microscopy (SEM) measurements were performed for an evaluation of the Co/Pd film surface. A SEM image of the Co/Pd film is shown in Figure 3.11 (a). The SEM tests show a good homogeneity of the material and a practical grain size of about 10 nm, compared to the nominal value of 6 nm. This small grain size is considered to be suitable for the fabrication of sub-micron scale magnetic lattice structures.

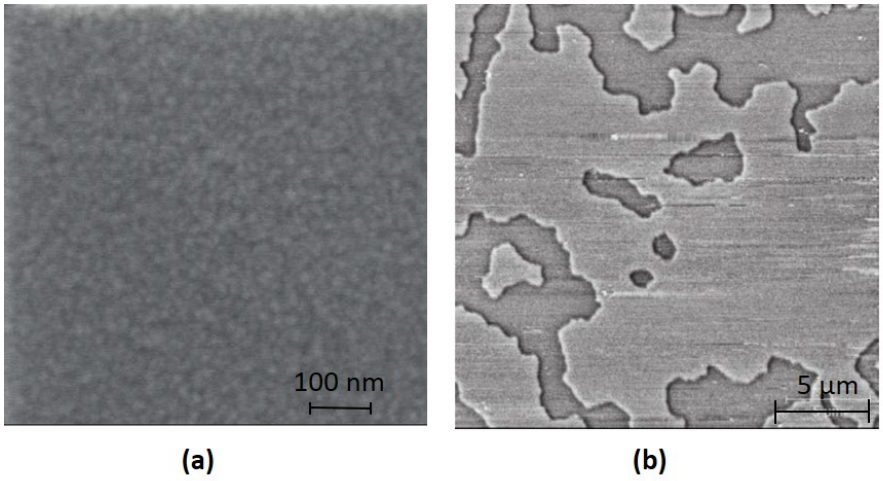

Figure 3.11: (a) SEM image of the Co/Pd film showing the material homogeneity and an average grain size of about 10 nm, (b) MFM image of the Co/Pd film in the demagnetized state showing magnetic domains with a typical size of 5 μm [17].

An atomic/magnetic force microscope (AFM/MFM) was employed for analyzing the magnetic properties of the fabricated Co/Pd film which operates in two passes. In the first pass, which is operated in the semi-contact mode, a magnetic CoCr coated cantilever periodically taps the surface to map out the surface topology of the sample. In the second pass, which is operated in the non-contact mode, the cantilever scans over the sample at a constant height from the surface to produce a magnetic force signal. A MFM image of the Co/Pd film in the demagnetized state,

which was provided by staff at the University of Augsburg in Germany, is shown in Figure 3.11 (b). Due to the strong PMA, large magnetic domain structures with magnetization pointing up or down perpendicular to the film plane are observed in island shapes. To test the longevity of the PMA properties, the measurements were repeated after several months. No significant change in the domain structure shape and position is observed, which indicates a stable and strong PMA of the Co/Pd film.

3.4.3 Design and fabrication

The optimization algorithm developed by Schmied et al. [28] was used to calculate the desired magnetic lattice geometries (Section 2.6.1). For our experiment, a new 35×40 mm^2 Co/Pd magnetic film was designed which contains four 1 mm×1 mm magnetic lattice structures: one 5 μm-period 1D lattice, one 0.7 μm-period 1D lattice, one 0.7 μm-period 2D square lattice and one 0.7 μm-period 2D triangular lattice, as shown in Figure 3.12. The 5 μm-period 1D lattice is included for system optimization while the other three 0.7 μm-period lattices serve as platforms for performing the main experiments.

For the fabrication of the new magnetic film, e-beam lithography (EBL) followed by reactive ion etching (RIE) microfabrication techniques were chosen for their high resolution, high versatility and the flexibility to produce arbitrary submicron scale magnetization patterns [32]. In the preparation stage, a Co/Pd film-coated wafer was wet cleaned in the solvents acetone, isopropanol and methanol, using an ultrasonic cleaning method. After that, dry nitrogen was employed to blow-dry the wafer, which was later heated on a 180 °C hot-plate for 3 minutes to vaporize the remaining solvents.

The fabrication procedure, shown in Figure 3.13, started by spin-coating the wafer with a 300 nm-thick layer of polymethyl methacrylate (PMMA) resist. In the second step, EBL, a maskless direct-write method using electron beams focused on an electron-sensitive resist to generate the desired patterns on the Co/Pd film,

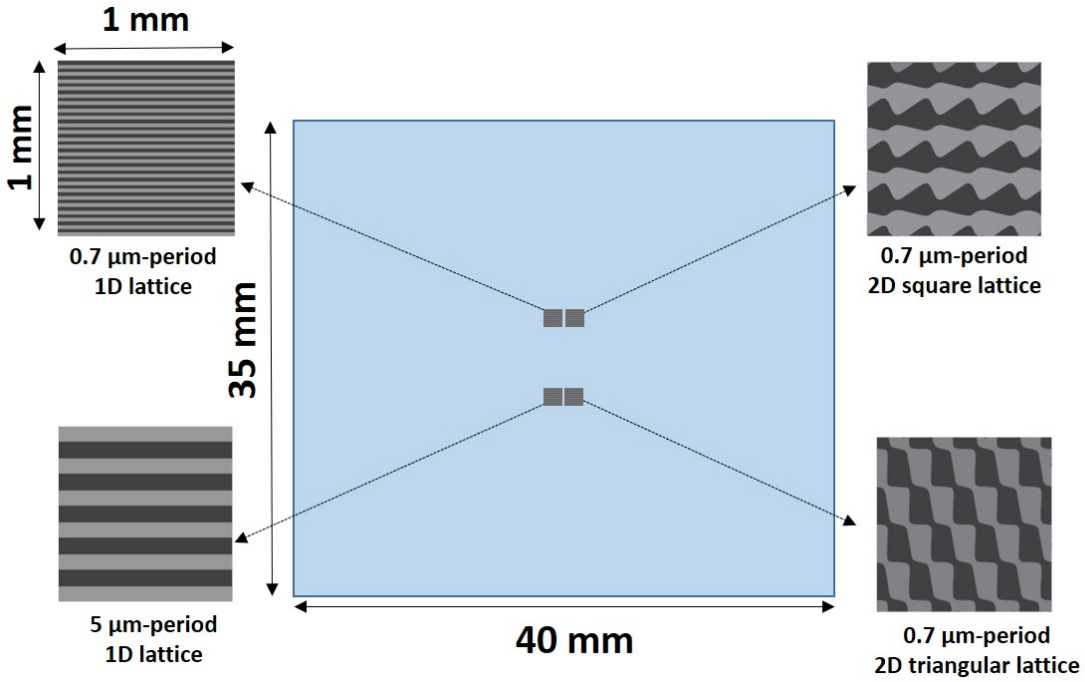

Figure 3.12: Schematic diagram of the magnetic lattice structures on the Co/Pd film.

was employed using a Raith EBPG5000plusES EBL exposure tool. The machine operates at 100 kV electron acceleration voltage and is capable of writing an area of 1 mm^2 all at once, which is considered sufficient for writing an entire magnetic lattice structure, thereby eliminating the need for stitching blocks. The exposure rate for the patterning is determined based on the complexity and the geometry of the lattice structures. Using a 5 nm full-width half-maximum electron spot size operating at 50 MHz rate, the exposure time ranges approximately from 30 mins for the 1D 0.7 μm-period grating structure to 120 mins for the 2D 0.7 μm-period structures. Afterwards, the resist is immersed for 80 seconds in a mixture of isopropanol and methyl isobutyl ketone with a proportion of 3:1 to develop the pattern. This step is necessary to avoid solubility of the patterned area due to the broken bonding of the polymer chains caused by the energetic electrons. Next, the resist is immersed in the isopropanol again to stop any further pattern development, and then blow-dried with dry nitrogen.

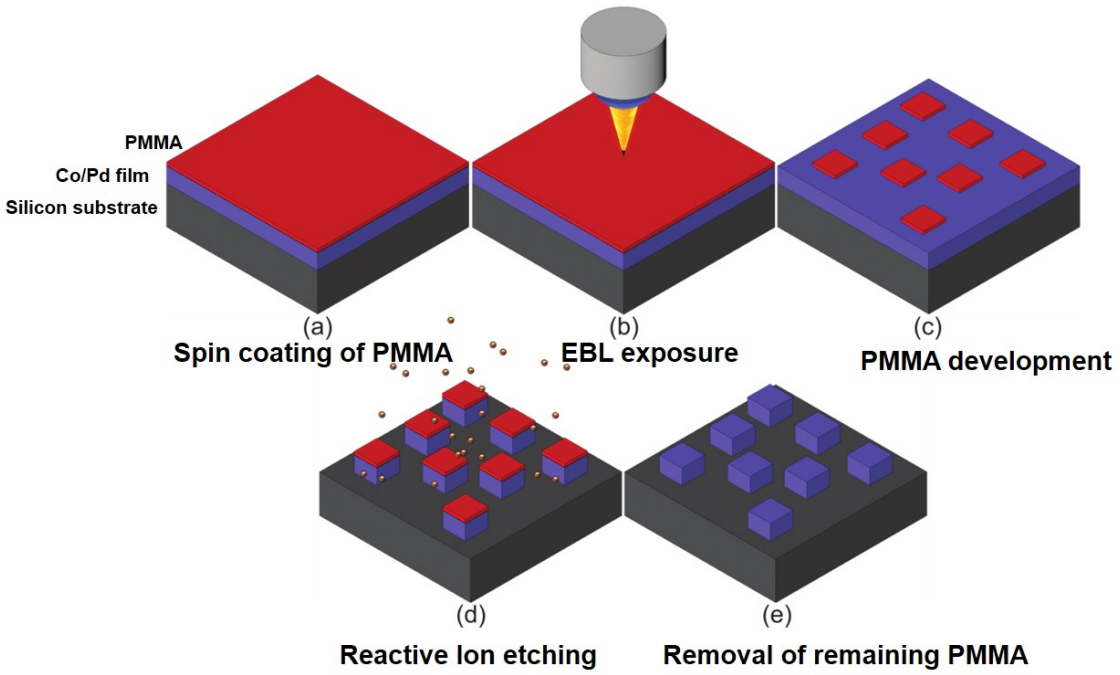

Figure 3.13: Patterning sequence of the Co/Pd magnetic film [17].

In the next step, an inductively coupled plasma reactive ion etching tool (Samco RIE-101iPH) is employed for dry-etching purposes. During this procedure, the machine first produces an environment of argon ions (Ar^+) which is subsequently used for bombardment via physical sputtering. The remaining PPMA resist layer after the resist development stage acts as a protective coating from the argon ion bombardment while in the exposed area the film is etched until it reaches the Si layer of the magnetic film stack. A $\sim 25\,\text{nm}$ etch depth is chosen to ensure the magnetic film is completely removed from the non-magnetic zones to produce binary patterns. In the next stage, the remaining PMMA resist is removed by immersing the wafer in acetone at $60\,^{\circ}\text{C}$.

Subsequently, an AXXIS (K.J. Lesker) physical vapour deposition system is employed to coat the magnetic film with a 50 nm gold reflecting layer via magnetron sputtering. In this way, the gold fills the etched gaps which helps to flatten the film surface. The high reflectivity gold layer acts as a mirror which is required for creating the mirror-MOT and for reflective absorption imaging of the atom clouds. Then, a 25 nm SiO_2 layer is deposited by electron-beam evaporation to prevent

rubidium atoms from reacting with the gold surface. In the final stage, the wafer is trimmed to $35 \times 40\,\mathrm{mm}^2$ size using a 1030 nm femtosecond laser beam (PHAROS, Light Conversion) before being ultrasonic cleaned.

3.4.4 Proximity effects

The proximity effect is a deformation of the structure towards the edges when the EBL exposure is performed on large areas. During our magnetic film fabrication, there is a non-uniformity in the pattern structure, increasing from the centre area towards the edge of the film.

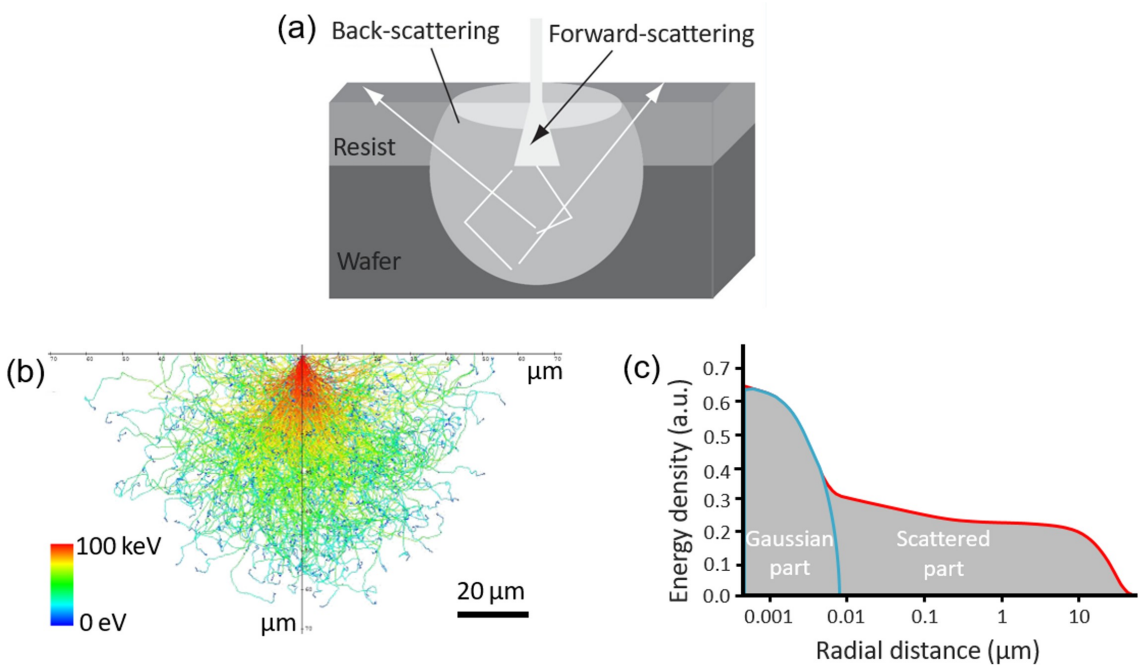

Figure 3.14: (a) Schematic representation of the electron spread due to forward-scattered and back-scattered electrons, (b) Monte-Carlo simulation of the trajectory spread of 10^6 electrons, (c) Energy density distribution along the radial direction of the electron beam in semi-log scale. The Gaussian part is created from the normal beam and the broad pedestal part is created from the scattered electrons responsible for proximity effects.

The non-uniformity is attributed to electron scattering as the electrons hit the resist-coated substrate (Figure 3.14 (a)). As a consequence, electrons are spread

over a large area compared to the initial 5 nm spot-size. The scattered electrons create a parasitic effect on the areas around the region being etched which changes the resist dissolution rate and the partially developed patterns. When a uniform dose distribution is used, this can cause a change in the desired patterns (Figure 3.14 (b)).

To compensate for this error, a dose scaling method is employed, in which the dose distribution is modified for different exposure areas. At first, Monte-Carlo simulations are performed to simulate the scattering of electron beams during the lithography procedure to generate a point spread function. Based on this, the dose is modified correspondingly to compensate for parasitic exposure. As a result, the base dose at the periphery region is considerably larger than the base dose in the central area. In our case, in a ~ 25 μm wide periphery region, it is required to add $0.5 \times$ the base dose to avoid the proximity effect for a 1 mm $\times$ 1 mm EBL exposure area (Figure 3.14 (c)).

3.5 New DBC atom chip

In our current atom chip (Figure 3.1), the chip wires are designed with mainly diagonal wires which creates a spatially non-uniform magnetic field component. This can affect the lattice loading in our present experiments since our magnetic lattice is very sensitive to changes in magnetic field . In this new chip, I have designed current-carrying wires that are optimized by employing more symmetric and perpendicular wires so that the bias field created from secondary current-carrying wires spatially cancel each other resulting in a more stable magnetic field environment for trapping and loading the atoms. Compared to the previous DBC atom chip, the width of current-carrying wires on the new DBC chip are three times smaller which can induce a three times larger resistive heating on the same current.

The new chip was fabricated in direct bonded copper (DBC) to our design by the company REMTEC Industries [109], USA using specialized and high precision fabrication facilities and procedures. The wire etching techniques can produce a 0.25

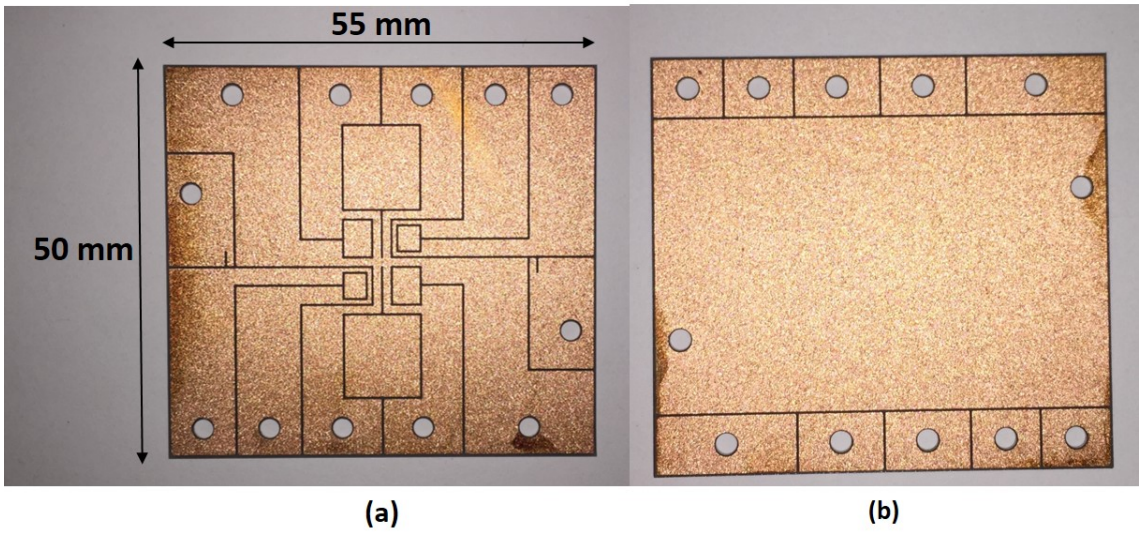

Figure 3.15: Photos of the front (a) and rear (b) face of the new fabricated DBC atom chip.

mm copper trace width with a typical tolerance of 0.1 mm. As atoms are trapped very close to the chip surface, any wire fabrication defects can alter the trapping potential of the atoms. The final fabricated DBC chip is shown in Figure 3.15.

The etching procedure is described as follows:

In a clean room environment both sides of the copper clad ceramics are laminated with a UV-sensitive dry film photoresist $\sim$40 - 100 μm thick depending on the circuit complexity. A photo tool is placed over the laminated copper substrate and exposed to high-intensity collimated light with a wavelength of 350 - 420 nm. When exposed, the photo tool negative selectively lets light pass through the tool to harden the exposed photoresist.

The exposed substrates are then moved to wet processing and passed through a neutralizing sodium developer solution which reacts with the unexposed photoresist allowing it to become soluble and to be removed through rinsing. The remaining hardened photoresist coats the copper substrate with a positive image of the desired circuit. Unwanted copper around the desired circuit is removed through a subtractive spray etch process using cupric chloride solution. The remaining positive copper pattern then passes through a mildly alkaline caustic solution allowing the

remaining photoresist to be dispersed into a stripping solution or dissolved before the substrate is rinsed and thoroughly dried.

The patterned parts are surface-plated to customer specifications by typically depositing electrodeless nickel mid-phos ($\sim$ 6 - 10% phosphorus by weight) 2.5 - 8 μm thick followed by an immersion gold $\sim$0.01 - 0.15 μm thick to reduce the potential for oxidation of the nickel surface. The patterned parts that are to be left in the bare copper are subjected to a final cleaning process and then the copper is passivated in citric acid or other anti-tarnish solutions.

Finally, the patterned and plated substrates are laser-scribed using a CO_2 laser equipped with Automatic Optical Pattern Recognition (AOPR) to align and score the ceramic along the designated boundaries of individual cells. The scored substrates are cleaned to remove any residual contamination from the scribing process, to singulate and cut individual finished cells from the master substrate array.

Finished individual cells are packaged with a corrosion inhibitor and placed into metallized-foil bags which are then purged with nitrogen and vacuum-sealed creating an anti-corrosive environment to ensure product reliability and solderability.

CHAPTER 4

Experimental setup

This chapter describes the technical details of our magnetic lattice trapping experiment including the patterned magnetic lattice film on the DBC atom chip mounted inside an ultra-high vacuum chamber, the laser system layouts, and the experimental control system. Also, the experimental procedure to obtain Bose-Einstein condensation of ^{87}Rb $|F = 1, m_F = -1\rangle$ atoms in the Z-wire trap on the atom chip is presented.

The current experimental setup was partly modified, developed and optimized from the experiment system built by former students in our group [58–61]. The installation of the new fabricated magnetic lattice and atom chip (described in Chapter 3) in the UHV chamber, which was carried out jointly with PhD student Yibo Wang, is described. Also, my independent work of optimizing the experimental setup, achieving BEC in the Z-wire magnetic trap and other measurements with this experimental system is described.

4.1 Ultrahigh vacuum chamber

An ultra-high vacuum (UHV) system, used for isolating the trapped atoms from the environment, is one of the most important apparatuses for our ultracold atom experiment setup. We need to have good control of the vacuum conditions in the

chamber in order to prevent collision losses of the trapped atoms with background gases (H_2, CO, CO_2, N_2, H_2O, etc.) and to maintain long trapping lifetimes of atoms in the magnetic traps.

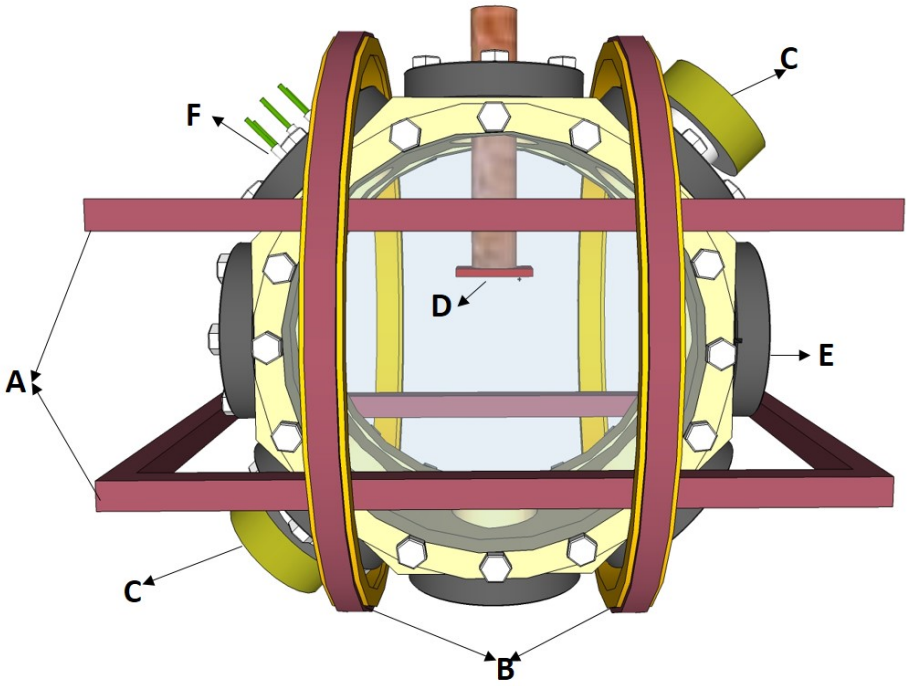

Figure 4.1: Schematic drawing of the vacuum chamber with atom chip and magnetic coils. A: compensation coils, B: B_x large coils, C: quadrupole coils, D: atom chip, E: connections to vacuum pumps, F: electrical feedthrough connections to the atom chip.

In our experiment setup, we use a single 316L non-magnetic stainless steel vacuum chamber with octagonal geometry (MCF600-SO200800 Kimball Physics Inc.) with 10 conflat ports. The ten conflat ports include two 6″ diameter antireflection-coated viewports on two sides of the UHV chamber, one 2.75″ diameter port for mounting the atom chip, two 2.75″ diameter ports for mounting electrical feedthroughs to provide electrical connections to the atom chip and the remaining five 2.75″ diameter ports for optical access and pumping purposes. In our experiment, the atom chip is mounted upside down with a 20 mm-diameter solid copper rod for heat conduction. A schematic drawing of the vacuum system and magnetic coils is shown in Figure 4.1.

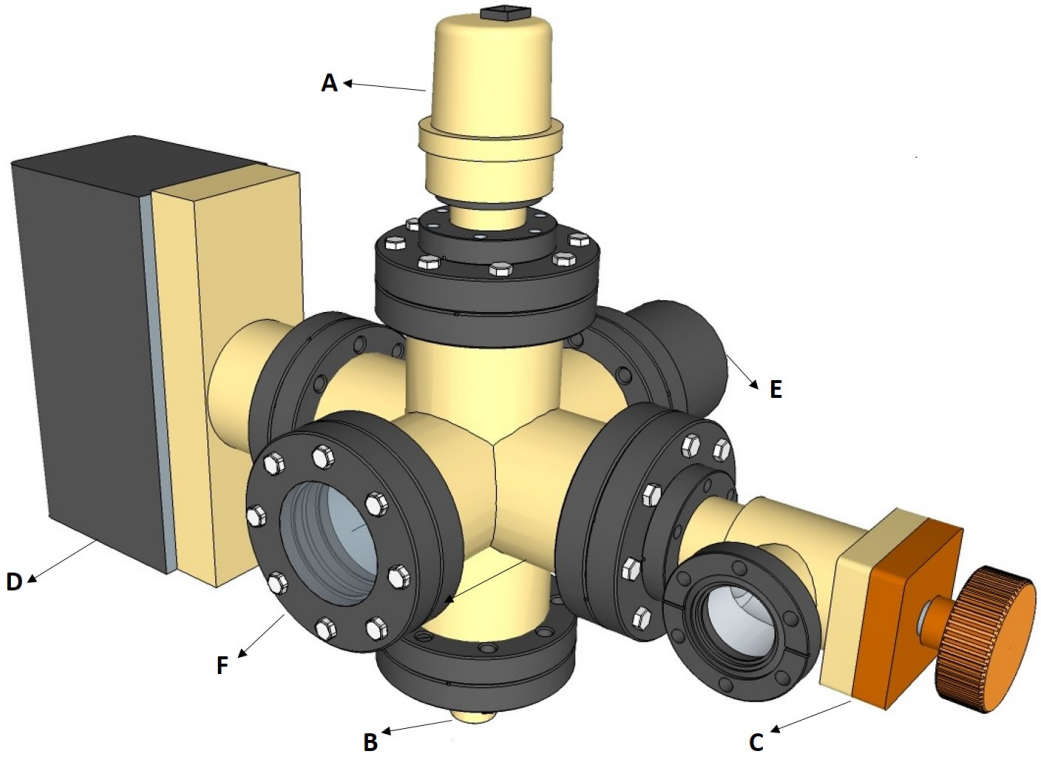

Figure 4.2: Schematic drawing of the vacuum pumps. A: cold cathode gauge, B: getter pump, C: all-metal angle valve, D: ion pump, E: connection to UHV chamber, F: access viewport for optical beams.

A stable pressure below 10^{-11} mbar inside the UHV chamber is required for maintaining a long trapping lifetime of atoms in the magnetic traps. To achieve this vacuum, we first perform a baking procedure, in which the vacuum chamber and components are baked at a temperature of 110°C for one week. During this period, a turbo molecular pump (Pfeiffer TMU065) and a diaphragm pump are used to pump out the system. The baking procedure is carried out at a relatively low temperature to avoid demagnetization of the magnetic film and at a low heating rate to avoid damage to the chip. After this process, the vacuum is maintained using a SAES getter pump (CapaciTorr D 400-2) and an ion pump (Varian Starcell VacIon Plus 55) at a pumping speed of 50 l/s. Use of 4 pumps can help to remove all gases more efficiently which helps to achieve a good vacuum inside the UHV chamber. During

the whole procedure, all pressure measurements are performed using a cold cathode gauge (Pfeiffer IKR-270). A similar baking-out procedure is described in detail in the thesis of Mandip Singh [58]. A schematic diagram of the vacuum pump system is shown in Figure 4.2.

4.2 Laser optical system

4.2.1 Trapping laser

In our experiments, a total of four laser beams at different frequencies including trapping, repumper, optical pumping and imaging beams are used. To avoid stray, scattered light to the UHV chamber, a separate optical table for the laser systems is used. These beams are then directed to the UHV chamber on another optical table through polarization-maintaining optical fibres. In order to reduce mechanical vibrations and associated noise, the optical table is floated on a compressed air system. Also, the laser-system table is covered with a perspex box to improve laser-head temperature stability for optimal usage.

The energy level diagram of the ^{87}Rb D_2 line is illustrated in Figure 4.3 and a schematic diagram of the trapping laser optics is shown in Figure 4.4. The trapping beam is derived from a tapered amplifier diode laser (Toptica TA100). It can provide an output $\sim$ 600 mW at 780 nm wavelength, which is used for the MOT and polarization gradient cooling. The laser output is locked a few linewidths below the ^{87}Rb $F = 2$ to $F' = 3$ cycling transition using the polarization spectroscopy technique [110, 111]. For this purpose, a low intensity output (3 mW) from the rear panel of the Toptica TA100 is sent through an acousto-optic modulator AOM 1 (Isomet 1205C-2) in double-pass. This frequency-tuneable AOM is configured for a single-pass shift f_1 of 70 MHz, which makes a total 2×70 MHz frequency shift before entering the locking setup.

By utilizing a quarter-wave plate, we can obtain a circularly polarized pump beam which is sent to a Rb vapour cell. The Rb vapour cell is probed by a counter-

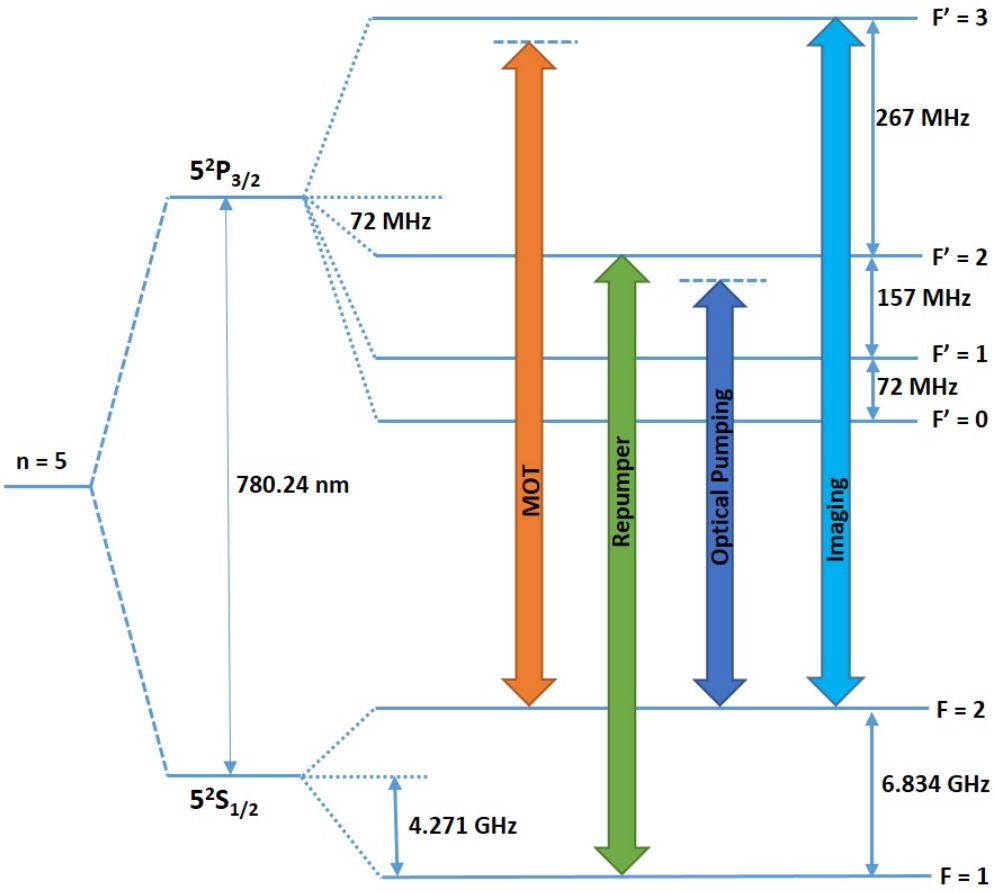

Figure 4.3: Energy level diagram of the ^{87}Rb D_2 line.

propagating linearly polarized beam. By detecting the difference of the polarizations of the probe beam without and with the vapour cell by means of a polarizing beam splitter, the laser can be locked to the $F = 2$ to $F' = 3$ cycling transition. Since the locking beam experiences a frequency up-conversion, the laser beam is red-detuned by $2 \times f_1$ from the $F = 2$ to $F' = 3$ cycling transition.

The main output of the TA100 diode laser is sent through AOM 2 (Isomet 1206C), which has a frequency shift of $f_2 = 125$ MHz. As a result, it produces a total detuning of $f_2 - 2 \times f_1$. The first-order diffracted beam from AOM 2, with an output of $\sim$90 mW is sent to the MOT setup via a polarization-maintaining optical fibre. In our locking setup, AOM 1 is used for laser detuning through a double-pass configuration while AOM 2 is used as a fast shutter for the trapping laser with a response time of less than 500 ns compared to 1 ms for the mechanical shutters.

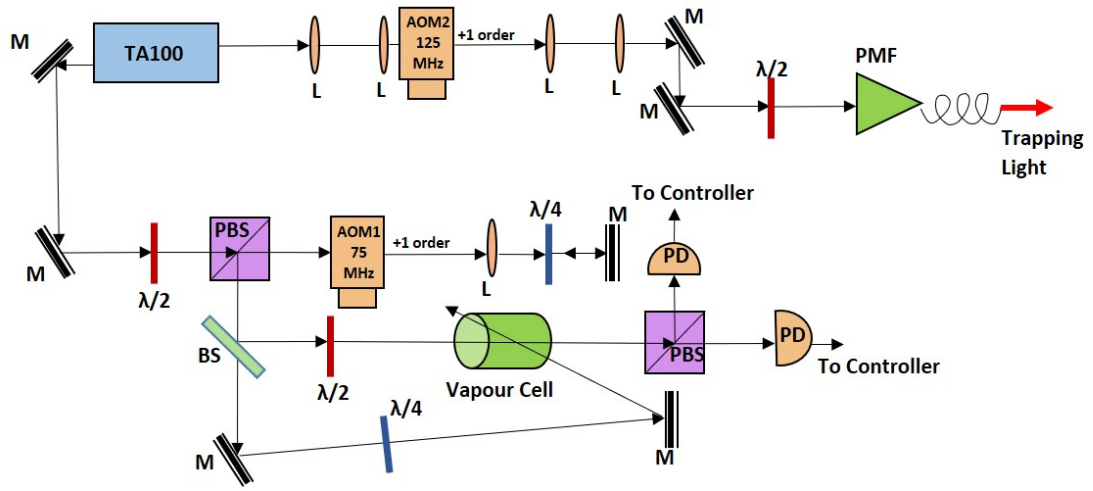

Figure 4.4: Optical layout for the trapping laser system. TA100: tapered amplifier diodelaser, PBS: polarizing beam splitter, AOM: acousto-optic modulator, $\lambda/4$: quarter-wave plate, $\lambda/2$: half-wave plate, PD: photo-diode, PMF: polarization-maintaining fibre, M: mirror, L: lens.

4.2.2 Repumper laser

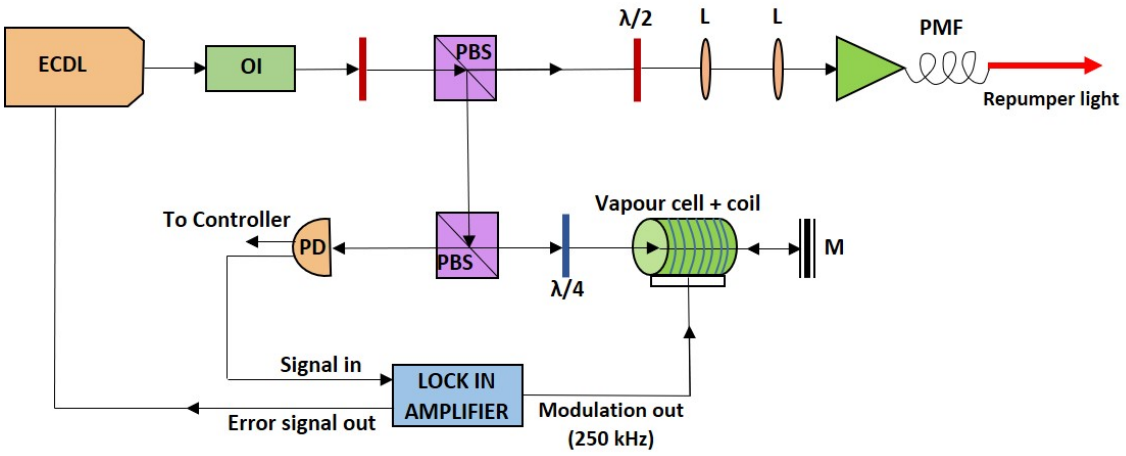

Figure 4.5: Optical layout for the repumper laser system. ECDL: external cavity diode laser, PBS: polarizing beam splitter, AOM: acousto-optic modulator, $\lambda/4$: quarter-wave plate, $\lambda/2$: half-wave plate, PD: photo-diode, PMF: polarization-maintaining fibre, M: mirror, L: lens, OI: optical isolator.

In our experiments, a 50 mW repumper laser, produced by a MOGLabs diode

laser (ECD-004) plus a MOGLabs diode laser controller, is locked to the $F = 1$ to $F' = 2$ transition using the Zeeman modulation technique. An error signal is generated by a lock-in amplifier, which is produced by subjecting a reference vapour cell to an AC magnetic field and modulating the laser frequency through the Doppler-free transition peak. The repumper beam is then sent to the MOT setup via a polarization-maintaining optical fibre producing a ~ 20 mW beam output. A schematic diagram of the repumper laser optics is shown in Figure 4.5.

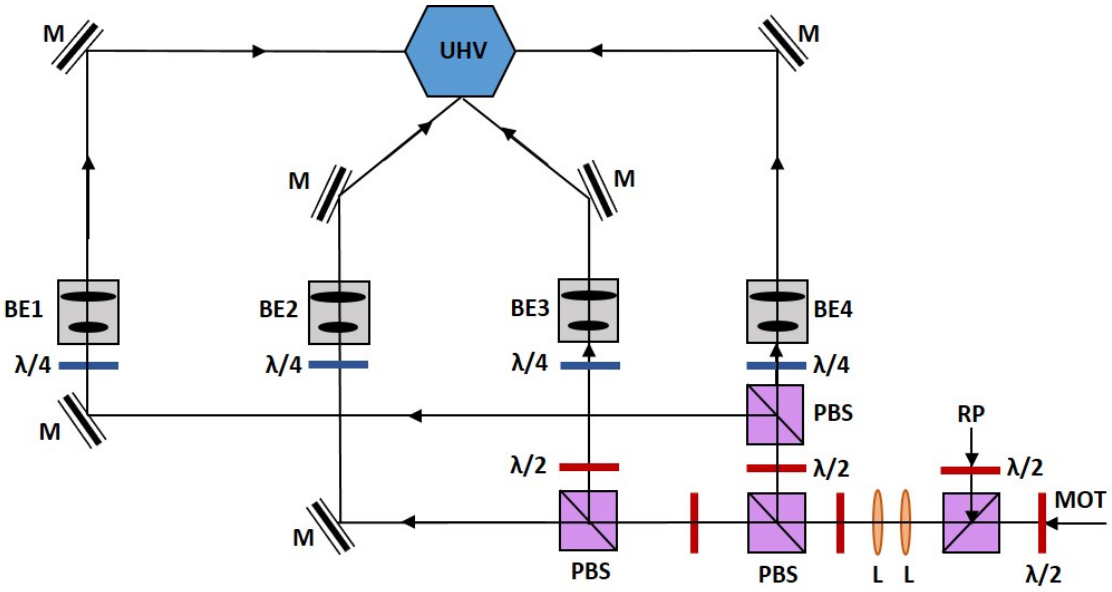

Figure 4.6: Schematic diagram of the MOT-beam layout. BE: beam expander, PBS: polarizing beam splitter, $\lambda/4$: quarter-wave plate, $\lambda/2$: half-wave plate, PMF: polarization-maintaining fibre, M: mirror, L: lens, RP: repumper light, MOT: trapping light.

During the MOT stage, some atoms may experience off-resonant excitation via the $F = 2 \rightarrow F' = 2$ transition to the $F' = 2$ state which decays to the $F = 1$ dark state and cannot be cooled. Therefore, in our MOT setup, after transferring through the polarization maintaining optical fibre to the UHV chamber optical table, the repumper beam is combined with the trapping beam for higher trapping efficiency. This combination beam, with an output of ~ 220 mW, is then further divided into four different beams using a polarizing beam splitter which are sent to the UHV

chamber with a power of around $\sim$ 40 mW after beam expansion up to $\sim$ 20 mm in diameter, as shown in Figure 4.6.

4.2.3 Optical pumping laser

In our experiment, in order to efficiently load trapped atoms into the magnetic lattice, we require a large number of atoms trapped in the $|F = 1, m_F = -1\rangle$ state. After the MOT stages, atoms are populated over all Zeeman sublevels. Therefore, an active optical pumping stage is needed to optically pump atoms into the desired state $|F = 1, m_F = -1\rangle$. This can be done by applying a combination of σ^- light and π-polarization light. The σ^- light is achieved by passing the beam through a $\lambda/4$ waveplate while π-polarization can be achieved by a small misalignment between the beam and its quantization axis. The σ^- light is employed to optically pump atoms into the $|F = 2, m_F = -2\rangle$ state while the π-polarization light pumps atoms from the $|F = 2, m_F = -2\rangle$ state into the required $|F = 1, m_F = -1\rangle$ state (Figure 4.7).

The optical pumping beam, taken from a MOGLabs diode laser with $\sim$ 40 mW laser output, is first sent through a PBS to extract a weak beam for the locking procedure. This weak beam is locked to the $F = 2 \rightarrow F' = 1/F = 2 \rightarrow F' = 3$ cross-over using a frequency modulation locking scheme, shown in Figure 4.8. As the atom cloud is thick for resonant light, in order to pump atoms in all undesired Zeeman sublevels the main beam is red-detuned by 20 MHz from the $F = 2 \rightarrow F' = 2$ transition by passing through an AOM (Isomet 1205C-2) operating at 75 MHz. This light is then coupled into a PMF which is later sent through a $\lambda/4$ waveplate to create the desired σ^- polarization, before reaching the UHV chamber with an output of $\sim$ 3 mW.

The reason we do not choose the passive pumping method, in which the repumper laser is shut off right after the PGC stage in order to let atoms relax to the $|F = 1, m_F = -1\rangle$ state, is that the active pumping method can achieve a higher (around two-fold) efficiency, compared to the passive optical pumping method.

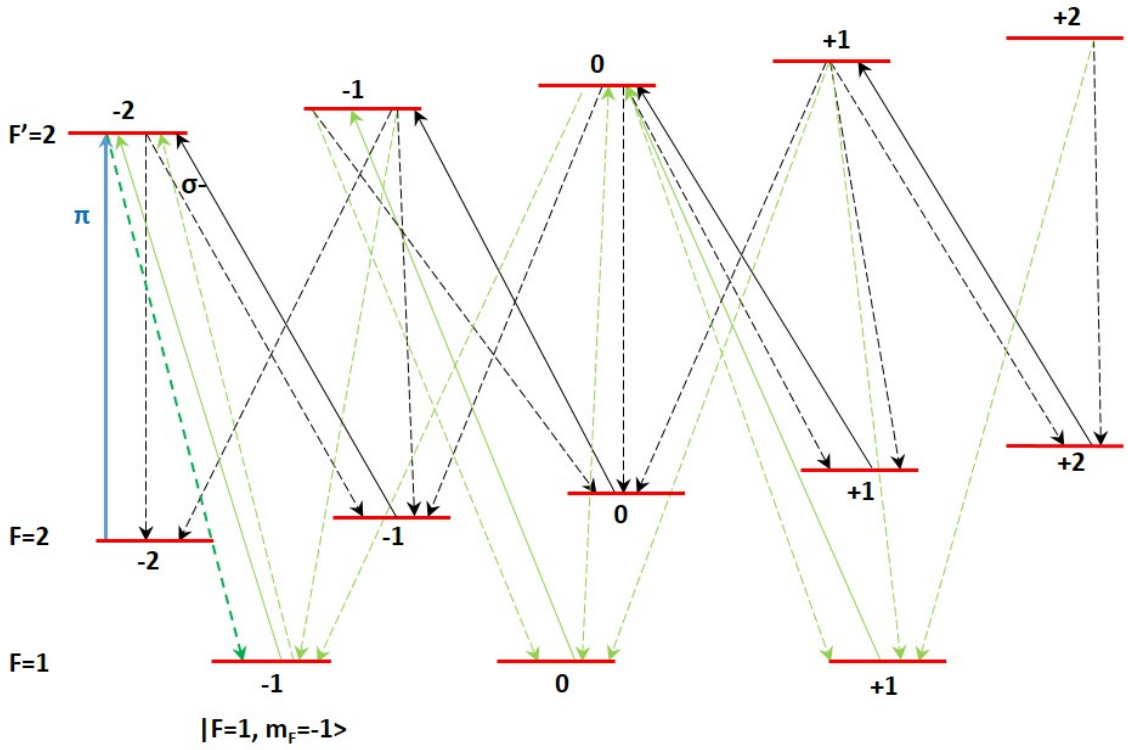

Figure 4.7: Optical pumping ^{87}Rb atoms into the $|F = 1, m_F = -1\rangle$ state. The dashed lines refer to spontaneous emission.

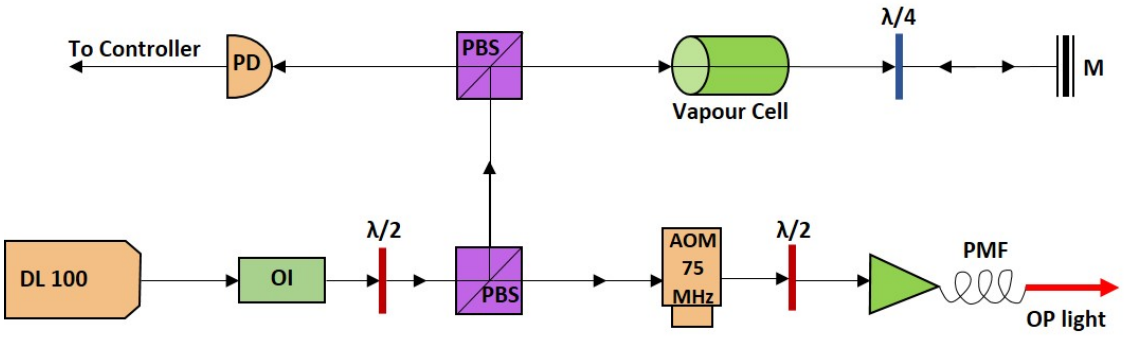

Figure 4.8: Optical layout for the optical pumping laser system. DL 100: Toptica external cavity diode laser, PBS: polarizing beam splitter, AOM: acousto-optic modulator, $\lambda/4$: quarter-wave plate, $\lambda/2$: half-wave plate, PD: photo-diode, PMF: polarization-maintaining fibre, M: mirror, L: lens, OI optical isolator.

4.2.4 Imaging laser

In our experiments, the imaging laser setup is quite a challenge since high precision measurements with low noise and low fringing are required. For this purpose, a

narrow linewidth ($\sim$ 80 kHz) imaging beam from a MOGLabs cateye external cavity diode laser (ECD-003) with an output of $\sim$ 40 mW is used. This beam is split into two parts by a PBS, where the weak beam is sent through an AC peak locking system for locking to the $F = 2 \rightarrow F' = 1/F = 2 \rightarrow F' = 3$ cross-over while the main beam is passed through a tuned AOM (Isomet 1206C). This AOM, operating at 105 MHz, tunes the imaging light to the $F = 2 \rightarrow F' = 3$ cycling transition with a double pass before coupling to a PMF. The light is then σ^--polarized by a $\lambda/4$ waveplate, which is aligned 45^0 to the optical axis before being sent to the UHV chamber. A schematic diagram of the imaging laser optics is shown in Figure 4.9.

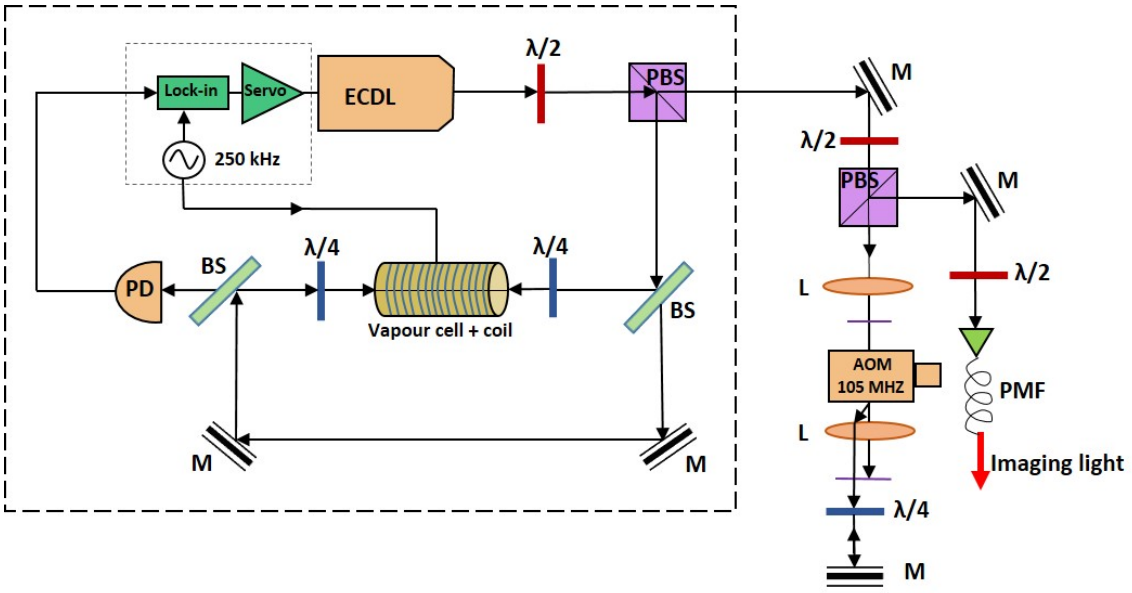

Figure 4.9: Optical layout of the imaging laser system. ECDL: external cavity diode laser, PBS: polarizing beam splitter, AOM: acousto-optic modulator, $\lambda/4$: quarter-wave plate, $\lambda/2$: half-wave plate, PD: photo-diode, PMF: polarization-maintaining fibre, M: mirror, L: lens, BS: beam splitter.

After the UHV chamber, an imaging system consisting of two lenses with focal lengths $f_1 = 120\,\text{mm}$ and $f_2 = 500\,\text{mm}$ is used for collecting images as shown in Figure 4.10. The first lens is positioned at a distance equal to its focal length $f_1 = 120\,\text{mm}$ from the chamber, while the second lens is positioned a distance equal to $f_2 = 500$ mm from the CCD camera. The distance between the two lenses is

determined based on the desired magnification $M = f_2/f_1$.

4.3 Absorption imaging

To image the magnetically trapped atoms, a resonant absorption imaging method is used, in which an imaging beam traverses the atom cloud in a direction parallel to the chip surface. In principle, this technique is based on detecting the difference of the light intensity of the imaging beam before and after traversing the atom cloud on a CCD camera. This method gives a two-dimensional profile of the atom cloud based on the light absorption by the atom cloud which casts a shadow on the CCD camera.

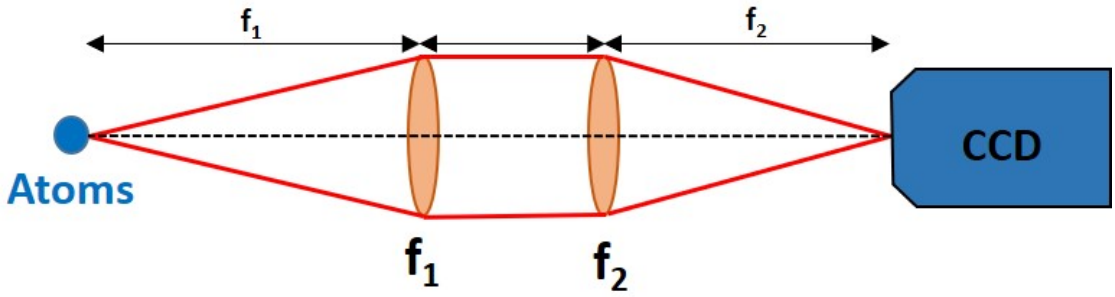

Figure 4.10: Optical setup for absorption imaging system. CCD: camera; f_1: lens with focal length f_1; f_2: lens with focal length f_2.

Assuming laser light of intensity I_0 passing through the cloud, the intensity distribution of the imaging light in the x-direction is given by:

$$I(y,z) = I_0(y,z)e^{-OD(y,z)}, \tag{4.1}$$

where $OD(y,z) = \sigma \int n(x,y,z)dx$ is the optical density and $n(x,y,z)$ is the cloud density. The photon absorption cross section σ for an atomic transition between the $|F = 2, m_F = +2\rangle$ and the $|F = 3, m_F = +3\rangle$ states is given by:

$$\sigma = \frac{\sigma_0}{1 + I/I_s + 4(\delta/\Gamma)^2}, \tag{4.2}$$

where I_s is the saturation intensity, Γ is the natural radiative linewidth, δ is the laser detuning and $\sigma_0 = \frac{3\lambda^2}{2\pi}$ is the resonant absorption cross section for a two-level system. In our experiment, σ^+ polarized imaging light is used for ^{87}Rb, which gives $\sigma_0 = 2.9 \times 10^{-13}\,\mathrm{m}^2$. The number density of an atom cloud is given by:

$$n(y,z) \equiv \int n(x,y,z)dx \approx \frac{OD(y,z)}{\sigma_0}. \tag{4.3}$$

For each absorption imaging cycle, three consecutive frames are taken, which are shown in Figure 4.11: a first CCD clean frame which is used for discharging all the accumulated dark counts, a second absorption frame with atoms and a third reference frame without atoms. The CCD clean frame is then discarded while the light intensities I_{abs} and I_{ref} are derived from the last two CCD images, respectively. The optical density is then rewritten as $OD = -\ln[I_{abs}/I_{ref}]$. Therefore, the total number of atoms can be calculated as:

$$N = \int_{A_p} n(y,z)dydz = \frac{A_p}{\sigma_0} \sum_{(i,j)\in A_p} OD_{ij}, \tag{4.4}$$

where A_p is the pixel area of the CCD camera.

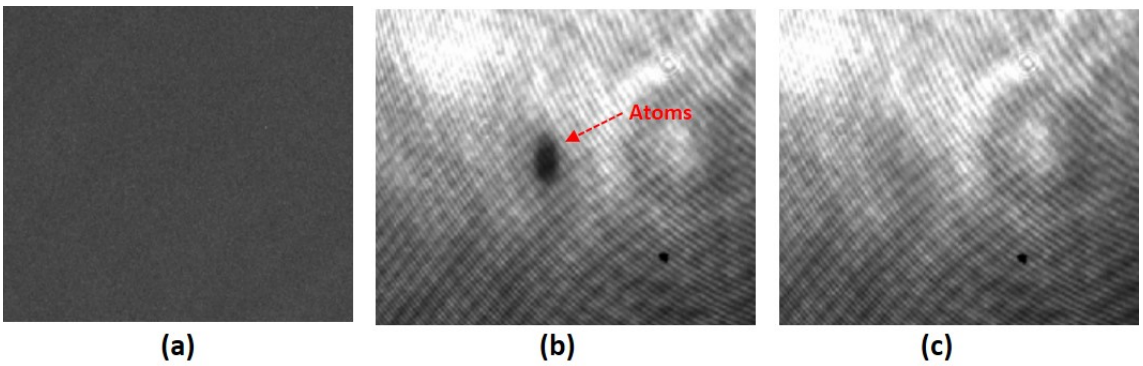

Figure 4.11: Frames taken by the CCD camera within one imaging cycle, (a) CCD clean frame, (b) absorption frame, (c) reference frame.

In our experiment setup, a Princeton Instruments frame transfer camera MicroMAX: 1024B is employed to capture images of the atoms. The camera has 1024×1024 pixels^2 with a pixel area of $13\,\mu\mathrm{m} \times 13\,\mu\mathrm{m}$. The quantum efficiency of the camera, which corresponds to the number of electrons that the camera produces when absorbing one photon, is $Q \approx 0.7$ for a laser wavelength of $\lambda = 780$ nm.

By using the camera in so-called frame-transfer mode, the time between taking two consecutive second and third frames is 4 ms while the exposure time of the camera is 1200 ms. Compared to the full-frame mode, the frame-transfer mode gives clearer images with less fringing and noise because the difference in beam intensity between the two frames caused by factors other than atom absorption are minimized in the very short time delay of 4 ms [60].

4.4 Computer control and electronics

In each cycle of our experiment, there are many complex stages which require a rapid change in numerous experimental parameters in differently defined steps with high accuracy. For this purpose, a LabVIEW programming environment (National Instruments LabVIEW) which controls and synchronizes experimental parameters is used. This program is run by a computer to generate both analog and digital signals using three National Instruments cards: one PCI-6259 card for digital output and two PCI-6713 cards for analog output. The first card controls the operation of the mechanical shutters, AOMs and other triggers while the other two cards control the current through the atom chip wires, magnetic coils and tuning of AOMs. For controlling the U-wire and Z-wire current through the atom chip and magnetic field coils, home-made IGBT switches are used with a typical response time of less than 800 μs. For operation of the CCD camera, a separate computer is used for image acquisition with the WinView program.

4.5 50 Hz AC line synchronization

For conducting high accuracy measurements with the magnetic lattice, it is required to reduce the effect of stray magnetic fields to a minimal level. There can be AC magnetic noise mainly from nearby power supplies affecting the experiments. The measured dominant noise is from 50 Hz and its higher harmonic frequencies. For example, during RF spectra measurements, the width of the measured RF spectra is

quite sensitive to this noise. The reason might be traced back to phase fluctuations of the 50 Hz AC line while we are applying the RF pulse in the RF spectra measurements. The fluctuations cause a phase difference in the RF pulse triggering which can alter the trap bottom and consequently lead to broadening of the RF spectra.

This problem can be simply overcome by building a line trigger circuit which ensures the RF pulse is triggered at a fixed specific phase compared to the AC noise. For this reason, we have employed a 50 Hz AC line trigger circuit which was designed by Rice University (Figure 4.12). Generally, the circuit acts as a good clock and produces TTL pulses which trigger the RF pulse generator at the zero-crossing of the AC power line. In this way, the RF pulse is locked to a well-defined phase of the AC line until being triggered by the circuit which consequently suppresses the magnetic noise from the environment.

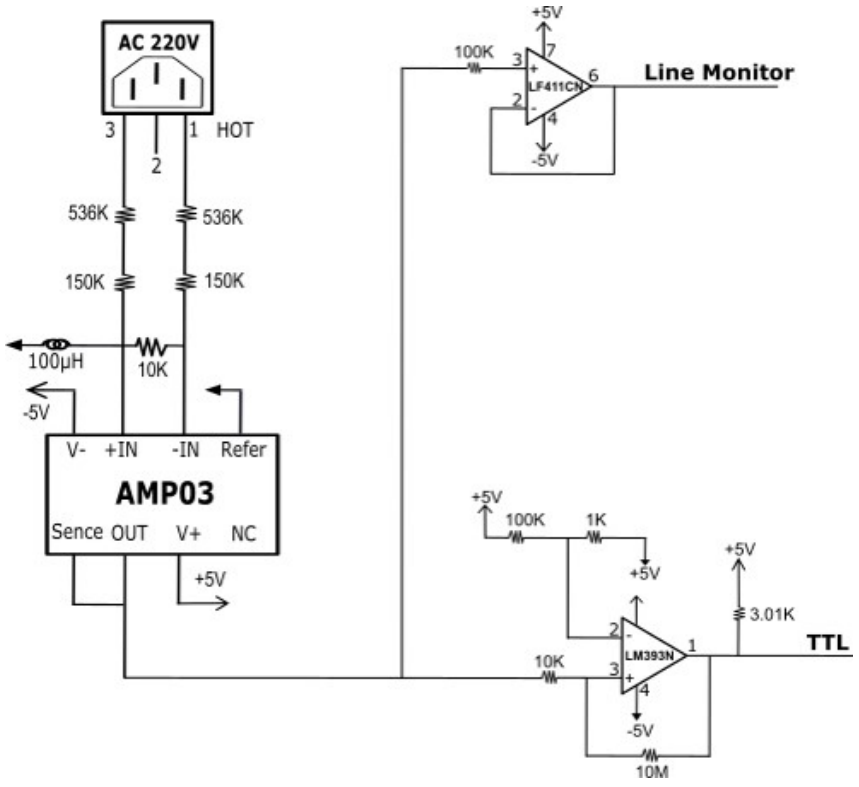

Figure 4.12: Schematic drawing of the 50 Hz AC line synchronization line circuit.

4.6 Producing a Bose-Einstein condensation on the atom chip

4.6.1 Mirror MOT

In our atom chip experiment setup, two reflected beams from the gold reflecting surface of the atom chip are employed to replace two of the six beams of a normal MOT. In this configuration, the reflecting surface on the chip creates two pairs of trapping laser beams at 45° to the chip surface together with a pair of counter-propagating beams parallel to the chip surface. A pair of anti-Helmholtz coils is positioned outside the UHV chamber with their axis along the direction of one of the 45° beams to produce a quadrupole magnetic field (Fig 4.1). Upon reflection from the chip surface, a circularly polarized beam will change its helicity so that the pair of beams resembles a standard MOT light-field configuration. The quadrupole field centre position can be overlapped with the intersection of the four laser beams by using three orthogonal pairs of current-carrying coils in a Helmholtz configuration which produces uniform magnetic fields. The advantage of the mirror MOT (MMOT) is that its geometry creates a MOT very close to the atom chip, which increases the trapping efficiency by directly collecting atoms near the chip surface and then transferring to the magnetic trap.

In our experiment, the first stage involves cooling and trapping ^{87}Rb atoms in the MMOT. The trapping laser is red-detuned 14 MHz below the $F = 2$ to $F' = 3$ hyperfine transition and is mixed with the repumping light which is locked to the $F = 1$ to $F' = 2$ transition. In the first step, Rb dispensers (SAES alkali metal dispensers) are turned on by passing a current of 6.0 A for 26 s to produce the Rb vapour needed for the experiment. The dispensers are then turned off during the subsequent steps and finally turned on again at the end of each experiment cycle. A small running current of 2.9 A is used to maintain the temperature of the dispensers which is warm enough for them to quickly heat up in the following experiment cycles. After the MMOT stage, approximately $2\times\ 10^8$ atoms are trapped at $\sim$ 1.2

mm below the chip surface.

4.6.2 Compressed U-wire magneto-optical trap

After the MMOT stage, the atoms are brought closer to the chip surface by transferring to a compressed U-wire magneto-optical trap (CMOT) in 30 ms. In the first step, the current in the external quadrupole coils is ramped down to zero to turn off the associated quadrupole magnetic field while the current through the U-wire is ramped up. Combining with a bias magnetic field in the x-direction, another quadrupole field with a larger field gradient along the z-direction is created. In the next step, the bias field is further ramped up while keeping the U-wire current constant to further compress the trap. After the CMOT stage, around $\sim 1.5 \times 10^8$ atoms at $\sim 150\ \mu K$ are transferred to the Z-wire trap. The main purpose of the CMOT is to increase the transfer efficiency of trapped atoms to the Z-wire trap with rapid magnetic field switching capability. However, a limitation of the CMOT stage is that as the density of the atom cloud is increased, the temperature of the atoms increases correspondingly which reduces the cloud density.

After the CMOT stage, a polarization gradient cooling (PGC) stage is used to further reduce the temperature of the atom cloud below the Doppler limit. During this stage, the trapping laser detuning is ramped up to 56 MHz in three stages while keeping the U-wire current the same. By doing this, the atom scattering rate decreases which results in a reduction of the radiation pressure and consequently an increase of the cloud density. After ~ 20 ms of PGC, the temperature of the cloud is as low as 30 μK. The U-wire current and trapping light are then turned off for the next stages.

4.6.3 Optical pumping

As only atoms in low field-seeking states can be trapped in a magnetic trap, it is required to prepare the atoms in the $|F = 1, m_F = -1\rangle$, $|F = 2, m_F = 1\rangle$ or $|F = 2, m_F = 2\rangle$ states. In our experiment, the $|F = 1, m_F = -1\rangle$ absolute ground

state is chosen because of its three-times smaller three-body recombination rate and weaker magnetic confinement compared with the $|F = 2, m_F = 2\rangle$ state [56,57]. For optical pumping atoms into the $|F = 1, m_F = -1\rangle$ state, an active optical pumping scheme is used. In the first 0.5 ms, atoms are transferred to the $|F = 2, m_F = -2\rangle$ state with a σ^--polarized light component of the optical pumping beam (Figure 4.7). During this period, the repumper light is also employed to optically pump atoms out of the $|F = 1, m_F = 0\rangle$ and $|F = 1, m_F = +1\rangle$ states. After this step, atoms occupy the negative magnetic sublevels $m_F = -1$ and $m_F = -2$. After switching off the repumper light, the optical pumping light with a π-polarization component is applied for an additional 0.5 ms to remove atoms from the $|F = 2, m_F = -2\rangle$ dark state so that they then relax into the $|F = 1, m_F = -1\rangle$ state through the $|F' = 2, m_F = -2\rangle$ excited state. The optical pumping light is then shut off for the loading of the Z-wire magnetic trap. In order to check the efficiency of the optical pumping stage, a comparison of the atom number trapped in the Z-wire magnetic trap after employing and not employing an optical pumping stage was performed. In our experimental system, the optical pumping stage atom number increases ~2.5 times the atom number previously trapped in the Z-wire magnetic trap.

Besides the active optical pumping scheme described above, there is a passive optical pumping method, which is to turn off the repumper laser after the PGC. By doing this, most of the atoms will spontaneously decay into the $|F = 1, m_F = -1\rangle$ state. However, the efficiency of this method is not as high as for the active pumping method.

4.6.4 Z-wire magnetic trap

After the optical pumping stage, atoms are transferred to the desired $|F = 1, m_F = -1\rangle$ trapping state which is ready for the Z-wire magnetic trap loading. The Z-wire trap has the advantages of rapid switching of the magnetic field and a high collision rate for efficient evaporative cooling which is needed to achieve BEC. In this stage, a Ioffe-Pritchard magnetic trap is created $\sim 600\ \mu m$ from the chip surface by applying a 35 A current through the Z-wire while the bias field B_x is increased to 33 G. To

control the trap depth and trap bottom, a bias field $B_y = 7.2$ G is applied. After that, atoms are transferred to the magnetic trap in 4 ms. In the next 100 ms, the trap is further compressed to increase the elastic collision rate and also to bring the atom cloud closer to the chip surface. This is done by ramping the Z-wire current to 37.6 A, B_x to 52 G and B_y to 8 G. In the ideal case, this compression is an adiabatic process which increases the elastic collision rate several orders while the phase space density remains constant. After this stage, around $5\times\ 10^7$ atoms are trapped in the Z-wire magnetic trap.

4.6.5 Forced evaporative cooling

Forced evaporation cooling is used to cool atoms in the Z-wire magnetic trap. This cooling method employs RF radiation to resonantly transfer trapped atoms to non-trappable magnetic sublevels which are lost from the trap. The more energetic atoms located at the top of the trap, which have a large Zeeman shift, are out-coupled from the trap through $\Delta m_F = \pm 1$ transitions first as the Zeeman shift of the magnetic sublevels is in resonance with the RF frequency: $g_F \mu_F B = \hbar \omega_{RF}$. These atoms take away more energy than their share of thermal energy which allows the remaining atoms to rethermalize and reach a new equilibrium state at a lower temperature by elastic collisions.

During the evaporative cooling procedure, the trapped atoms are characterized by a Boltzmann distribution that is truncated at the trap depth $\epsilon_t = \eta k_B T$, where η is a truncation parameter [112]. In forced evaporation cooling, the trap depth ϵ_t is lowered as the cooling progresses to maintain an evaporation cooling rate given by:

$$\frac{1}{\tau_{ev}} = -N \frac{\eta e^{-\eta}}{\tau_{el}\sqrt{2}}, \tag{4.5}$$

where the elastic collision rate $1/\tau_{el} = n_0 \sigma_{el} \bar{v}\sqrt{2}$, $\sigma_{el} = 8\pi a_s^2$ is the elastic collision cross section, and $\bar{v}\sqrt{2} = \sqrt{\frac{16 k_B T}{\pi M}}$ is the average relative velocity between two atoms.

For a high evaporative cooling efficiency $\alpha = \frac{\mathrm{d} \ln T}{\mathrm{d} \ln N}$, the RF ramping should be performed at a proper rate. If the RF ramping rate is too low, the atoms can suffer

losses from background gas collisions. On the other hand, if the RF ramping rate is too high, there is not enough time to allow atom rethermalization to occur, so that consequently atoms are removed from the trap without cooling. Additionally, to allow a large increase in the phase space density, the elastic collision rate should be maintained at a rate [113]:

$$\frac{d(\tau_{el}^{-1})/dt}{\tau_{el}^{-1}} = \frac{1}{\tau_{el}}\left(\frac{\alpha(\delta - 1/2) - 1}{\lambda} - \frac{1}{R}\right) > 0, \tag{4.6}$$

where $\alpha = \frac{\eta}{\delta+3/2} - 1$, $\lambda = \tau_{ev}/\tau_{el} = \frac{\sqrt{2}e^{\eta}}{\eta}$ for large η, $\delta = 3/2$ for a 3D harmonic trap and $R = \tau_{loss}/\tau_{el}$ is the number of elastic collisions per trapping time.

As no photon redistribution is involved, evaporative cooling typically helps to increase the phase space density of the atom cloud by several orders of magnitude, which makes it a crucial stage in achieving a BEC.

In our experiments, an unamplified 30 MHz synthesized function generator (Stanford Research Systems DS345) provides a RF field in sweep mode in which the trap depth is ramped down as the cooling progresses. The RF field is transferred through a thin RF wire on the atom chip as an antenna whose plane is perpendicular to the trapping axis. The start frequency, the final frequency, the ramping time and the RF amplitude parameters are programmed before each experimental cycle. The RF cooling period is 12 seconds with a starting frequency of 30 MHz and RF amplitude of 5 V while the final frequency is determined based on the desired final temperature of the atom cloud. This setting is considered to be optimal for cooling, in which the ramping rate is not too fast so that rethermalization of the atoms can occur, nor is it too slow for the limited trapping lifetime of atoms in the magnetic trap.

4.6.6 Trap frequency measurements

To measure the radial trapping frequencies of atoms in the Z-wire magnetic trap, we use a dipole oscillation method. The Z-wire trapped cloud is first cooled close to the BEC critical temperature to reduce the size during the evaporation cooling. In the next step, the cloud is shaken vertically in the z-direction by quickly changing

the Z-wire current for a short time of ~ 1.2 ms and then back to the original value while the bias fields remain unchanged. This introduces an oscillation in the vertical direction to the cloud. By recording the position of the cloud after different holding times t, we map the oscillation of the atoms in the trap in the z-direction. By fitting a sinusoidal function to the oscillation, one can determine the radial trapping frequency which is equal to the oscillation frequency. In this experiment, the value of the final current I_f and the current changing time determines the amplitude and the frequency of the oscillations. The value of I_f is chosen so that the cloud oscillation remains in the harmonic region near the bottom of the trap while the current changing time is chosen to be one-half of an oscillation period.

Figure 4.13 shows the measurement of the Z-wire trapping frequency for $I_z = 37.7\,\mathrm{A}$, $B_x = 52\,\mathrm{G}$, $B_y = 8.3\,\mathrm{G}$ by the dipole oscillation method. The measured radial trapping frequency is $\omega_{rad}/2\pi = 417(2)$ Hz. This measurement is in reasonable agreement with the calculated trapping frequency $\omega_{rad}/2\pi = 426$ Hz.

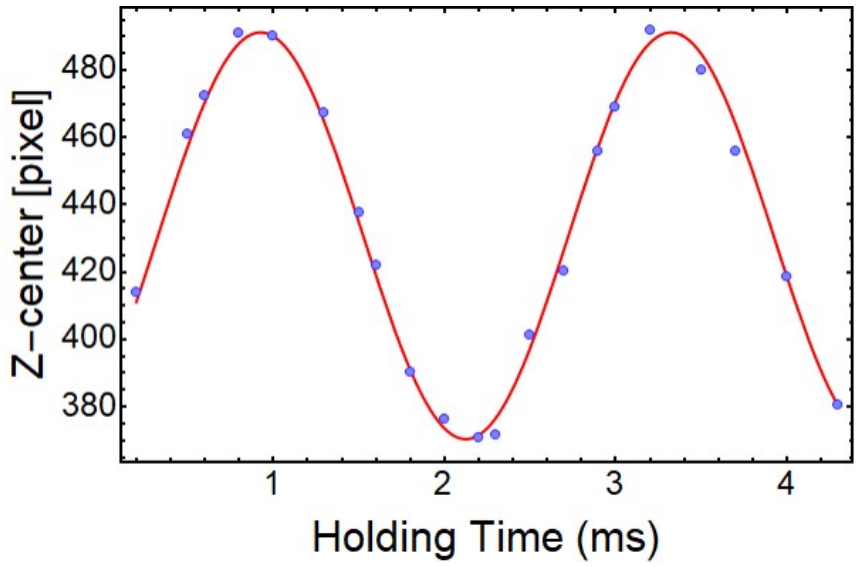

Figure 4.13: Radial trapping frequency measurement of the Z-wire magnetic trap, $\omega_{rad}/2\pi = 417(2)$ Hz.

For measurements of the small axial trapping frequency, it is very difficult in our experiment setup to use the above dipole oscillation method. Instead, the trapped atom cloud is shaken along the axial (y) direction and a collective mode excitation

method is employed [114]. The experiment procedure is described in detail in the thesis of Yibo Wang [61]. The measured axial trapping frequency is $\omega_{ax}/2\pi = 18(2)$ Hz.

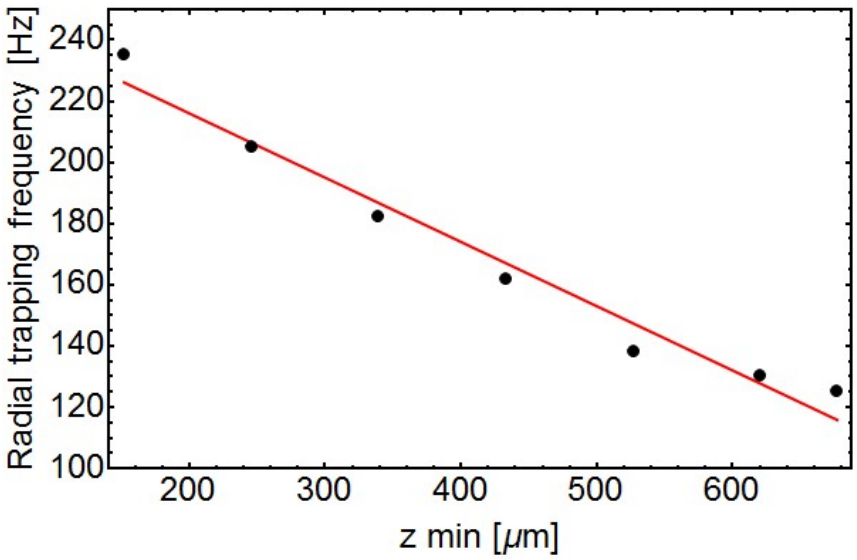

Figure 4.14: Radial trapping frequency versus distance to the chip surface. The linear fit is $\omega_{rad}/2\pi = -0.21 \times z_{min} + 257(7)$ Hz.

All of the measurements above were performed with the Z-wire magnetic trap located far ($\sim$ 700 μm) from the chip surface where there are no trap perturbation or surface effects much affecting the trapped atoms. However, as the Z-wire magnetic trap is brought to within $\sim 100\,\mu$m of the chip surface, atom-surface interactions significantly affect the trapped atoms. Any perturbation or oscillation of the trap can result in atoms hitting the chip surface and becoming lost. Additionally, atom-surface interactions, which can distort the trapping potential, may affect the accuracy of the measurements. Therefore, for distances $< 100\,\mu$m from the surface an extrapolation of the radial trapping frequency of the Z-wire magnetic trap is performed. The extrapolation is based on a series of radial trapping frequency measurements versus distance z_{min} as shown in Figure 4.14, which gives a linear fit $\omega_{rad}/2\pi = -0.21 \times z_{min} + 257(7)$ Hz. The change of the axial trapping frequency with distance is assumed to be negligible.

4.6.7 Effective pixel size

As the images taken by our CCD imaging system are processed by a Winview program, all dimensions and distances are measured in pixel units. Therefore, we need to have a parameter for converting pixel units to the real distance in our imaging system. This parameter is called the effective pixel size (EPS), which is also used to check the magnification of our imaging system. We use this mainly for measurements of the distance from the atom cloud to the chip surface. At first, the distance between the real and reflected images of the clouds (Figure 5.1 (b)) in pixels is measured. Then, this is converted to the real distance in μm. This distance is approximately twice the distance from the real atom cloud to the atom chip.

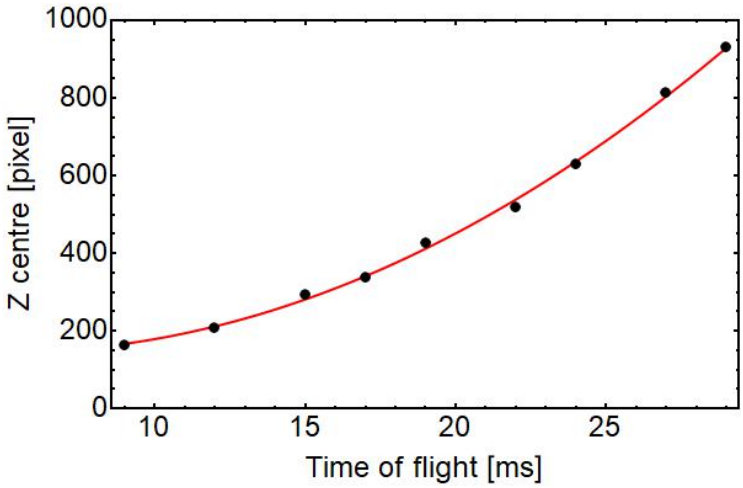

Figure 4.15: Effective pixel size measurement of the imaging system. The black points are experimental data, the red curve is the fit of a second-order polynomial function $z = 1.36t^2 - 13.7t + 179.4$. The unit of t is ms.

To determine the effective pixel size, a measurement of the vertical position of the atom cloud centre after different times of flight is performed. When the cloud falls under gravity, the vertical cloud position follows the kinematic equation $z = \frac{g}{2}t^2 + v_0 t + z_0$, where g is the gravitational acceleration. The pixel size is then determined by fitting the recorded data with a second-order polynomial $z = At^2 + Bt + C$. Thus, the effective pixel size can be calculated as $EPS = g/(2A)$.

A second-order polynomial function fit for the effective pixel size of our imaging system is shown in Figure 4.15. The fitting function $z = 1.36t^2 - 13.7t + 179.4$ gives the effective pixel size $EPS = 3.31\,\mu$m while the resolution of the imaging system is $\sim 10\,\mu$m.

4.6.8 Bose-Einstein condensation in the Z-wire trap

As the atom cloud is cooled by RF evaporative cooling to a final RF frequency of 580 kHz, besides the isotropic Gaussian distribution of the thermal cloud, an inverted parabolic shape of a BEC (Thomas-Fermi distribution) in a harmonic trap appears. The thermal and condensate components of this bimodel distribution are non-interacting. As the temperature is reduced further, the thermal component becomes less dominant while the distribution of the condensate part becomes sharper until an almost pure BEC distribution is achieved for a final RF frequency of 480 kHz. The evolution of the atom distribution in the cloud is shown in Figure 4.16.

Further evidence of a BEC is provided by the anisotropic expansion of the atom cloud in Time of Flight (TOF) measurements, as shown in Figure 4.17. In this experiment, the Z-wire current is switched off to release the cloud from the trap. As a result, the cloud falls downwards under gravity and an anisotropic expansion occurs in which the condensate component of the cloud experiences an accelerated expansion in the tight radial direction. The radial $R(t)_{rad}$ and axial width $R(t)_{ax}$ of the atom cloud after a TOF t are given by [115]:

$$R(t)_{rad} = R(0)_{rad}(1 + \omega_{rad}t) \tag{4.7}$$

$$R(t)_{ax} = R(0)_{ax}(1 + \frac{\pi\omega_{ax}^2}{2\omega_{rad}}t), \tag{4.8}$$

where $R(0)_{rad}$ and $R(0)_{ax}$ are the initial radial width and axial width of the cloud before releasing from the trap, and ω_{rad} and ω_{ax} are the radial and axial trapping frequencies, respectively.

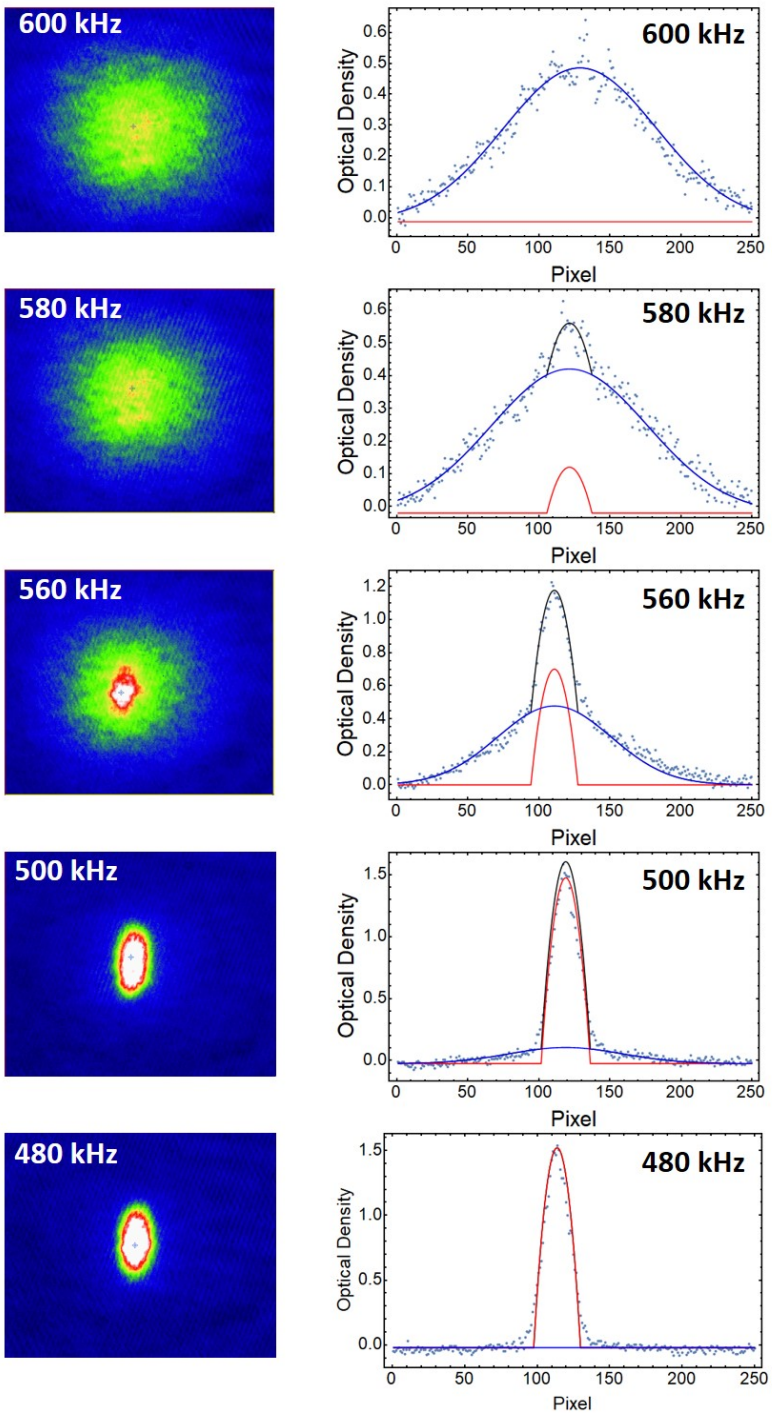

Figure 4.16: Evolution of the density distribution of atoms trapped in the Z-wire magnetic trap as the RF frequency is lowered during the evaporation cooling procedure. The left panel shows the Z-wire cloud images. The right panel shows the corresponding fitting of the cloud density distribution in the y-direction.

Compared to the expansion $R(t)_{rad}$, the $R(t)_{ax}$ is negligible as $\omega_{ax} \ll \omega_{rad}$ for the same TOF t. This anisotropic expansion occurs as the atom-atom interaction energy of the condensate is converted to kinetic energy (Figure 4.17). In the case of the thermal cloud, an isotropic expansion in both the axial and radial direction of the cloud is observed instead.

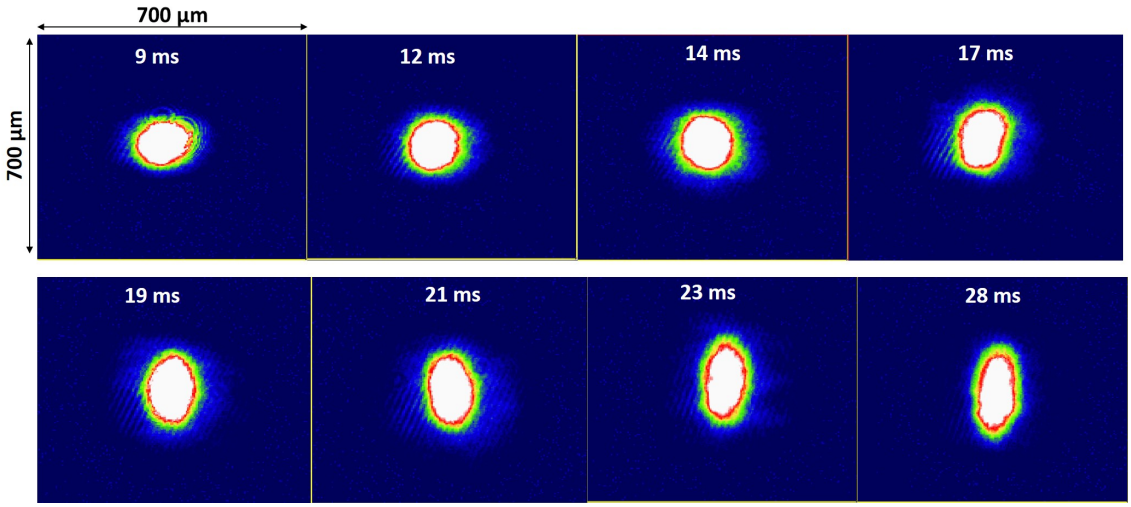

Figure 4.17: Anisotropic expansion of a BEC versus time of flight due to gravity after releasing from the Z-wire magnetic trap.

CHAPTER 5

Trapping atoms in the 0.7 μm-period triangular and square magnetic lattices

This chapter describes the successful trapping of ^{87}Rb atoms in multiple sites of the 0.7 μm-period triangular and square magnetic lattices at distances of less than 1 μm from the chip surface. Measurements of the lifetimes of the trapped atoms in both magnetic lattices are also presented. The experimental data presented in Figures 5.3 and 5.5 was obtained jointly with a former PhD student in our group, Yibo Wang [61].

5.1 Trap-surface distance calibration

In our experiment setup, the period of our 2D fabricated magnetic lattice structures are on a sub-micron scale, 0.7 μm. As the surface magnetic field from the magnetic structures decays exponentially from the film surface, the magnetic lattice traps are created at distances down to about $\sim$ 100 nm from the chip surface. This imposes a challenge for lattice loading experiments since at such a small distance, effects of atom-surface interactions can be significant which can induce atom losses. In order to load atoms into the magnetic lattice traps, one needs to merge the Z-wire magnetic trap with the lattice traps. Thus, before attempting to trap atoms in the

0.7 μm-period magnetic lattices at such small distances, it is important to study the surface-interaction effects on the Z-wire trapped atom cloud and to see how close the Z-wire trapped cloud can be to the chip surface without losing the atoms. This information helps us not only to determine the proper height to load atoms from the Z-wire trap into the magnetic lattice traps but also to study the effects of the surface on the Z-wire trapped atoms.

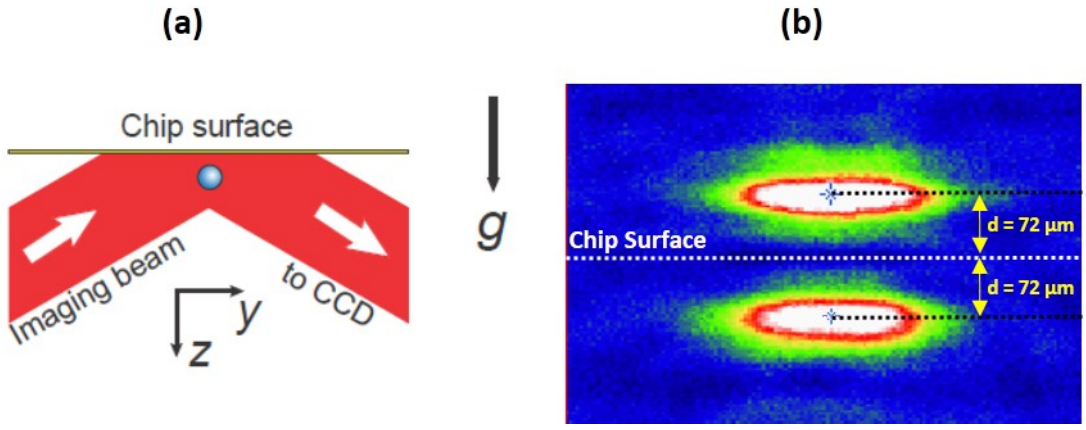

Figure 5.1: (a) Reflection absorption imaging setup, (b) reflection absorption images of a Z-wire trapped atom cloud at a distance of 72 μm from the surface showing the direct (lower) and mirror (upper) images of the cloud.

For this purpose, at first, a surface-distance calibration is performed to measure the distance from the Z-wire trapped atom cloud to the chip surface as the cloud is brought closer to the surface. These experiments are carried out by employing an *in situ* imaging method rather than releasing the cloud to fall under gravity and then taking standard TOF measurements. In this experiment, a reflection absorption imaging technique, in which the imaging beam is shone onto the reflecting chip surface at an angle of about 2°, is used [116]. The imaging beam is aligned so that the incoming beam and the reflected beam from the surface both pass through the cloud. This imaging setup produces a real image of the cloud together with its reflected image (Figure 5.1). The real image is created by the reflecting beam from the chip surface passing through the atom cloud while the reflected image is produced by the beam first passing through the atom cloud and then reflecting

from the chip surface. By measuring the distance s between the two images, the distance d from the centre of the magnetically trapped cloud to the chip surface can be determined from the expression $s = 2d\cos\theta$. When $\theta \approx 2°$, d is given to good approximation by $d = s/2$.

The experiment cycle begins by ramping down the Z-wire current I_z, while keeping the bias field B_{bx} at different selected values, and measuring the distance from the centre of the Z-wire trapped cloud to the chip surface. From a Gaussian fit to the cloud image, the vertical positions of the centres of the clouds in pixels are determined which are subsequently used to determine the distance d in μm using the measured effective pixel size (Section 4.6.7). In our experiment setup, owing to the finite resolution of the imaging system ($\sim$ 10 μm) and the large size of the atom cloud, as the atom cloud approaches very close ($\sim$ 40 μm) to the chip surface the two images merge into one and it is not possible to directly measure the distance. Therefore, an extrapolation of the linear curve of I_z versus distance, shown in Figure 5.2, is used to determine the distance of the cloud within 40 μm of the chip surface.

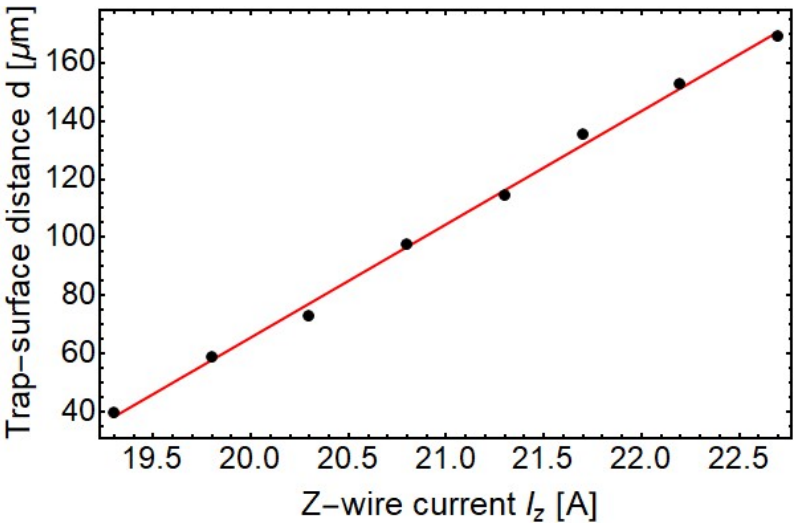

Figure 5.2: Distance calibration of a Z-wire trapped atom cloud close to the chip surface for B_x = 52 G. The measurement shows a plot of the distance d from the trap centre to the gold reflecting layer on the chip surface versus Z-wire current I_z. The fitting function is $d = 38.88(0.8)I_z - 712(17)$ μm.

As can be seen in Figure 5.2, there is a linear relationship between the current I_z passing through the Z-wire on the atom chip and the corresponding distance d from the cloud to the chip surface: $d = 38.88(0.8)I_z - 712(17)\,\mu$m, where the uncertainties are statistical (1σ). At $I_z = 0$, $d = 712(17)\,\mu$m which is consistent with the estimated distance from the plane of the current-carrying wires to the gold reflecting surface.

5.2 Projection of ultracold atoms towards the 2D magnetic lattice potential

Although during the baking procedure the heating temperature (~ 110°C) is kept well below the nominal Curie temperature ($300 - 400$°C) to protect the magnetic properties of the magnetic film, it is important before commencing the magnetic lattice trapping experiments to check the magnetization of the film *in situ* to ensure the ultracold atoms can interact with the short-range magnetic lattice potential. This is performed by bringing a Z-wire trapped atom cloud far from the surface ($d \sim 700\,\mu$m) to within a few hundred nanometres of the chip surface with no bias magnetic field applied. At such short distances, the cloud interacts with the short-range magnetic lattice potential in which the strength of the magnetic field decays exponentially from the surface with decay length $\sim 0.7\,\mu\text{m}/2\pi$.

In our earlier 1D 10 μm-period magnetic lattice experiments, an arc-shaped atom cloud reflection from the lattice grating structure was observed when a Z-wire trap cloud was projected towards the surface in the z-direction with a bias-field applied in the y-direction [54, 58]. This reflected cloud showed a lateral expansion in the y-direction with increasing TOF which resulted from the corrugated potential in the y-direction in the presence of the bias field B_y. For the case where there is no bias field applied, the reflected cloud from the 1D grating structure experiences no force component in the y-direction.

We have calculated the pseudo-potentials of the magnetic patterns in the trapping plane 0.35 μm from the surface created by the 0.7 μm-period square and triangular lattice structures for the case of no applied bias field. When an ultracold atom cloud interacts with the surface potentials, the cloud can only be reflected and atoms cannot be trapped since without a bias field there are no trap minima resulting from magnetic field cancellation. For the case of the square magnetic lattice, the magnetic pattern consists of a two-dimensional corrugated potential with a period $\sqrt{2}a$ [61]. For the case of the triangular magnetic lattice, the pattern consists of a corrugated potential with a period $\sim a$ in the y-direction and $\sim a/2$ in the x-direction [61]. The simulations were repeated for different trapping heights which showed robust potential patterns.

For our 2D 0.7 μm-period magnetic lattice structures, we expect the reflected cloud to show a lateral expansion in both the x-direction and the y-direction of the chip surface plane. As an atom approaches the surface, it experiences an exponentially increasing repulsive force in the z-direction which originates from the corrugated potential. In the case where there is no external bias field, the reflected cloud from the 1D structure experiences no force component in the y-direction while the reflected cloud from the 2D structure still experiences force components in the $x-$ and y-directions. Consequently, the force components in the x and y-directions affect the shape of the reflected cloud in the corresponding directions. In our imaging setup, since the imaging beam is aligned along the x-direction, only a half-moon shaped expansion of the cloud is expected.

For this experiment, at first a Z-wire trapped atom cloud at $\sim 200\,\mu$K is prepared at $\sim 700\,\mu$m from the chip surface. The cloud is then brought to a distance d close to the surface of the triangular magnetic lattice structure by slowly reducing I_z while keeping B_x constant. In the next step, we quickly turn off I_z and B_x simultaneously, so that I_z quickly becomes zero while the magnetic field B_x decreases much more slowly due to the slow response time ($\sim 10\,$ms) of the large Helmholtz coils. This introduces a momentum kick launching the cloud vertically towards the surface with an estimated initial launching velocity $v_l \sim 70\,\mu$m/ms. The experiment is repeated

for different cloud launching positions and the cloud behaviour is monitored after different TOFs, as shown in Figure 5.3.

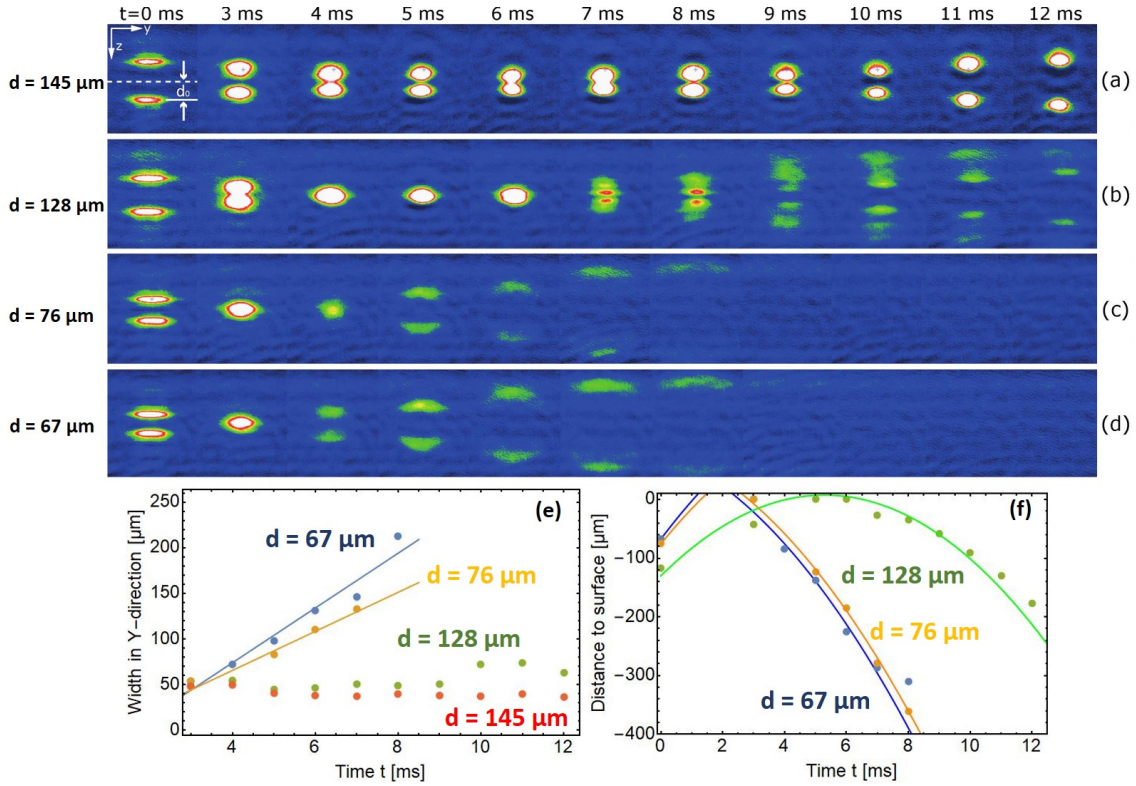

Figure 5.3: Reflection absorption images of an atom cloud launched vertically towards the magnetic lattice potential of the 0.7 μm-period triangular magnetic lattice structure with no bias field at distances d_0 = (a) 145 μm, (b) 128 μm, (c) 76 μm, (d) 67 μm from the chip surface. The upper clouds in (a) - (d) are the mirror images, the lower clouds are real images of the projected cloud. (e) Time evolution of the lateral widths along the y-direction and (f) vertical positions of the cloud launched vertically towards the magnetic lattice potential at distances d_0 = 67 μm (blue points), 76 μm (orange points), 128 μm (green points), 145 μm (red points). The fitted curves in (f) are $d = -67.5 + 70t - 0.5gt^2$ before reflection and $d = -82.5 + 60(t + 8.1) - 0.5g(t + 8.1)^2$ after reflection (blue line); $d = -75.7 + 65t - 0.5gt^2$ before reflection and $d = -82.5 + 60(t + 7.8) - 0.5g(t + 7.8)^2$ after reflection (orange); $d = -130 + 52t - 0.5gt^2$ (green). d is in μm and t is in ms. Gravity acceleration $g = 9.8\,\mu\text{m/ms}^2$. Adapted from [35].

As can be seen in Figure 5.3, when launched far from the surface, $d_0 > 128\,\mu$m, the cloud does not reach the magnetic potential before falling down under gravity. In this case, there is almost no thermal expansion observed during the free fall of the cloud; the lateral width remains constant $\sigma_Y \sim 50\,\mu$m since the cloud temperature is well below the critical temperature. When launched from a distance $d_0 = 128\,\mu$m, some of the cloud can reach the surface potential and is reflected. The cloud is split into two parts: the reflected part (the lower cloud) which expands in a direction parallel to the surface and the non-expanding free-falling part (the upper cloud). When the cloud is launched from smaller distances, $d_0 = 76\,\mu$m and $d_0 = 67\,\mu$m, a clear half-moon shaped expansion in the y-direction, which is associated with lateral expansion of the reflected cloud with TOFs in a direction parallel to the surface, is clearly observed.

To study the reflection dynamics, a simple analysis of the lateral width σ_Y and the initial launching distance d versus time t after projection is employed, as can be seen in Figure 5.3 (e), (f). For the case of no reflection, there is no change of the lateral width of the atom cloud ($\sigma_Y \sim 50\,\mu$m). The velocity of the cloud is fitted using a single quadratic function. After reflection from the chip surface, the lateral width of the projected cloud σ_Y increases almost linearly with TOF. The lateral width expansion with increasing fall time increases with velocities of $30\,\mu$m/ms for $d_0 = 67\,\mu$m and $21\,\mu$m/ms for $d_0 = 76\,\mu$m. By using quadratic functions, reasonable fitting of the cloud trajectories in the vertical direction is achieved. The fits imply the incident velocity v_i and the reflected velocity v_r of the cloud are not exactly the same. The fitting gives $v_i = 65\,\mu$m/ms, $v_r = 60\,\mu$m/ms for $d_0 = 76\,\mu$m and $v_i = 70\,\mu$m/ms, $v_r = 60\,\mu$m/ms for $d_0 = 67\,\mu$m, respectively. The fitted equations, given in the caption of Figure 5.3, indicate that for $d = 128\,\mu$m, the cloud reaches its turning point 8 μm below the silica surface after 5.3 ms. For $d = 76\,\mu$m and $67\,\mu$m, the projected cloud reaches the chip surface with incident velocities of 60 and 52 μm/ms after 1.0 and 1.3 ms launching, respectively and is reflected with downward velocities of 45 and 45 μm/ms, respectively. In fact, the initial launching position of the cloud plays an important role in determining the strength of the interaction with

the exponentially increasing magnetic potential. As the distance d_0 increases, the interaction decreases due to the decrease in the incident velocity at the surface; a cloud with low incident velocity penetrates the magnetic potential less than a cloud with high incident velocity. Consequently, the distance d_0 changes the spatial profile of the reflected cloud due to the different interaction strength with the corrugated potential. It is observed that the cloud reflection starts to occur at $d_0 \approx 128\,\mu$m. If we further reduce d_0 such that $v_i \gg 70\,\mu$m/ms the cloud would penetrate the potential, then hit the hot chip surface and become lost. Similar observations have been reported for the 1D 10 μm-period magnetic lattice by Singh *et al.* [54, 58].

An experiment was also performed in which the same atom cloud is launched vertically towards the surface in a region where there is no magnetic lattice structure. Similar to the experiment above, no reflection is observed as the cloud is launched far from the surface, $d_0 > 128\,\mu$m. For $d_0 \leq 128\,\mu$m, the cloud touches the surface and disappears immediately. This confirms that the magnetic potential from the lattice structures is responsible for the observed reflected cloud in Figure 5.3.

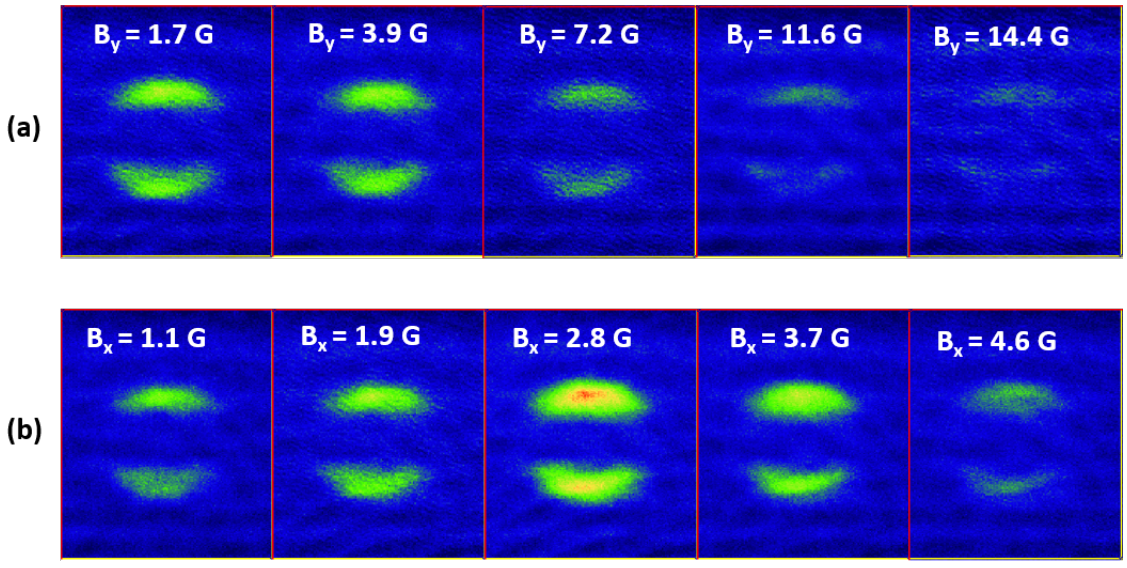

Figure 5.4: Reflection absorption images of an atom cloud launched vertically toward the triangular magnetic lattice potential at the same distance d_0 from the chip surface in different bias fields (a) B_y with $B_x = 0$ and (b) B_x with $B_y = 0$.

A similar experiment was performed on the triangular magnetic lattice structure

with a bias field applied in the x or y-directions. At appropriate initial launching distances d_0, the reflection of the cloud is observed with different strength for different bias fields, as can be seen in Figure 5.4. In the case of applying only a bias field B_y, the reflection becomes weaker as we increase B_y. This is attributed to the fact that for the triangular magnetic lattice structures, the applied bias field B_y is in the opposite direction to the direction of the magnetic field from the magnetic lattice structure, which reduces the repulsive force component in the y-direction. In the case of applying only a bias field B_x, the interaction becomes stronger until a certain value $B_x = 2.8\,\mathrm{G}$ and then gets smaller and disappears for $B_x > 4.6\,\mathrm{G}$. The non-uniform distribution of atom density in the reflected cloud is due to the fact that the magnetic interaction strength is not the same for all atoms, which is attributed to the different atom positions and momenta. From this experiment, it is clear that we can control the interaction strength between the Z-wire trapped atom cloud and the magnetic lattices and also the number of atoms interacting with the lattice potentials by varying the external bias fields.

5.3 Atom number versus Z-wire trap distance

To study the atom-surface interactions, measurements of the remaining atom fraction $\chi(d)$ versus distance $d = z - 75\,\mathrm{nm}$ from the chip surface were performed, where z is the distance of the centre of the atom cloud to the magnetic film and the 75 nm accounts for the nominal thickness of the gold and silica films on the chip surface. At first, a Z-wire trap cloud with an initial atom number N_i is prepared at a distance $d_i \sim 100\ \mu\mathrm{m}$ from the chip surface. By slowly ramping down the Z-wire current, the atom cloud is brought to a distance d close to the chip surface. The cloud is held there for a short time, $t_0 = 10\,\mathrm{ms}$, before being moved back quickly to its original position by ramping up the Z-wire current to the original value. The remaining number of atoms, N_f, is then measured using the *in situ* reflection absorption imaging method. During the whole experiment, the bias field B_x is kept constant.

The experiment is performed for a range of different atom cloud temperatures, which is achieved by changing the final evaporation frequency during the RF evaporative cooling stage: from a condensate $T = 200\,\text{nK}$ well below the critical temperature ($T_c \approx 520\,\text{nK}$) to thermal clouds at 600 nK, 1 μK and 2 μK. These temperatures were measured by TOF measurements where a Gaussian distribution was used to fit the measured cloud distribution. The measured atom fraction $\chi(d)$ versus distance d results are shown in Figure 5.5 for a range of different cloud temperatures.

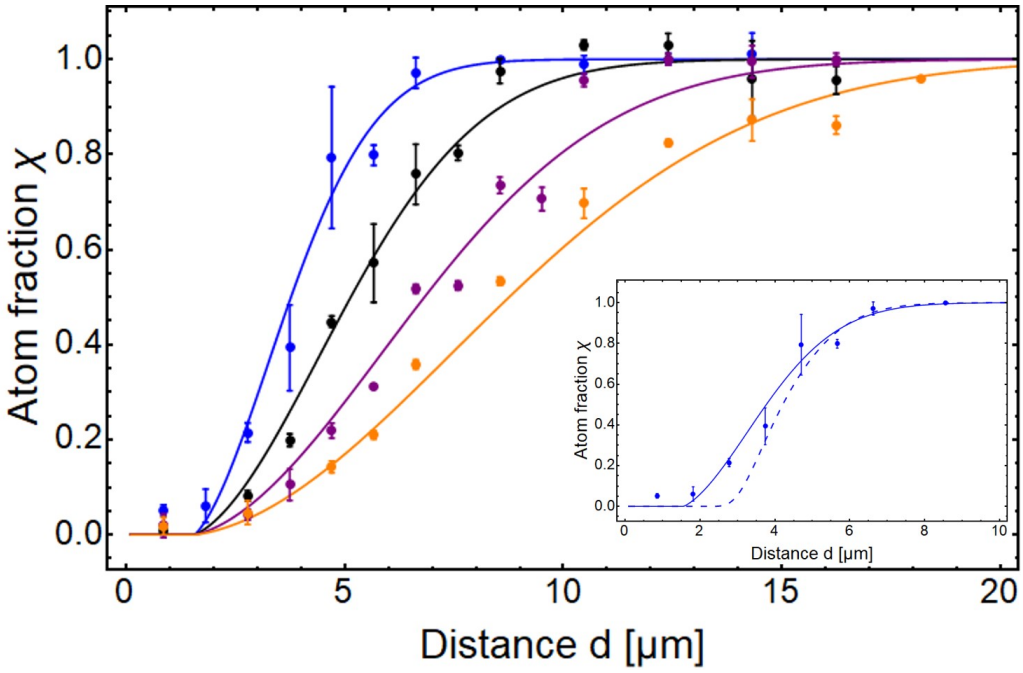

Figure 5.5: Remaining atom fraction $\chi(d)$ versus distance d of the Z-wire trap cloud centre from the chip surface for a BEC at $T \approx 200\,\text{nK}$ (blue) and for a thermal cloud at 600 nK (black), 1 μK (purple) and 2 μK (orange) for $B_x = 52\,\text{G}$. Solid curves are theoretical fits using the simple truncation model with $T \approx 190\,\text{nK}$ (blue curve), 430 nK (black curve), 0.85 μK (purple curve) and 1.5 μK (orange curve). The inset is the $\chi(d)$ versus distance d of the Z-wire trap cloud centre from the chip surface for a BEC at $T \approx 200\,\text{nK}$, where the dashed blue curve is a theoretical fit using the 1D surface evaporation model with $T = 130\,\text{nK}$, $\tau_{el} = 0.6\,\text{ms}$ (see text).

As can be seen in Figure 5.5, atom losses occur as the centre of the Z-wire trap cloud is brought close to the surface. For the condensate, the loss is noticed at

distances $d \sim 5\,\mu$m while the loss begins at distances $d \sim 10, 15, 20\,\mu$m for thermal clouds at $T \sim 0.6, 1, 2\,\mu$K, respectively. The rapid loss of atoms in the loose Z-wire trap at these distances is attributed to atom-surface interactions which could be caused by Johnson noise and/or Casimir-Polder interactions and/or inelastic collisions.

In our experiment setup, atom losses caused by 3-body recombination are ignored because of the long calculated lifetime, $\tau_{3b} = 500\,$s for a Z-wire trapped atom cloud at $T = 1.5\,\mu$K with $n = 6.7 \times 10^{12}\,\text{cm}^{-3}$, $N \sim 4 \times 10^5$ and $\omega_{rad}/2\pi = 300\,$Hz, $\omega_{ax}/2\pi = 18\,$Hz. In another experiment [61], a distance-independent loss rate for $d \gg 30\,\mu$m was observed which indicates an atom loss due to background collisions $\gamma_{bg} = (25 \pm 4\,\text{s})^{-1}$. Therefore, loss due to background collisions is negligible in these experiments.

In the case of atom losses due to Johnson noise, when atoms are trapped close to the surface, their magnetic moment couples to the fluctuating magnetic field from the thermal current noise in the gold conducting film near the chip surface. The coupling can drive spin-flip transitions which cause atom losses. In our experiment setup, the thickness of the gold reflecting layer is $t_{Au} = 50\,$nm and the trap bottom is set to 1.0 G, which gives a skin depth $\delta \sim 94\,\mu$m. As our experiments are performed in the region $\delta = 94\,\text{nm} \gg \max\{d, t_{Au}\}$, the spin-flip rate is calculated from Eq. 2.30, to give $\gamma_s = 1/\tau_s = (150\,\text{s})^{-1}$. The spin-flip lifetime due to Johnson noise is long and thus is not considered to be the significant factor for the steep atom loss curves in Figure 5.5.

When close to the surface, an atom cloud experiences a combined trapping potential $V(z) = V_z(z) + V_{CP}(d)$, where $V_z(z) = \frac{1}{2}M\omega_r^2(z - z_{min})^2$ is the harmonic Z-wire trap potential truncated at the chip surface $z = t_{Au} + t_{SiO_2} = 75\,$nm and $V_{CP}(d) = -\frac{C_4}{d^3(d+3\lambda_{opt}/2\pi^2)}$ is the attractive Casimir-Polder potential, where for ^{87}Rb $\lambda_{opt}/2\pi \approx 120$ nm and $C_4 \approx 8.2 \times 10^{-56}\,\text{Jm}^4$ for a dielectric silica film. For the attractive Casimir-Polder effect, the trap depth is lowered to ΔE_b corresponding to distance d, which is approximately reduced to zero at $d \approx 1\,\mu$m from the surface for a Z-wire trapped atom cloud at a radial trapping frequency $\omega_{rad}/2\pi = 280\,$Hz. The

$\omega_{rad}/2\pi = 280\,\text{Hz}$ is an extrapolated value based on the trapping frequency versus distance d curve (Figure 4.14). The finite trap depth created by the combined potential $V(z)$ leads to a sudden truncation of the high energy tail of the Boltzmann distribution of atoms in the Z-wire trap. Thus, the remaining atom fraction can be expressed approximately by a simple truncation model $\chi(d) = 1 - e^{-\eta}$, where $\eta = \Delta E_b/(k_B T)$ is the truncation parameter [86].

Trapped atoms with higher energies, located in the region near the chip surface, tend to escape the trap through 1D surface evaporation during the holding time $t_0 = 10$ ms. This is understandable since for a thermal cloud at temperature $T = 2\,\mu\text{K}$, the holding time is much longer than the elastic collision time $\tau_{el} \approx 1.6\,\text{ms}$. The simple truncation model above can be extended to include classical 1D surface evaporation loss of the atoms [87], in which the remaining atom fraction becomes $\chi = \chi_0 e^{-\Gamma_{ev} t_0}$, where $\chi_0 = 1 - \exp(-\eta)$ and $\Gamma_{ev} = f(\eta) e^{-\eta}/\tau_{el}$ is the atom loss rate due to 1D surface evaporation, $f(\eta) \approx 2^{-5/2}(1 - \eta^{-1} + \frac{3}{2}\eta^{-2})$ for $\eta \geq 4$ [117], $\tau_{el} = [n_0 \sigma_{el} \overline{v}_{rel}]^{-1}$ is the elastic collision time, $\overline{v}_{rel} = \sqrt{16 k_B T/(\pi M)}$ is the mean relative velocity, $n_0 = \frac{N}{(2\pi)^{3/2}\sigma_{rad}^2 \sigma_{ax}}$ is the peak atom density in the Z-wire trap, $\sigma_{rad,ax} = (k_B T/M)^{1/2}/\omega_{rad,ax}$ is the half-width of the trapped cloud, N is the number of atoms in the Z-wire trap, $\sigma_{el} = 8\pi a_s^2$ is the elastic collision cross section, and $a_s = 5.3\,\text{nm}$ is the s-wave scattering length for $^{87}\text{Rb}\ |F = 1, m_F = -1\rangle$ atoms.

For this 1D surface evaporation model, the cloud temperature T acts as the main fitting parameter. The fitting temperatures used for the data shown in Figure 5.5 are 190 nK, 430 nK, 0.85 μK and 1.5 μK, corresponding to the blue, black, purple and orange curves, respectively. These values are comparable to the temperatures measured by TOF mentioned above. For a good fit to the condensate 200 nK data set, a cloud temperature $T = 130\,\text{nK}$ and an elastic collision time $\tau_{el} = 0.6\,\text{ms}$ are employed, which is shown by the dashed blue curve in the inset of Figure 5.5. Compared to the fit using the simple truncation model, which is shown as the solid blue curve, there is a discrepancy for $\chi < 0.4$. The reason could be that for the simple 1D surface evaporation model, the effect of evaporation-induced temperature changes and redistribution of atom directions from the atom collisions are ignored

[118]. According to our simulations, the attractive Casimir-Polder force tends to reduce the trap depth of the combined potential $V(z)$ to zero at $d \sim 1.5\,\mu$m which is comparable to our observed value (Figure 5.5). Indeed, one can cool a trapped cloud by bringing it close to the chip surface thanks to surface-induced 1D evaporation. This method has been considered as an effective cooling method to reach BEC [92].

5.4 Trapping ^{87}Rb atoms in the 0.7 μm-period triangular magnetic lattice

From the experiments described above, it is clear that the magnetized magnetic film is suitable for lattice loading experiments and also that the Z-wire trapped atoms can be brought to a sufficiently close distance to smoothly merge with the magnetic lattice traps. To prevent significant atom losses due to the Casimir-Polder interaction for a Z-wire trap at distances $d < 1\,\mu$m from the chip surface, it is required to create a trap with very high trapping frequencies. Our simulations indicate that the trapping frequencies of our magnetic lattice traps (∼100-800 kHz) are sufficiently high to overcome the Casimir-Polder interaction effect at such short distances from the surface. Details of the experiment procedures and simulation results are discussed in the following.

After the RF cooling stage in the Z-wire trap, the atom cloud is merged with the magnetic lattice traps, which are located around 200 nm below the chip surface, for a constant bias field B_x. This merging procedure is performed by ramping down the Z-wire current further to various final values until the Z-wire trap overlaps the magnetic lattice trapping potential. The ramping was performed slowly while B_y is turned off and B_x is kept constant. Lattice loading was performed for a range of bias field settings $B_x = 9$, 14, 26, 40 and 52 G.

Figure 5.6 (a) shows the magnetic film pattern which is designed for a triangular magnetic lattice optimized for a trap distance $h = a/2$ from the magnetic film surface. To obtain the optimized triangular magnetic lattice potential for the film

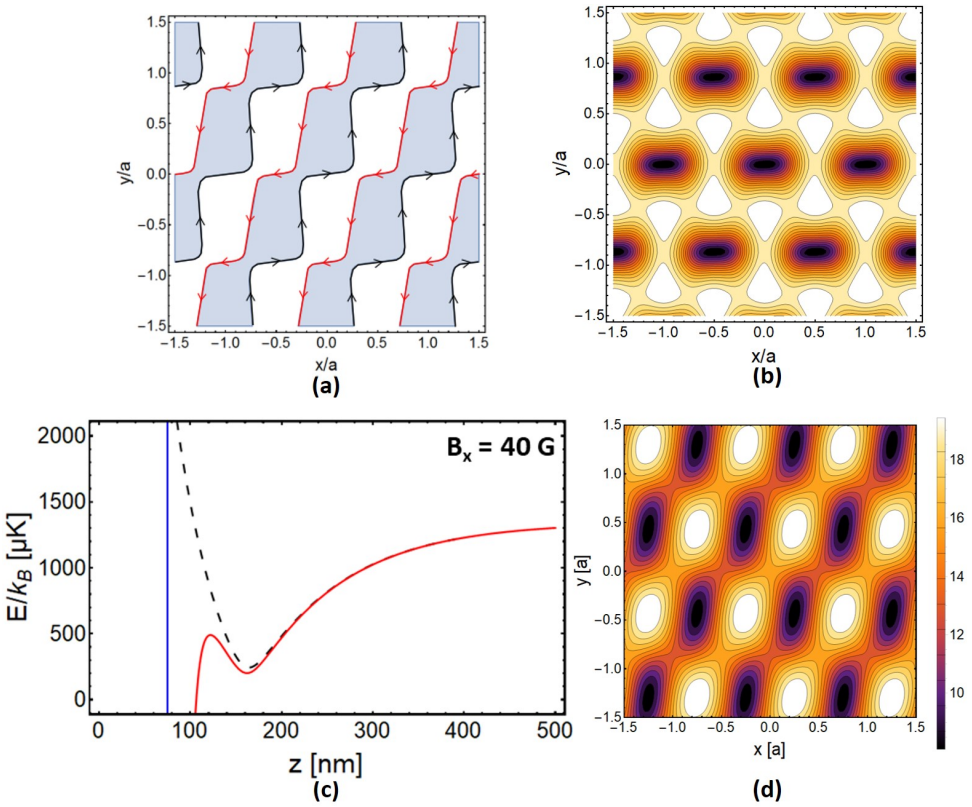

Figure 5.6: (a) Optimized magnetic film pattern for a triangular magnetic lattice at a vertical trap distance $h = a/2$, with bias fields $B_x = 0.5\,\mathrm{G}$, $B_y = 4.5\,\mathrm{G}$. (b) Calculated potentials at the optimum trapping plane height. Dark regions represent trapping potential minima. (c) Simulated trapping potential for ^{87}Rb $|F = 1, m_F = -1\rangle$ atoms trapped in a 0.7 μm-period triangular magnetic lattice for a bias field $B_x = 40\,\mathrm{G}$, $B_y = 0\,\mathrm{G}$ and (d) calculated pseudo-potentials at the trapping plane height at the trap minimum. Vertical blue line in (c) is the nominal position of the silica surface ($z = 75\,\mathrm{nm}$). Black dashed line in (c) represents the magnetic lattice trapping potential, and the red line is the combined magnetic lattice trapping potential and the attractive Casimir-Polder potential for a silica surface ($C_4 = 8.2 \times 10^{-56}\mathrm{Jm}^4$). Input parameters of the simulations: $4\pi M_z = 5.9\,\mathrm{kG}$, $t_m = 10.34\,\mathrm{nm}$.

magnetization $4\pi M_z = 5.9\,\mathrm{kG}$ and magnetic film thickness t_m =10.34 nm, we need to apply bias fields $B_x = 0.5\,\mathrm{G}$, $B_y = 4.5\,\mathrm{G}$. As can be seen in Figure 5.6 (b), each trap minimum, which is shown as a dark region, is surrounded by six potential

maxima. For our magnetic trapping potential created by applying $B_x = 40\,\mathrm{G}$, $B_y = 0\,\mathrm{G}$ (shown in Figure 5.6 (c)), the traps are more elongated and tighter compared with the traps for the optimized lattice and they are surrounded by four potential maxima (Figure 5.6 (d)). This is explained as follows. As the magnetic film is magnetized in the vertical z-direction, the surface magnetization can be considered as a virtual current running along the edges of the etched structure of the magnetic film (Figure 5.6 (a)). Because the bias field is applied in the x-direction B_x, the magnetic field from the current running along the red edges of the magnetic film is cancelled, which leads to elongated magnetic traps along the long red edges. Because increasing the bias field strength B_x increases the trapping frequencies, the barrier heights increase accordingly while the distance from the trapping potential minima to the chip surface decreases resulting in a stronger effect of the Casimir-Polder interaction on the trapping potential. On the other hand, as no bias field is applied in the y-direction B_y, the magnetic field from the virtual current running along the horizontal black edges of the magnetic film is not affected and there are no magnetic traps created along the short horizontal black edges.

The loading procedure begins with a thermal cloud of $\sim 5 \times 10^5$ ^{87}Rb $|F = 1, m_F = -1\rangle$ atoms at $\sim 1\,\mu$K prepared in the Z-wire trap at $\sim 670\,\mu$m from the chip surface with $I_z = 38\,\mathrm{A}$ and $B_x = 52\,\mathrm{G}$. For lattice trapping at $B_x = 52\,\mathrm{G}$, the trapping sequence is rather straightforward since there is no change in the bias field in transferring from the Z-wire trap to the magnetic lattice traps. This is conveniently implemented by just ramping down the Z-wire current to an appropriate value so that the Z-wire trap can merge with the magnetic lattice potential. For the smaller $B_x = 9$, 14, 26, 40 G, the procedure is more complex since B_x needs to be reduced first before loading atoms into the magnetic lattice traps. As we reduce B_x, the Z-wire magnetic trap position changes accordingly and this would result in the Z-wire cloud being pushed further away from the surface. In order to compensate for this change, the Z-wire current needs to be reduced at the same time as B_x and should be carefully monitored to minimize atom losses during atom transfer and any sloshing in the magnetic lattice traps. In the experiment, the response time for

reducing the Z-wire current is about 0.1 ms and the response time of the two large Helmholtz coils that produce the bias field B_x is about 10 ms. This fact was taken into account in calculating the experimental parameters so that the change of the Z-wire trap position is minimal. This stage is carried out in 146 ms.

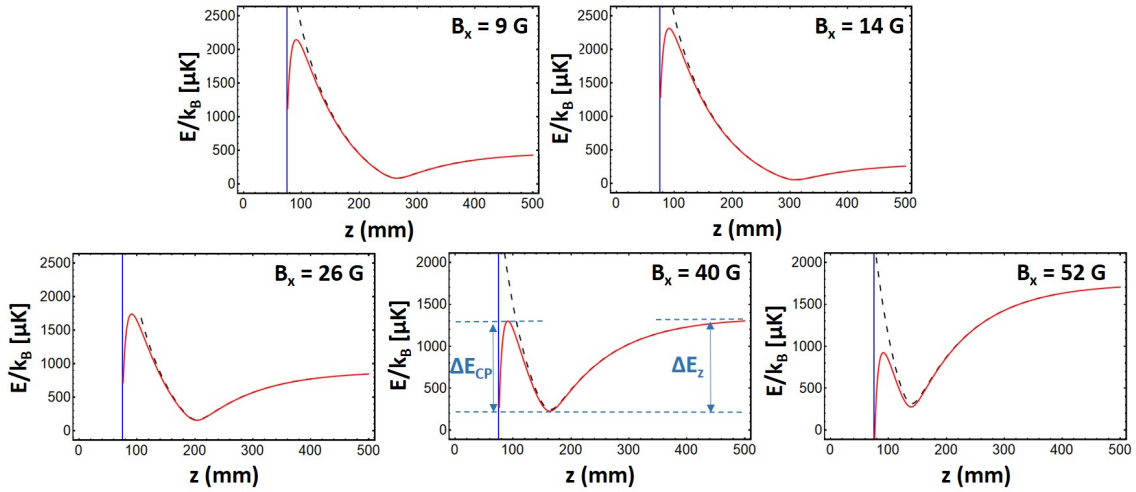

Figure 5.7: Simulated trapping potentials for ^{87}Rb $|F = 1, m_F = -1\rangle$ atoms trapped in a 0.7 μm-period triangular magnetic lattice for various bias fields B_x and B_y= 0 with an offset parameter $\delta d = 25$ nm. The black dashed lines represent the magnetic lattice trapping potentials, and the red lines are the combined magnetic lattice trapping potential and the attractive Casimir-Polder potential for a silica surface ($C_4 = 8.2 \times 10^{-56}$Jm^4). The blue solid line represents the nominal atom chip surface position at z = 75 nm.

Figure 5.7 shows calculated trapping potentials for ^{87}Rb $|F = 1, m_F = -1\rangle$ atoms trapped in a 0.7 μm-period triangular magnetic lattice for various bias fields $B_x = 9$, 14, 26, 40, 52 G and $B_y = 0$, where the coefficient for the attractive Casimir-Polder potential for a silica surface is taken to be the calculated value $C_4 = 8.2 \times 10^{-56}$Jm^4 and an offset parameter $\delta d = 25$ nm is used (see Section 5.5 for discussion). As shown in Table 5.1, the calculated geometric mean trapping frequencies $\overline{\omega}/2\pi$ for the lattice traps are high, ranging from ~ 330 kHz to ~ 830 kHz, which are sufficiently high to largely compensate the Casmir-Polder effect. For $B_x \geq 40$ G, for which the distance from the trap centre to the chip surface is $d < 130$ nm, the Casimir-Polder force

starts to affect the lattice traps and the effective trap depth of the lattice potential is determined by the Casimir-Polder interaction $\Delta E_{eff} \equiv \Delta E_{CP}$ (Figure 5.7). For bias fields $B_x < 40\,\mathrm{G}$, the Casimir-Polder effect is insignificant and the effective trap depth of the lattice potential is determined by $\Delta E_{eff} \equiv \Delta E_z$.

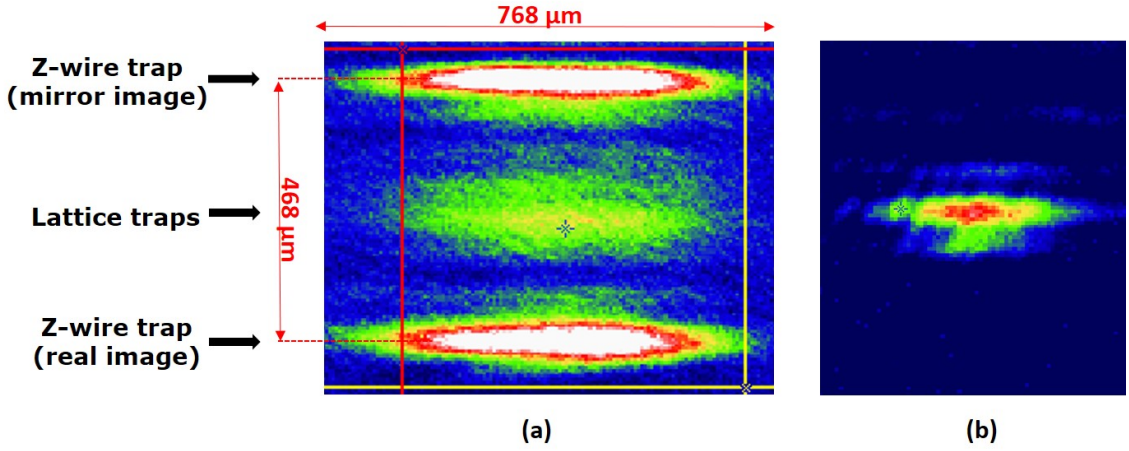

Figure 5.8: Reflection absorption images of ^{87}Rb $|F = 1, m_F = -1\rangle$ atoms trapped (a) in the 0.7 μm-period triangular magnetic lattice mid-way between the real and mirror images of the Z-wire trapped cloud for $B_x = 52\,\mathrm{G}$ and (b) in the 0.7 μm-period triangular magnetic lattice only for $B_x = 14\,\mathrm{G}$. The temperature of the Z-wire trapped cloud is 1.3 μK.

The key task of the magnetic lattice loading experiments is to optimize the ramping speed. If the Z-wire current is ramped down too quickly the Z-wire trapped cloud would receive a large launching force so that it would penetrate the lattice trapping potential and hit the chip surface and become lost. On the other hand, if the Z-wire current is ramped too slowly, in the region where the atom cloud is very close to the chip surface, the atoms may be lost because of atom-surface interactions and atom sloshing. Next, the Z-wire current is further ramped down to a small value so that the Z-wire trap can merge with the magnetic lattice potential and I_z is rapidly ramped up in 2 ms to bring the Z-wire cloud further away from the surface for *in situ* imaging.

Figure 5.8 (a) shows a representative reflection absorption image for $B_x = 52$

Table 5.1: Calculated parameters for ^{87}Rb $|F = 1, m_F = -1\rangle$ atoms trapped in the 0.7 μm-period triangular magnetic lattice, for $4\pi M_z = 5.9$ kG, $t_m = 10.34$ nm, $C_4 = 8.2 \times 10^{-56}$ Jm^4 and offset parameter $\delta d = 25$ nm. The distance of the trap minima from the chip surface is $d = z_{min} - (t_{\mathrm{Au}} + t_{\mathrm{SiO_2}}) + \delta d = z_{min} - 50$ nm. B_{IP} is the Ioffe-Pritchard (minimum) magnetic field.

Bias field B_x (G)	z_{min} (nm)	d (nm)	B_{IP} (G)	$\omega_{\perp,\parallel}/2\pi$ (kHz)	$\overline{\omega}/2\pi$ (kHz)	$\Delta E_{x,y}/k_B$ (μK)	$\Delta E_z/k_B$ (μK)	$\Delta E_{CP}/k_B$ (μK)
9	310	260	1.6	618, 94	330	359, 232	244	2258
14	267	217	2.5	772, 115	409	559, 362	376	2072
26	203	153	4.7	1097, 153	569	1104, 729	731	1584
40	163	113	6.7	1405, 185	715	1703, 1155	1118	1075
52	139	89	8.2	1657, 207	828	2233, 1554	1465	655

G. The clouds at the bottom and top of the figure are the real and mirror images of the atoms remaining in the Z-wire trap, respectively. The cloud in the middle is attributed to the unresolved direct and mirror images of atoms trapped in multiple sites of the magnetic lattice very close ($\sim$90 nm) to the chip surface. Due to the limited resolution of the imaging system, it is not possible to resolve the direct and mirror images of the lattice trapped cloud, which are separated by only $\sim 0.2\,\mu$m, and atoms in individual lattice sites, which are separated by 0.7 μm. Similar images of the lattice trapped clouds are observed for the other values of the bias field B_x.

In conjunction with the above experiments, another lattice loading experiment was performed in order to verify that the atoms are trapped in the magnetic lattice. This experiment starts by bringing the Z-wire trapped cloud up close to the chip surface to merge with the magnetic lattice trap potential and then I_z is quickly switched to a small value, or I_z is completely switched off, while keeping the bias field constant at $B_x = 14$ G. This projects the Z-wire trap cloud in the vertical direction so that the cloud hits the chip surface and is removed while the small atom cloud mid-way between the two images of the Z-wire cloud remains visible (Figure 5.8 (b)). This is a good test for the authenticity of the trapped cloud since

if atoms are actually trapped in the magnetic lattice, they should remain at their original position when the Z-wire magnetic trap is turned off.

Immediately after turning off the Z-wire trap, typically $\sim 2 \times 10^4$ atoms are trapped in the 0.7 μm-period magnetic lattice in an area of $\sim 180\,\mu\text{m} \times 13\,\mu\text{m}$ (FWHM). This area corresponds to ~ 4900 lattice sites which gives $\overline{N}_{site} \approx 4$ atoms per site.

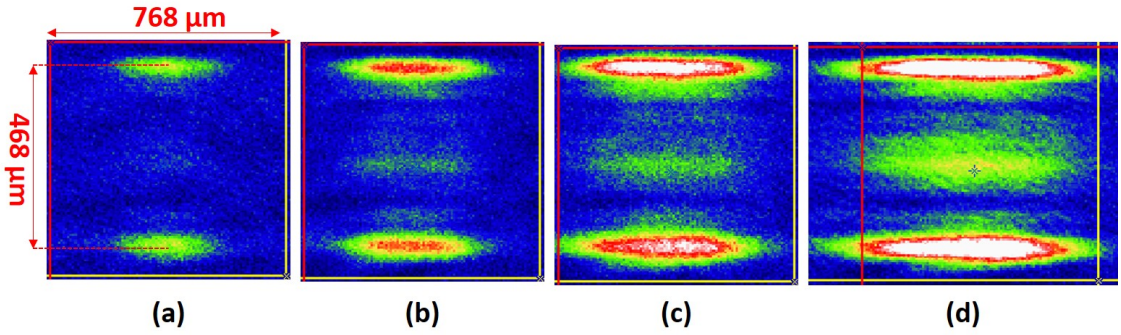

Figure 5.9: Reflection absorption images of ^{87}Rb $|F = 1, m_F = -1\rangle$ atoms trapped in the 0.7 μm-period triangular magnetic lattice mid-way between the real and mirror images of the Z-wire trapped cloud for different Z-trap cloud temperatures: (a) 0.3 μK, (b) 0.5 μK (c) 0.7 μK and (d) 1.3 μK with the number of magnetic lattice trapped atoms $N \sim 200, 1.2 \times 10^3, 2.5 \times 10^3$ and 4×10^3, respectively. The measurements of the number of atoms were taken after 2 ms of bringing the Z-wire trapped atom cloud further from the chip surface for imaging. The bias field was $B_x = 52$ G.

Similar lattice trapping experiments were performed with different initial temperatures of the Z-wire trapped cloud and hence for clouds with different sizes and Z-wire trapped atom numbers. After bringing the Z-wire trapped atom cloud close to the chip surface, it was then moved further from the surface in 2 ms to measure the number of atoms trapped in the magnetic lattice. As can be seen in Figure 5.9, with a larger cloud, it is possible to load more atoms in the magnetic lattice sites, from $N \sim 200$ atoms at $T \sim 0.3\,\mu$K up to $N \sim 4 \times 10^3$ at $T \sim 1.3\,\mu$K.

An additional trapping experiment was carried out by carefully launching the atom cloud towards the chip surface. At first, using a bias field B_{bx}= 52 G, the Z-wire trapped cloud is brought from 670 μm to around 130 μm from the chip surface by ramping down just the I_z value. At this position, the Z-wire current and the bias magnetic field B_x are quickly switched off simultaneously. The delay in response time between I_z and B_x, as discussed in Section 5.2, projects the atom cloud towards the chip surface. As a result, this sudden switch-off creates a vertical force launching the cloud towards the chip surface, so that it interacts with the magnetic lattice potential before falling down under gravity.

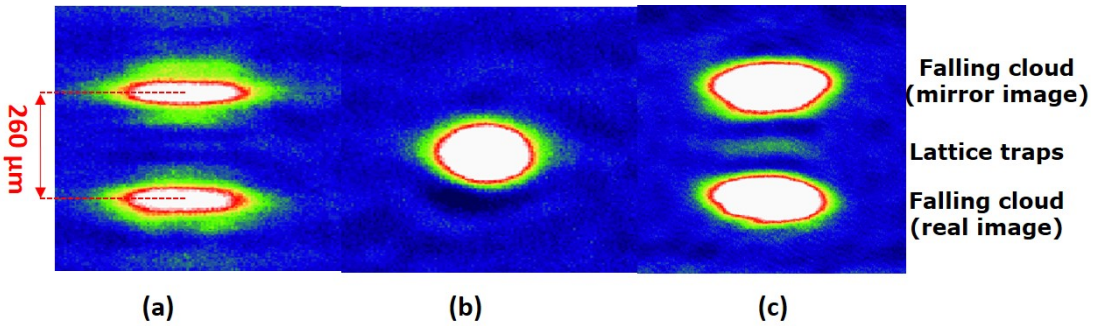

Figure 5.10: Reflection absorption images of ^{87}Rb $|F = 1, m_F = -1\rangle$ atoms trapped in the 0.7 μm-period triangular magnetic lattice for B_x = 52 G after projecting a Z-wire trapped atom cloud vertically towards the chip surface after TOF of 0 ms (a), 2 ms (b) and 3 ms (c). The small atom cloud mid-way between the real and mirror images of the Z-trap cloud in (c) is attributed to the magnetic lattice trapped atom cloud.

Immediately after launching the atom cloud, small bias fields in the negative x-direction, $B_x = -5.3$ G, and in the y-direction, $B_y = 6.1$ G, are applied for a short time of 3 ms. The bias field in the negative x-direction is produced by a pair of small Helmholtz coils, which have a much faster response time than the large Helmholtz coils used to produce B_x = 52 G . This applied magnetic field acts to cancel the residual bias magnetic field from the large magnetic coils. In addition, the bias field in the y-direction, B_y = 6.1 G, acts to create a triangular magnetic lattice similar to the optimized triangular lattice in Figure 5.6(b). This experiment was performed

by trial and error using different launching speed. At the optimal launching speeds, part of the atom cloud merges with the magnetic lattice trap potential and is trapped there while the remaining part of the cloud falls down under gravity, as can be seen in Figure 5.10. The occurrence of some surface evaporative cooling provides the dissipation required for atoms to remain trapped in the conservative potential of the magnetic lattice. The lattice trapped cloud appears after 3 ms time of flight and then disappears after a further 1.5 ms which is consistent with the lifetimes measured in the experiments below. When the experiment is repeated using the same initial experimental parameters but without applying external bias fields B_x and B_y, no trapped cloud is observed.

5.5 Lifetimes of atoms trapped in the 0.7 μm-period triangular lattice

The lifetime of the atoms trapped in the triangular magnetic lattice was measured by recording the atom number remaining in the lattice versus holding time for various values of the bias field B_x, and hence for various values of the distance $z = z_{min}$ from the magnetic film. The results shown in Figure 5.11 are decay curves for B_x = 9, 14, 26, 40, 52 G. A single exponential function is employed for fitting the decay curves. The smaller number of atoms in the images in Figure 5.9 is due to the measurement being made after ramping up the Z-wire current for 2 ms, while the atom number shown at the start of the decay curves in Figure 5.11 was taken immediately after the atom cloud was trapped in the magnetic lattices. Due to the sensitivity limitation of our imaging system, very low numbers of atoms are not detectable which hinders the observation of any small non-exponential tail in the decay curves. The lifetimes of the trapped atoms are rather short varying from 0.43 ± 0.06 ms for $B_x = 52$ G up to 1.69 ± 0.11 ms for $B_x = 9$ G. These lifetimes increase approximately linearly with distance $d = z - (t_{Au} + t_{SiO_2})$ from the chip surface and are much longer than the corresponding lattice trap oscillation periods (1 - 3 μs). Various loss mechanisms are considered to explain the short lifetimes:

one-dimensional thermal evaporation, three-body recombination and Johnson noise.

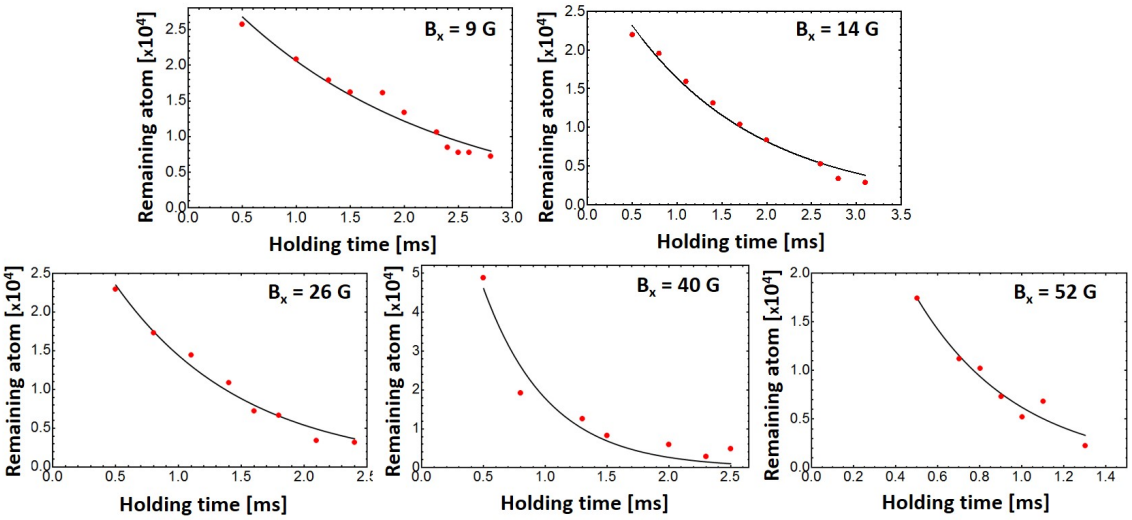

Figure 5.11: Decay curves for atoms trapped in the 0.7 μm-period triangular magnetic lattice for $B_x = 9,\ 14,\ 26,\ 40,\ 52$ G. The solid lines are single exponential fits to the data corresponding to $\tau = 1.69 \pm 0.11\,ms$, $1.24 \pm 0.07\,ms$, $0.9 \pm 0.06\,ms$, $0.78 \pm 0.11\,ms$, $0.43 \pm 0.06\,ms$. Time zero is chosen arbitrarily.

When the Z-wire trapped atom cloud is transferred to the tight magnetic lattice traps, the cloud is heated by adiabatic compression resulting from the large increase in trapping frequency from $\overline{\omega}/2\pi = 84 - 113$ Hz in the Z-wire trap to $\overline{\omega}/2\pi = 330 - 830$ kHz in the magnetic lattice traps, depending on the bias field $B_x = 9 - 52$ G, and hence distance d from the chip surface $d = 260 - 89$ nm, respectively. The transfer therefore introduces significant heating of the cloud, from an initial temperature $T \approx 1\,\mu$K to an estimated $\sim 3 - 8$ mK. Atoms with energies higher than the effective lattice trap depth $\Delta E_{eff} = \min\{\Delta E_z, \Delta E_{CP}\}$ quickly escape the trap. After this sudden truncation of the high energy tail of the Boltzmann distribution, energetic atoms with energies comparable to the effective lattice trap depth ΔE_{eff}, which populate the edge of the lattice traps, are rapidly lost by escaping from the traps, spilling over into neighbouring lattice traps, or by three-body recombination.

Through rethermalization by elastic collisions, the remaining atoms reach a quasi-equilibrium state at a lower temperature due to the fact that the energies of the lost

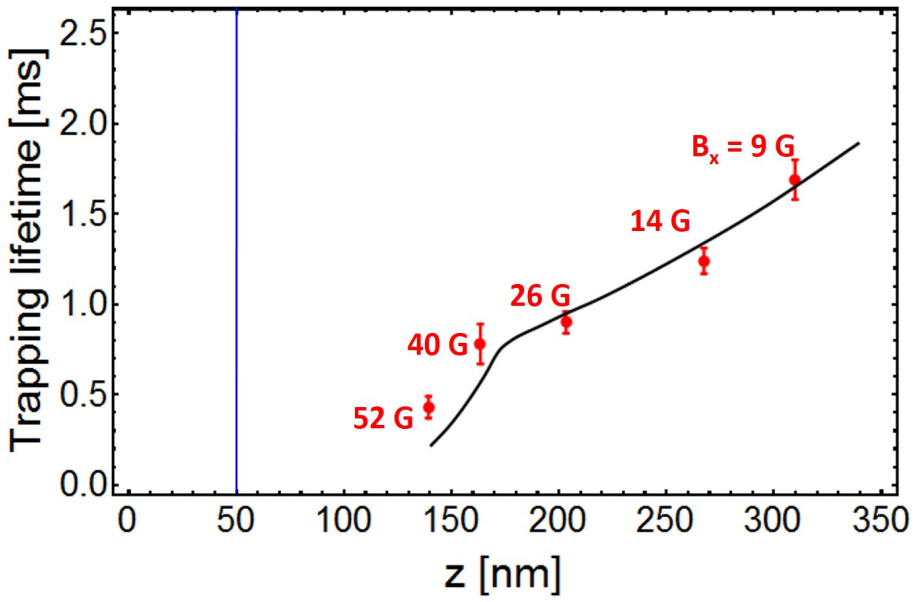

Figure 5.12: Measured lifetimes (red points) of atoms trapped in the magnetic lattice versus distance z of the magnetic lattice trap centre from the magnetic film surface. The B_x values (in G) are shown and the error bars are 1σ statistical uncertainties. The black curve shows the calculated evaporation lifetime τ_{ev} versus z for $\overline{N}_{site} = 1.5$, $\eta = 4$, offset $\delta d = 25\,\text{nm}$. The vertical blue line indicates the position of the silica surface at $z = 50$ nm, allowing for an offset of $\delta d = 25\,\text{nm}$.

atoms are greater than the energies of the remaining atoms. The quasi-equilibrium temperature can be approximated by $T \approx \Delta E_{eff}/(\eta k_B)$ where η is the truncation parameter. We estimate that there are initially of the order of 100 atoms per lattice site available for elastic collisions and evaporative cooling which provides dissipation to allow the atoms to be trapped in the conservative potential. At the beginning of the evaporation, the one-dimensional thermal evaporation loss is large and then decreases gradually as evaporation proceeds.

Using the 1D evaporation model in Section 5.3, the lifetime for one-dimensional thermal evaporation is [87]:

$$\tau_{ev} = \tau_{el}/[f(\eta)e^{-\eta}], \tag{5.1}$$

where $\tau_{el} = [n_0 \sigma_{el} \overline{v}_{rel}]^{-1}$ and $n_0 = \frac{\overline{N}_{site}}{(2\pi)^{3/2}}(\frac{M}{k_B T})^{3/2}\overline{\omega}^3$ is the peak atom density in the magnetic lattice traps. In this model, τ_{ev} scales as $\Delta E_{eff}/[\overline{\omega}^3 \overline{N}_{site} \eta f(\eta) e^{-\eta}]$. For

$B_x < 40\,\mathrm{G}$, where $\Delta E_{eff} \equiv \Delta E_z$ (Table 5.1), there is an almost linear increase of τ_{ev} with increasing distance d from the chip surface (Figure 5.12). This can be interpreted as follows: as the minima of the lattice traps are brought further from the atom chip surface, $\overline{\omega}^{-3}$ increases at a faster rate than ΔE_z decreases. On the other hand, for $B_x \geq 40\,\mathrm{G}$, where $\Delta E_{eff} \equiv \Delta E_{CP}$ (Table 5.1), there is a sharp decrease in τ_{ev} with decreasing d. This is due to the fact that when the minima of the lattice traps are brought to a very small distance from the chip surface both ΔE_{CP} and $\overline{\omega}^{-3}$ decrease together with decreasing z.

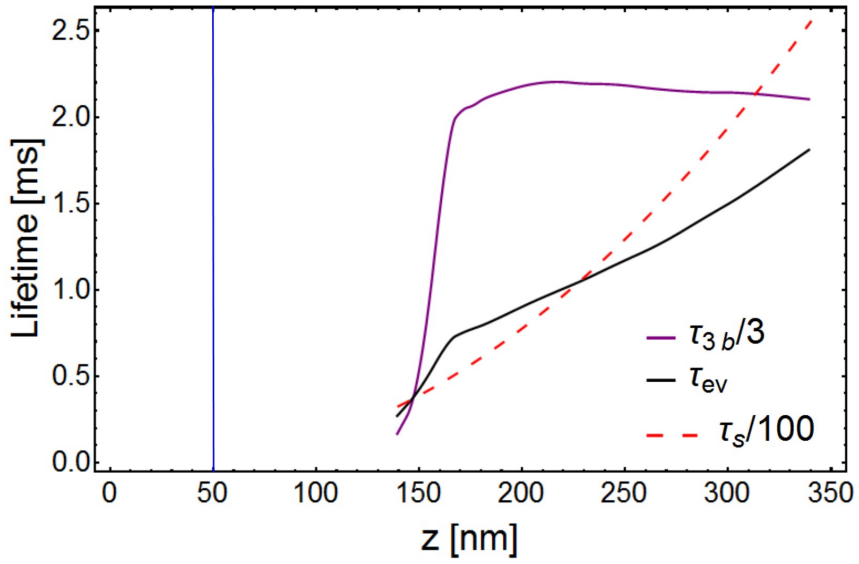

Figure 5.13: Calculated lifetimes for 1D evaporation τ_{ev} (black), three-body recombination τ_{3b} (purple) and spin flips τ_s (dashed red) for $\overline{N}_{site} = 1.5$, $\eta = 4$, $\delta d = 25\,\mathrm{nm}$. The curves for τ_{3b} and τ_s are reduced by factors of 3 and 100, respectively. The vertical blue line indicates the position of the silica surface at $z = 50$ nm, allowing for an offset of $\delta d = 25\,\mathrm{nm}$.

In the very tight magnetic lattice traps, atoms can be lost via three-body recombination. For a non-condensed cloud of ^{87}Rb atoms in the $|F = 1, m_F = -1\rangle$ state, the lifetime for (non-exponential) decay by 3-body recombination is $\tau_{3b} = 1/(K_3 n_0^2)$, where $K_3 = 4.3(1.8) \times 10^{-29}\,\mathrm{cm^6 s^{-1}}$ [56]. Therefore, τ_{3b} scales as $\Delta E_{eff}^3/[\overline{\omega}^6 \overline{N}_{site}^2 \eta^3]$. For $B_x < 40\,\mathrm{G}$ where $\Delta E_{eff} \equiv \Delta E_z$, as B_x decreases, the rate at which ΔE_z^3 decreases is comparable to the rate at which $\overline{\omega}^{-6}$ increases. Thus, there is almost no

change in τ_{3b} observed for distances $z > 170\,\text{nm}$ as shown by the purple (top) curve of Figure 5.13. For increasing $B_x \geq 40\,\text{G}$ where $\Delta E_{eff} \equiv \Delta E_{CP}$, a rapid decrease in τ_{3b} is observed. This is due to the fact that as B_x increases, the trap minima are brought very close to the chip surface and ΔE_{CP}^3 and $\overline{\omega}^{-6}$ both decrease strongly together with decreasing z.

In addition, Johnson magnetic noise from currents induced in the gold coating layer of the magnetic film structures may cause atom loss through Majorana spin-flips (Sect. 2.4.3). The Johnson spin-flip lifetime is given by $\tau_s = \frac{256\pi\hbar^2 d}{3\mu_0^2\mu_B^2\sigma k_B T g(d,t_{Au},\delta)}$ for the state $|F = 1, m_F = -1\rangle$ [77], where $g(d, t_{Au}, \delta) \approx t_{Au}/(t_{Au} + d)$ for $\delta \gg \text{Max}\{d, t_{Au}\}$, $\delta = \sqrt{2/(\sigma\mu_0\omega_L)}$ is the skin depth at the spin-flip transition frequency $\omega_L = m_F g_F \mu_B B_{IP}/\hbar$; σ is the electrical conductivity of the conducting layer, and μ_0 is the vacuum permeability [93]. According to our calculations, the Johnson spin-flip lifetimes for $t_{Au} = 50\,\text{nm}$ are much longer than the measured magnetic lattice trap lifetimes, as shown by the dashed red in Figure 5.13. For example, the calculated lifetimes are $\tau_s = 48\,\text{ms}$ for $d = 110\,\text{nm}$ and $\tau_s = 230\,\text{ms}$ for $d = 290\,\text{nm}$.

Generally, the calculated one-dimensional evaporation lifetime versus distance curve (Figure 5.12), which has a positive slope given approximately by $\Delta E_{eff}/(\overline{\omega}^3 d)$, fits the measured lifetime versus distance curve satisfactorily. On the hand, the three-body recombination lifetimes versus distance curve is almost constant for $z > 170\,\text{nm}$ and the calculated Johnson spin-flip lifetimes are much longer than the experimental lifetimes (Figure 5.13). Therefore, we attribute the main mechanism for loss of atoms in the lattice traps to one-dimensional thermal evaporation, rather than to the other two mechanisms. It is expected that some atoms will remain in the magnetic lattice traps after thermal evaporation for times much longer than 1 ms. However, no non-exponential tail in the decay curves is observed within our detection sensitivity.

As can be seen in Figure 5.12, the parameters $\overline{N}_{site} = 1.5$, $\eta = 4$ and an offset $\delta d = 25\,\text{nm}$ allow a reasonable fit of the calculated evaporation lifetime to the measured lifetimes. A value $\overline{N}_{site} \approx 1.5$, which is smaller than the estimated $\overline{N}_{site} \approx 4$, is required to keep the evaporation lifetime much smaller than the three-body recombi-

nation lifetime which exhibits a different dependence on distance z. This difference in $\overline{N}_{site}$ could be explained as a result of atoms spilling over into neighbouring lattice sites during the initial transfer of atoms from the Z-wire trap to the magnetic lattice traps, so that at the time the lifetime measurements are taken, there are actually more than 4900 lattice sites occupied. On the other hand, the difference may be due to uncertainties in the estimated size of the Z-wire magnetic trap cloud or the estimated total number of atoms trapped in the magnetic lattice. An average value $\overline{N}_{site} \approx 1.5$ is consistent with the end product of a rapid three-body recombination process which occurs before the observation period leaving, 2, 1 or 0 atoms on any given lattice site.

To achieve a good fit between the calculated evaporation lifetime and the measured magnetic lattice trapping lifetimes in the region of very small distances d to the magnetic film surface, the calculated Casimir-Polder interaction coefficient $C_4 = 8.2 \times 10^{-56}\mathrm{Jm}^4$ is required to be smaller by an order of magnitude or the calculated distances of the trapped atoms from the chip surface $d = z_{min} - (t_{\mathrm{Au}} + t_{\mathrm{SiO_2}})$ are required to be larger by $\delta d \approx 25$ nm.

The uncertainty in the calculated C_4 value is expected to be $\sim 40\%$ based on the the level of agreement between the calculated C_4 value and the measured value for a dielectric sapphire surface film [119]. On the other hand, for our fabricated magnetic lattice film, the estimated uncertainty $\left(^{+40}_{-30}\,\mathrm{nm}\right)$ in $d = z_{min} - (t_{\mathrm{Au}} + t_{\mathrm{SiO_2}})$ for $B_x = 40\,\mathrm{G}$ and $52\,\mathrm{G}$ has contributions from a systematic error of about $+10$ nm from the 20 nm-deep etching of the patterned film, the uncertainties in the thickness of the gold and silica coating layer of the magnetic film ($\pm\,5\,\mathrm{nm}$) and z_{min} ($\pm\,25\,\mathrm{nm}$) and the effect of the estimated uncertainty in C_4 ($\pm\,2\,\mathrm{nm}$) [35]. Thus, an offset of $\delta d = 25\,\mathrm{nm}$ is considered to be within the estimated uncertainty $\left(^{+40}_{-30}\,\mathrm{nm}\right)$ in $d = z_{min} - (t_{\mathrm{Au}} + t_{\mathrm{SiO_2}})$ for $B_x = 40\,\mathrm{G}$ and $52\,\mathrm{G}$.

5.6 Trapping ^{87}Rb atoms in the 0.7 μm-period square lattice

In the above section, ^{87}Rb atoms were successfully trapped in a 0.7 μm-period *triangular* magnetic lattice. Due to the high trapping frequencies in the magnetic lattice traps, atoms could be trapped at distances down to $\sim 90\,\text{nm}$ from the chip surface. However, the trap lifetimes are short, even for a relatively low bias magnetic field. In the next stage, we trap atoms in the 0.7 μm-period *square* magnetic lattice using a similar loading procedure to the triangular magnetic lattice. Since for an optimized square magnetic lattice, the main bias field is along the x-direction (i.e., B_x), it is expected that the trapping should be more straightforward.

Figure 5.14 (a) shows the magnetic film pattern designed for a square magnetic lattice that is optimized for a trap distance $h = a/2$ from the magnetic film surface. To obtain the optimized square magnetic lattice potential for the film magnetization ($4\pi M_z = 5.9\,\text{kG}$) and magnetic film thickness (t_m =10.34 nm), it is required to apply bias fields $B_x = 7.5\,\text{G}$, $B_y = 3.6\,\text{G}$. As can be seen, for a square magnetic lattice each potential minimum, which is shown as a dark region, is surrounded by four potential maxima. For our trapping potential created by applying $B_x = 11\,\text{G}$, $B_y = 0\,\text{G}$ (shown in Figure 5.14 (c)), the barrier heights in the y and z-directions are much smaller than in the x-direction (Table 5.2) and the traps tend to resemble a periodic array of 1D magnetic traps. Additionally, the traps are more elongated and are looser than for the optimized triangular lattice and each potential minimum is surrounded by two large and two small potential maxima.

For comparison with the simulated results for the triangular magnetic lattice, calculations of the trap potentials for the 0.7 μm-period square magnetic lattice were performed for the same bias field configuration, as shown in Figure 5.15. The Casimir-Polder interaction coefficient $C_4 = 8.2\times10^{-56}\text{Jm}^4$ and the offset $\delta d = 25\,\text{nm}$ are still employed. Generally, the trend in the change in trapping parameters with B_x bias field in the square magnetic lattice is similar to that of the triangular magnetic

lattice. However, the lattice trap minimum is further away from the chip surface for the same bias magnetic field strength B_x, which results in the trapping frequencies being 2 to 3 times smaller. This is a key factor for reducing losses caused by 1D thermal evaporation, 3-body recombination, heating due to adiabatic compression and the Casimir-Polder force. However, for the same bias magnetic field, the effective trap depth is smaller for the square magnetic lattice potentials, which increases the atom loss through 1D evaporation near the chip surface.

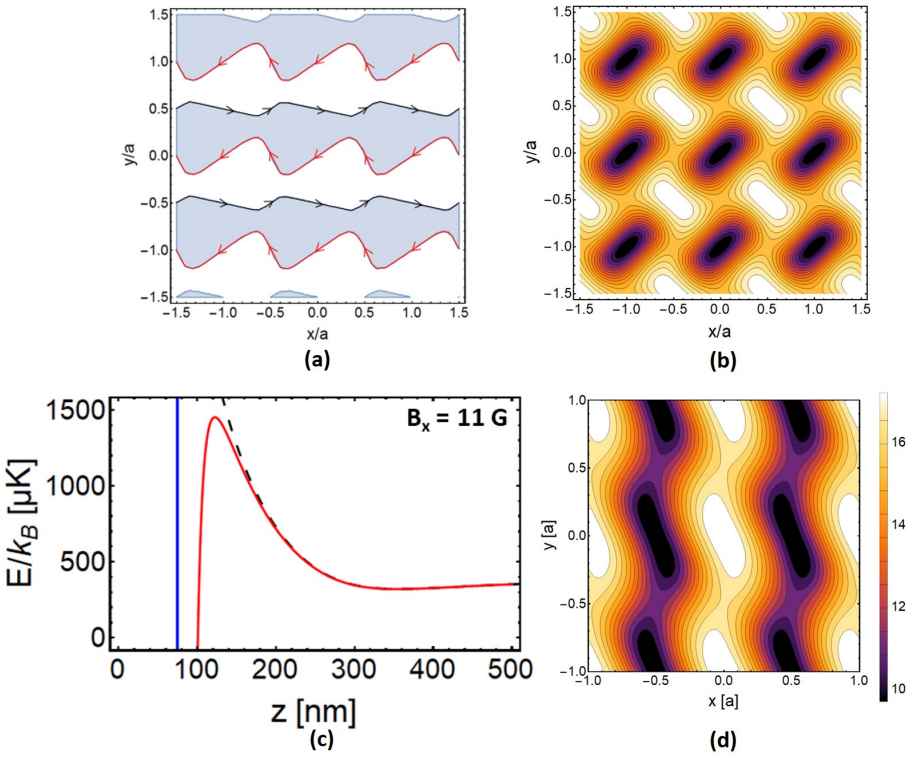

Figure 5.14: (a) Optimized magnetic film pattern for a square magnetic lattice at a vertical trap distance $h = a/2$ and (b) calculated pseudo-potentials at the optimum trapping plane height. The bias fields required are $B_x = 0.5$ G and $B_y = 4.5$ G. Dark regions represent the trapping potential minima. (c) Simulated trapping potential for ^{87}Rb $|F = 1, m_F = -1\rangle$ atoms trapped in a 0.7 μm-period square magnetic lattice for a bias field $B_x = 11$ G, $B_y = 0$ and (d) calculated pseudo-potentials in the trapping plane at the trap minimum. Vertical blue line in (c) is the nominal position of the silica surface ($z = 75$ nm). Input parameters of the simulations: $4\pi M_z = 5.9$ kG, $t_m = 10.34$ nm.

Table 5.2: Calculated parameters for ^{87}Rb $|F = 1, m_F = -1\rangle$ atoms trapped in the 0.7 μm-period square magnetic lattice, for $4\pi M_z = 5.9\,\text{kG}$, $t_m = 10.34\,\text{nm}$, $C_4 = 8.2 \times 10^{-56}\,\text{Jm}^4$ and offset parameter $\delta d = 25\,\text{nm}$. The distance of the trap minima from the chip surface is $d = z_{min} - (t_{\text{Au}} + t_{\text{SiO}_2}) + \delta d = z_{min} - 50\,\text{nm}$. B_{IP} is the Ioffe-Pritchard (minimum) magnetic field.

Bias field B_x (G)	z_{min} (nm)	d (nm)	B_{IP} (G)	$\omega_{\perp,\parallel}/2\pi$ (kHz)	$\overline{\omega}/2\pi$ (kHz)	$\Delta E_{x,y}/k_B$ (μK)	$\Delta E_z/k_B$ (μK)	$\Delta E_{CP}/k_B$ (μK)
9	384	334	7.7	156, 29	89	156, 21	42	2028
10.5	364	314	8.9	175, 35	103	189, 27	51	1947
11	358	308	9.3	181, 39	109	200, 29	54	1920
13.5	330	280	11.3	211, 44	125	261, 40	70	1787
15	316	265	12.5	229, 54	142	301, 48	81	1709

A similar loading procedure was used to trap atoms in the 0.7 μm-period square magnetic lattice. The experiment setup is the same except the Z-wire and U-wire traps are now above the square magnetic lattice structure instead of the triangular magnetic lattice structure. This is easily implemented by switching the pinhole connections on the atom chip (Figure 3.1).

At first, a thermal cloud of $\sim 5 \times 10^5$ ^{87}Rb $|F = 1, m_F = -1\rangle$ atoms at $\sim 1\,\mu$K is prepared in the Z-wire trap at $\sim 670\,\mu$m from the chip surface with $I_z = 38\,\text{A}$ and $B_x = 52\,\text{G}$. The loading procedure is performed by ramping down the Z-wire current further to various final values to bring the cloud closer to the chip surface until the Z-wire trapped atom cloud merges with the magnetic lattice trapping potential. The ramping is performed slowly while B_y is turned off and B_x is kept constant. The magnetic lattice trapping is first performed at similar bias field settings as in the triangular magnetic lattice: $B_x = 26\,\text{G}$, 40 and 52 G. However, no lattice trapping is observed when bias fields $B_x \geq 26\,\text{G}$ are applied. Lattice trapping occurs when we reduce the bias field down to $B_x = 15\,\text{G}$. The trapped cloud in the square magnetic lattice is similar to that in the triangular magnetic lattice shown in Figure 5.8.

The lifetime of the atoms trapped in the square magnetic lattice was measured

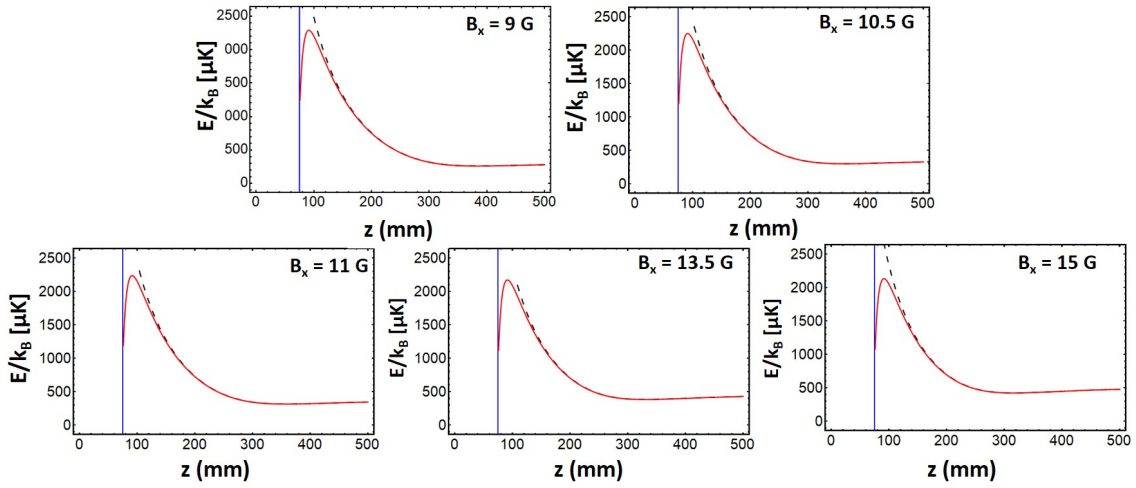

Figure 5.15: Simulated trapping potentials for ^{87}Rb $|F = 1, m_F = -1\rangle$ atoms trapped in a 0.7 μm-period square magnetic lattice for various bias fields B_x and $B_y = 0$ with an offset parameter $\delta d = 25$ nm. The black dashed curves represent the magnetic lattice trapping potentials, and the red curves are the combined magnetic lattice trapping potential and the attractive Casimir-Polder potential for a silica surface ($C_4 = 8.2 \times 10^{-56}$Jm^4). The blue solid line represents the nominal atom chip surface position at z= 75 nm

by recording the atom number remaining in the lattice versus holding time for various values of the bias field B_x, and hence for various distances $z = z_{min}$ from the magnetic film. The decay curves for B_x = 9, 10.5, 11, 13.5, 15 G are shown in Figure 5.16. The lifetimes range from 0.79 ± 0.07 ms for $B_x = 15\,G$ to 2.5 ms ± 0.25 ms for $B_x = 9\,G$ and tend to increase approximately linearly with distance $d = z-(t_{\mathrm{Au}}+t_{\mathrm{SiO_2}})$ from the chip surface, as shown by the black points in Figure 5.17. As with the decay curves for the triangular magnetic lattice (Figure 5.12), there is no definite evidence of a non-exponential tail within the sensitivity of our detection system.

When the Z-wire trapped atom cloud is transferred to the tight magnetic lattice traps, the cloud is heated by adiabatic compression resulting from a large increase in trapping frequency from $\overline{\omega}/2\pi = 84-88$ Hz in the Z-wire trap to $\overline{\omega}/2\pi = 89-142$ kHz in the magnetic lattice traps, for the bias field $B_x = 9 - 15$ G, and hence the

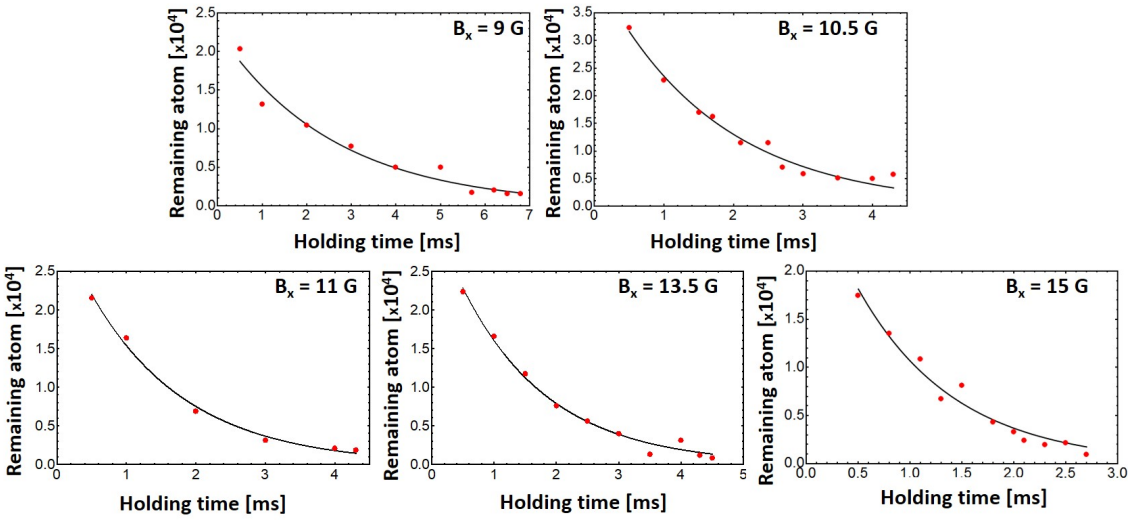

Figure 5.16: Decay curves for atoms trapped in the 0.7 μm-period square magnetic lattice for $B_x = 9$, 10.5, 11, 13.5, 15 G. The solid lines are single exponential fits to the data corresponding to $\tau = 2.46 \pm 0.25\,ms$, $1.78 \pm 0.12\,ms$, $1.56 \pm 0.09\,ms$, $1.17 \pm 0.07\,ms$, $0.82 \pm 0.07\,ms$. Time zero is chosen arbitrarily.

distance from the chip surface $d = 334 - 265$ nm, respectively. The transfer therefore introduces significant heating of the atom cloud, from an initial temperature $T \approx 1\,\mu$K to an estimated $\sim 1 - 2$ mK. The Casimir-Polder force is negligible in these cases since the lattice traps are far from the chip surface and the effective trap depth is determined purely by the magnetic lattice potentials $\Delta E_{eff} = \Delta E_z$. Furthermore, atom loss by three-body recombination is smaller because of the smaller trapping frequencies and hence smaller atom densities.

For the square magnetic lattice, the effective trap depth is much smaller than that of the triangular magnetic lattice for the same bias field B_x, and 1D evaporation is again the dominant loss mechanism. The parameters $\overline{N}_{site} \approx 1.6$ and $\delta d = 25$ nm, which are similar to the triangular magnetic lattice case, are employed to fit the calculated evaporation lifetime to the measured lifetimes as shown by the black curve in Figure 5.17. The value of $\overline{N}_{site} \approx 1.6$ is required to keep the evaporation lifetime much smaller than the three-body recombination lifetime. To obtain a reasonable fit to the steeply varying lifetime versus distance z curve using our model, we need

to assume a small and varying truncation parameter η. In the fit we assume a linear variation of η with distance from the chip surface, from $\eta = 1.53$ at $z = 384$ nm ($B_x = 9$ G) to $\eta = 1.10$ at $z = 316$ nm ($B_x = 14$ G). For a truncation parameter as small as $\eta = 1.5$, evaporative cooling will not have progressed very far and one might expect η to vary with barrier height and hence with distance from the chip surface.

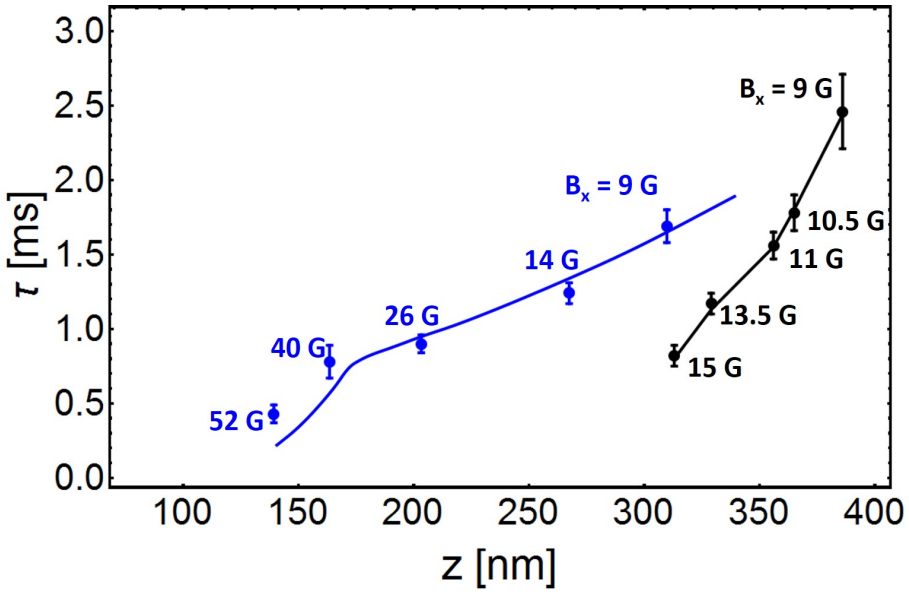

Figure 5.17: Measured lifetimes of atoms trapped in the square (black points) and triangular (blue points) magnetic lattices versus distance z of the magnetic lattice trap centre from the magnetic film surface. The B_x values (in G) are shown and the error bars are 1σ statistical uncertainties. The blue curve for the triangular magnetic lattice shows the calculated evaporation lifetimes τ_{ev} for $\overline{N}_{site} = 1.5$, $\eta = 4$, $\delta d = 25\,\text{nm}$. The black curve for the square magnetic lattice shows the calculated evaporation lifetimes τ_{ev} for $\overline{N}_{site} = 1.6$, $\eta = 1.53 - 1.11$ linearly decreasing with z_{min}, and $\delta d = 25\,\text{nm}$.

The rate at which the trap lifetime of atoms in the square magnetic lattice decreases with decreasing distance d is much larger than for the triangular magnetic lattice (Figure 5.17). For the square magnetic lattice, the spilling over of atoms into neighbouring lattice sites during the initial transfer of atoms from the Z-wire magnetic trap to the magnetic lattice traps can occur more easily than for the triangular

magnetic lattice because of the smaller minimum trap depth ΔE_y. Also, there is no sudden change in the slope of the lifetime curve as there is for the triangular magnetic lattice, since the Casimir-Polder interaction has no significant effect for the square magnetic lattice traps.

CHAPTER 6

Summary and future directions

6.1 Summary

In this thesis, we have reported the trapping of ultracold ^{87}Rb atoms in 0.7 μm-period triangular and square magnetic lattices on an atom chip.

In chapter 2 the theoretical background required for understanding the experiments described in this thesis was presented. This included the basic theory on Bose-Einstein condensation and the theory and conceptual framework for constructing the sub-micron period magnetic lattices and for the loss mechanisms of atoms trapped close to a surface.

In chapter 3 the fabrication and characterization of the triangular and square magnetic lattice structures on a Co/Pd multilayer magnetic film was described. The fabrication ultilizes an algorithm developed by Schmied *etal*. [28] which allows the design of optimized magnetic film patterns with the desired geometry and trapping parameters such as trapping heights, non-zero trap bottoms and trap depths. For the fabrication procedure, electron-beam lithography and reactive ion etching methods which give high etching resolution and high accuracy were employed. Additionally, a new direct bonded copper (DBC) atom chip was designed and fabricated with current-carrying wire structures for initial trapping of the ultracold atoms and

loading into the magnetic lattices. Together with the new Co/Pd magnetic lattice film, this atom chip forms a hybrid system that is used for trapping ultracold atoms in magnetic lattice traps.

In chapter 4 our experimental setup including the ultrahigh vacuum chamber, the laser optical system and the electronics control systems for trapping and cooling ^{87}Rb atoms were presented. Additionally, the experimental procedure and the creation of a BEC in a Z-wire magnetic trap used for loading the magnetic lattice traps were described.

In chapter 5 experiments demonstrating the trapping of ^{87}Rb atoms in the 0.7 μm-period triangular and square magnetic lattice were presented. Evidence for trapping in the sub-micron period magnetic lattices is based on the following observations:

(i) When the atom cloud in the Z-wire trap is launched vertically towards the chip surface, it interacts with the short-range magnetic lattice potential showing clear half-moon cloud shaped reflection signals.

(ii) When the Z-wire trap atom cloud is slowly brought very close to the chip surface, an atom cloud containing $\sim 2 \times 10^4$ atoms is observed mid-way between the real and mirror images of the Z-wire cloud detected by reflection absorption imaging. When the Z-wire magnetic trap is completely turned off, the atom cloud in the middle still remains.

(iii) When an atom cloud in the Z-wire trap is launched vertically towards the surface with optimized velocity and bias magnetic fields, a small atom cloud appears very close to the chip surface, mid-way between the direct and mirror images of the Z-trapped atom cloud.

(iv) The lifetimes of the middle atom cloud, which range from 0.43 ± 0.06 ms for $B_x = 52$ G up to 1.69 ± 0.11 ms for the triangular magnetic lattice and from 0.79 ± 0.07 ms for $B_x = 15$ G up to 2.5 ± 0.25 ms for the square magnetic lattice, are much longer than the corresponding lattice trap periods (1 - 3 μs). The trap lifetime increases almost linearly with increasing distance from the chip surface which ranges from as close as ~ 90 nm to ~ 330 nm.

Model calculations suggest that the trap lifetimes in the 0.7 μm-period magnetic

lattices are limited mainly by atom losses through one-dimensional thermal evaporation resulting from adiabatic heating as the atoms are transferred from the Z-wire magnetic trap with trapping frequency $\sim 200\,\mathrm{Hz}$ to the very tight magnetic lattice traps with trapping frequencies up to $\sim 800\,\mathrm{kHz}$. The calculations also indicate that for atom-surface distances greater than about 100 nm three-body recombination loss and fundamental atom-surface interactions such as Johnson magnetic noise and Casimir-Polder interactions do not contribute significantly to the short trap lifetimes.

The trapping of ultracold atoms in a sub-micron-period magnetic lattice at distances down to $\sim$ 90 nm from the chip surface and at trap frequencies up to $\sim$800 kHz represents new territory for trapping ultracold atoms. The observed trapping represents a significant step towards the long term goal of using magnetic lattices to simulate novel condensed matter phenomena such as newly predicted supersolidity characterized by co-existing crystalline and superfluid long-range order [120, 121], topologically non-trivial insulating states [122], and Mott insulating phases with fractional (1/3, 2/3) filling [123]. If the trap lifetimes can be lengthened, it should be possible to conduct the first quantum tunnelling experiments in a magnetic lattice. This would also provide us with important information on how close to the surface the arrays of atoms may be located and hence how small a lattice period can be used before decoherence due to surface effects such as the Casimir-Polder force become an issue. Such information is important in order to be able to perform quantum coherence experiments in sub-micron period magnetic lattices and it is also relevant to other atom chip applications such as chip-based miniature atomic clocks currently under development [124, 125].

6.2 Future directions

To overcome the limitation of short trap lifetimes in the sub-micron period magnetic lattices, it would be instructive to try to load the lattices with a BEC in the Z-wire trap. For a BEC, since all the atoms occupy the lowest energy state of the trap, it

is expected theoretically that no adiabatic heating occurs during the transfer of the atoms from the Z-wire magnetic trap with low trapping frequency to the tight sub-micron magnetic lattice traps with high trapping frequency. Also, in our experiment setup, it would be easier to be able to provide the appropriate bias magnetic fields required to obtain optimized square and triangular magnetic lattices as designed. In the case of the square magnetic lattice, for which the main bias field is along the x-direction (i.e., B_x), the bias field control is easier which would help us to study more about the behaviour of cold atoms very close to the chip surface.

In order to investigate further the origin of the short trap lifetimes, a new generation of magnetic lattice structures is planned with various lattice periods from 0.7 μm to 10 μm. The increase in the lattice period will reduce the trapping frequency of the lattice traps which should reduce the loss of atoms due to adiabatic heating during the transfer and increase the trap lifetime. Ideally, if the lifetime of the magnetic lattice trapped atoms can be increased to around a few hundred milliseconds with a lattice period around 1 μm, more important experiments could be performed such as RF spectroscopy of atoms trapped in the lattice and quantum tunnelling experiments.

It is also suggested to prepare a Z-wire magnetic trap with a high trapping frequency to reduce adiabatic heating as atoms are transferred into the lattice traps. Trapping frequencies of the order of kilohertz, as achieved by Jacqmin *et al*. [126] and Lin *et al*. [87], can help to reduce adiabatic heating by a factor of a few hundred. In our experiment setup, it should be possible to create a Z-wire trap with a higher trap frequency ($\sim$ 1 kHz) by using a thinner Z-wire to allow a smaller Z-wire trap. For this purpose, a new DBC (Direct Bonded Copper) atom chip has been designed and fabricated (Section 3.5).

Another possibility, which was suggested during a recent visit to our lab by Wolfgang Ketterle, is to load the magnetic lattice from a 1D optical lattice, for which the trapping frequencies could be as high as a few MHz [127]. A 1D optical lattice can be formed close to the magnetic lattice, for example, by shining a red-detuned laser beam at say 782 nm at nearly normal incidence to the gold reflecting surface

of the atom chip [128]. Atoms from a BEC in the Z-wire trap can then be loaded into several sites of the 1D optical lattice which extend from a few μm from the chip surface up to the magnetic lattice potential about 300 nm from the surface. In order for the atoms to remain trapped in the magnetic lattice, some energy dissipation in the conservative potentials can be provided by surface evaporative cooling.

Bibliography

[1] Maciej Lewenstein, Anna Sanpera, Veronica Ahufinger, Bogdan Damski, Aditi Sen, and Ujjwal Sen. Ultracold atomic gases in optical lattices: mimicking condensed matter physics and beyond. *Advances in Physics*, 56(2):243–379, 2007. (Cited on pages 1 and 5.)

[2] Steven Chu. Nobel lecture: The manipulation of neutral particles. *Reviews of Modern Physics*, 70(3):685, 1998. (Cited on page 1.)

[3] Claude N Cohen-Tannoudji. Nobel lecture: Manipulating atoms with photons. *Reviews of Modern Physics*, 70(3):707, 1998. (Cited on page 1.)

[4] William D. Phillips. Nobel lecture: Laser cooling and trapping of neutral atoms. *Rev. Mod. Phys.*, 70:721–741, 1998. (Cited on page 1.)

[5] M. Greiner, O. Mandel, T. Esslinger, T. W. Hänsch, and I. Bloch. Quantum phase transition from a superfluid to a Mott insulator in a gas of ultracold atoms. *Nature*, 415:39, 2002. (Cited on pages 1, 2, 3, 32, and 33.)

[6] Masao Takamoto, Feng-Lei Hong, Ryoichi Higashi, and Hidetoshi Katori. An optical lattice clock. *Nature*, 435(7040):321, 2005. (Cited on page 1.)

[7] Waseem S Bakr, Jonathon I Gillen, Amy Peng, Simon Fölling, and Markus Greiner. A quantum gas microscope for detecting single atoms in a Hubbard-regime optical lattice. *Nature*, 462(7269):74–77, 2009. (Cited on page 1.)

[8] T. Calarco, E. A. Hinds, D. Jaksch, J. Schmiedmayer, J. I. Cirac, and P. Zoller. Quantum gates with neutral atoms: Controlling collisional interactions in time-dependent traps. *Phys. Rev. A*, 61:022304, 2000. (Cited on page 2.)

[9] Chris Monroe. Quantum information processing with atoms and photons. *Nature*, 416(6877):238–246, 2002. (Cited on page 2.)

[10] F. S. Cataliotti, S. Burger, C. Fort, P. Maddaloni, F. Minardi, A. Trombettoni, A. Smerzi, and M. Inguscio. Josephson junction arrays with Bose-Einstein condensates. *Science*, 293:843, 2001. (Cited on page 2.)

[11] M Mancini, G Pagano, G Cappellini, L Livi, M Rider, J Catani, C Sias, P Zoller, M Inguscio, M Dalmonte, et al. Observation of chiral edge states with neutral fermions in synthetic Hall ribbons. *Science*, 349(6255):1510–1513, 2015. (Cited on page 2.)

[12] Juliette Billy, Vincent Josse, Zhanchun Zuo, Alain Bernard, Ben Hambrecht, Pierre Lugan, David Clément, Laurent Sanchez-Palencia, Philippe Bouyer, and Alain Aspect. Direct observation of Anderson localization of matter waves in a controlled disorder. *Nature*, 453(7197):891–894, 2008. (Cited on page 2.)

[13] Giacomo Roati, Chiara DErrico, Leonardo Fallani, Marco Fattori, Chiara Fort, Matteo Zaccanti, Giovanni Modugno, Michele Modugno, and Massimo Inguscio. Anderson localization of a non-interacting Bose-Einstein condensate. *Nature*, 453(7197):895–898, 2008. (Cited on page 2.)

[14] T. Kinoshita, T. Wenger and D. S. Weiss. A quantum Newton's cradle. *Nature*, 440:900–903, 2006. (Cited on page 2.)

[15] Kirill Martiyanov, Vasiliy Makhalov, and Andrey Turlapov. Observation of a two-dimensional Fermi gas of atoms. *Physical Review Letters*, 105(3):030404, 2010. (Cited on page 2.)

[16] Jonathan Simon, Waseem S Bakr, Ruichao Ma, M Eric Tai, Philipp M Preiss, and Markus Greiner. Quantum simulation of antiferromagnetic spin chains in an optical lattice. *Nature*, 472(7343):307–312, 2011. (Cited on page 2.)

[17] I. Herrera, Y. Wang, P. Michaux, D. Nissen, P. Surendran, S. Juodkazis, S. Whitlock, R. J. McLean, A. Sidorov, M Albrecht, and P. Hannaford. Sub-micron period lattice structures of magnetic microtraps for ultracold atoms on an atom chip. *J Phys D*, 48:115002, 2015. (Cited on pages 2, 5, 6, 23, 36, 41, 42, 43, 44, 45, 46, 47, and 50.)

[18] J. Yin, W. Gao, J. Hu, and Y. Wang. Magnetic surface microtraps for realizing an array of alkali atomic Bose-Einstein condensates or Bose clusters. *Opt Commun*, 206:99–113, 2002. (Cited on pages 2 and 3.)

[19] Axel Grabowski and Tilman Pfau. A lattice of magneto-optical and magnetic traps for cold atoms. *The European Physical Journal D-Atomic, Molecular, Optical and Plasma Physics*, 22(3):347–354, 2003. (Cited on page 2.)

[20] M. Yun and J. Yin. Practical scheme to realize 2D array of BECs on an atom chip: novel 2D magneto-optical and magnetic lattices. *Opt Express*, 14:2539–2551, 2006. (Cited on page 2.)

[21] R. Gerritsma and R. J. C. Spreeuw. Topological constraints on magnetostatic traps. *Phys. Rev. A*, 74:043405, 2006. (Cited on pages 2 and 28.)

[22] M. Singh, M. Volk, A. Akulshin, A. Sidorov, R. McLean, and P. Hannaford. One dimensional lattice of permanent magnetic microtraps for ultracold atoms on an atom chip. *J. Phys. B: At. Mol. Opt. Phys.*, 41:065301, 2008. (Cited on pages 2, 4, 5, 6, and 35.)

[23] E. A. Hinds and I. G. Hughes. Magnetic atom optics: mirrors, guides, traps, and chips for atoms. *J Phys D*, 32:R119–R146, 1999. (Cited on page 2.)

[24] S. Ghanbari, T. D. Kieu, and P. Hannaford. A class of permanent magnetic lattices for ultracold atoms. *J Phys B*, 40:1283–1294, 2007. (Cited on pages 2, 5, and 26.)

[25] R. Gerritsma, S. Whitlock, T. Fernholz, H. Schlatter, J. A. Luigjes, J.-U. Thiele, J. B. Goedkoop, and R. J. C. Spreeuw. Lattice of microtraps for ultracold atoms based on patterned magnetic films. *Phys. Rev. A*, 76:033408, 2007. (Cited on pages 2, 4, and 26.)

[26] S. Whitlock, R. Gerritsma, T. Fernholz, and R. J. C. Spreeuw. Two-dimensional array of microtraps with atomic shift register on a chip. *New J Phys*, 11:023021, 2009. (Cited on pages 2, 5, and 36.)

[27] Ahmed Abdelrahman, Mikhail Vasiliev, Kamal Alameh, and Peter Hannaford. Asymmetrical two-dimensional magnetic lattices for ultracold atoms. *Physical Review A*, 82(1):012320, 2010. (Cited on page 2.)

[28] R. Schmied, D. Leibfried, R. J. C. Spreeuw, and S. Whitlock. Optimized magnetic lattices for ultracold atomic ensembles. *New J Phys*, 12:103029, 2010. (Cited on pages 2, 5, 26, 28, 29, 30, 43, 48, and 115.)

[29] I Llorente García, B Darquié, E A Curtis, C D J Sinclair, and EA Hinds. Experiments on a videotape atom chip: fragmentation and transport studies. *New Journal of Physics*, 12(9):093017, 2010. (Cited on page 2.)

[30] V. Y. F. Leung, A. Tauschinsky, N. J. van Druten, and R. J. C. Spreeuw. Microtrap arrays on magnetic film atom chips for quantum information science. *Quant. Inf. Process*, 10:955–974, 2011. (Cited on pages 2 and 5.)

[31] Saeed Ghanbari, Ahmed Abdalrahman, Andrei Sidorov, and Peter Hannaford. Analysis of a simple square magnetic lattice for ultracold atoms. *Journal of Physics B: Atomic, Molecular and Optical Physics*, 47(11):115301, 2014. (Cited on pages 2 and 26.)

[32] S. Jose, P. Surendran, Y. Wang, I. Herrera, L. Krzemien, S. Whitlock, R. McLean, A. Sidorov, and P. Hannaford. Periodic array of Bose-Einstein condensates in a magnetic lattice. *Phys. Rev. A*, 89:051602(R), 2014. (Cited on pages 2, 5, 6, 35, and 48.)

[33] P. Surendran, S. Jose, Y. Wang, I. Herrera, H. Hu, X. Liu, S. Whitlock, R. McLean, A. Sidorov, and P. Hannaford. Radio-frequency spectroscopy of a linear array of Bose-Einstein condensates in a magnetic lattice. *Phys. Rev. A*, 91:023605, 2015. (Cited on pages 2, 5, 6, and 35.)

[34] V. Y. F. Leung, D. R. M. Pijn, H. Schlatter, L. Torralbo-Campo, A. L. La Rooij, G. B. Mulder, J. Naber, M. L. Soudijn, A. Tauschinsky, C. Abarbanel, B. Hadad, E. Golan, R. Folman, and R. J. C. Spreeuw. Magnetic-film atom chip with 10 μm period lattices of microtraps for quantum information science with Rydberg atoms. *Rev. Sci. Instrum.*, 85(5):053102, 2014. (Cited on pages 2 and 5.)

[35] Y Wang, T Tran, P Surendran, I Herrera, A Balcytis, D Nissen, M Albrecht, A Sidorov, and P Hannaford. Trapping ultracold atoms in a sub-micron-period triangular magnetic lattice. *Physical Review A*, 96(1):013630, 2017. (Cited on pages 2, 6, 86, and 106.)

[36] O. Romero-Isart, C. Navau, A. Sanchez, P. Zoller, and J. I. Cirac. Superconducting vortex lattices for ultracold atoms. *Phys. Rev. Lett*, 111:145304, 2013. (Cited on page 2.)

[37] X. Luo, L. Wu, J. Chen, R. Lu, R. Wang, and L. You. Generating an effective magnetic lattice for ultracold atoms. *New J Phys*, 17:083048, 2015. (Cited on page 2.)

[38] J. Yu, Z. Xu, R. Lü, and L. You. Dynamical generation of topological magnetic lattices for ultracold atoms. *Phys. Rev. Lett*, 116:143003, 2016. (Cited on page 2.)

[39] Adam D West, Kevin J Weatherill, Thomas J Hayward, Paul W Fry, Thomas Schrefl, Mike R J Gibbs, Charles S Adams, Dan A Allwood, and Ifan G Hughes. Realization of the manipulation of ultracold atoms with a reconfigurable nanomagnetic system of domain walls. *Nano Letters*, 12(8):4065–4069, 2012. (Cited on page 2.)

[40] R A Pepino, J Cooper, D Meiser, D Z Anderson, and M J Holland. Open quantum systems approach to atomtronics. *Physical Review A*, 82(1):013640, 2010. (Cited on page 2.)

[41] S. Ghanbari, P. B. Blakie, P. Hannaford, and T. D. Kieu. Superfluid to Mott insulator quantum phase transition in a 2D permanent magnetic lattice. *The European Physical Journal B*, 70:305–310, 2009. (Cited on pages 3 and 34.)

[42] Alan L Migdall, John V Prodan, William D Phillips, Thomas H Bergeman, and Harold J Metcalf. First observation of magnetically trapped neutral atoms. *Physical Review Letters*, 54(24):2596, 1985. (Cited on pages 3 and 13.)

[43] R V E Lovelace, C Mehanian, T J Tommila, and D M Lee. Magnetic confinement of a neutral gas. *Nature*, 318(6041):30–36, 1985. (Cited on page 3.)

[44] G. I. Opat, S. J. Wark, and A. Cimmino. Electric and magnetic mirrors and gratings for slowly moving neutral atoms and molecules. *Appl. Phys. B*, 54:396–402, 1992. (Cited on page 3.)

[45] T. M. Roach, H. Abele, M. G. Boshier, H. L. Grossman, K. P. Zetie, and E. A. Hinds. Realization of a magnetic mirror for cold atoms. *Phys. Rev. Lett.*, 75:629–632, 1995. (Cited on page 3.)

[46] A. I. Sidorov, R. J. McLean, W. J. Rowlands, D. C. Lau, J. E. Murphy, M. Walkiewicz, G. I. Opat, and P. Hannaford. Specular reflection of cold caesium atoms from a magnetostatic mirror. *Quantum Semiclass. Opt.*, 8:713–725, 1996. (Cited on page 3.)

[47] A. I. Sidorov, D. C. Lau, G. I. Opat R. J. McLean, W. J. Rowlands, and P. Hannaford. Magnetostatic optical elements for laser-cooled atoms. *Laser Physics.*, 8:642–648, 1998. (Cited on page 3.)

[48] D. C. Lau, R. J. McLean, A. I. Sidorov, D. S. Gough, J. Koperski, W. J. Rowlands, B. A. Sexton, G. I. Opat and P. Hannaford. Magnetic mirrors with micron scale periodicities for slowly moving neutral atoms. *J. Phys. B: Quantum Semiclass. Opt.*, 1:371–377, 1999. (Cited on page 3.)

[49] A. Grabowski and T. Pfau. A lattice of magneto-optical and magnetic traps for cold atoms. *Eur. Phys. J. D*, 22:347354, 2003. (Cited on page 4.)

[50] Saeed Ghanbari, Tien D Kieu, Andrei Sidorov, and Peter Hannaford. Permanent magnetic lattices for ultracold atoms and quantum degenerate gases. *Journal of Physics B: Atomic, Molecular and Optical Physics*, 39(4):847, 2006. (Cited on pages 4 and 5.)

[51] Min Yun and Jianping Yin. Practical scheme to realize 2D array of BECs on an atom chip: novel 2D magneto-optical and magnetic lattices. *Opt. Express*, 14:2539–2551, 2006. (Cited on page 4.)

[52] C. D. J. Sinclair, E. A. Curtis, I. Llorente Garcia, J. A. Retter, B. V. Hall, S. Eriksson, B. E. Sauer, and E. A. Hinds. Bose-Einstein condensation on a permanent-magnet atom chip. *Phys. Rev. A*, 72:031603(R), 2005. (Cited on page 4.)

[53] M. Boyd, E. W. Streed, P. Medley, G. K. Campbell, J. Mun, W. Ketterle, and D. E. Pritchard. Atom trapping with a thin magnetic film. *Phys. Rev. A*, 76:043624, 2007. (Cited on page 4.)

[54] M. Singh, R. McLean, A. Sidorov, and P. Hannaford. Dynamics of reflection of ultracold atoms from a periodic one-dimensional magnetic lattice potential. *Phys. Rev. A*, 79:053407, 2009. (Cited on pages 4, 84, and 88.)

[55] Mandip Singh and Peter Hannaford. Effect of projection velocity and temperature on the reflection of ultracold atoms from a periodic one-dimensional corrugated magnetic potential. *Physical Review A*, 82(1):013416, 2010. (Cited on page 4.)

[56] E. A. Burt, R. W. Ghrist, C. J. Myatt, M. J. Holland, E. A. Cornell, and C. E. Wieman. Coherence, correlations, and collisions: What one learns about Bose-Einstein condensates from their decay. *Phys. Rev. Lett.*, 79:337, 1997. (Cited on pages 5, 25, 71, and 104.)

[57] J. Söding, D. Guéry-Odelin, P. Desbiolles, F. Chevy, H. Inamori, and J. Dalibard. Three-body decay of a rubidium Bose-Einstein condensate. *Appl. Phys. B*, 69:257, 1999. (Cited on pages 5, 25, and 71.)

[58] M. Singh. A magnetic lattice and macroscopic entanglement of a BEC on an atom chip. *Swinburne PhD thesis*, 2008. (Cited on pages 6, 55, 58, 84, and 88.)

[59] S. Jose. Trapping of ultracold atoms in a magnetic lattice. *Swinburne PhD thesis*, 2013. (Cited on pages 6 and 55.)

[60] P. Surendran. Bose-Einstein condensation in a magnetic lattice. *Swinburne PhD thesis*, 2015. (Cited on pages 6, 55, and 67.)

[61] Y. Wang. Sub-micron-period magnetic lattices for ultracold atoms. *Swinburne PhD thesis*, 2017. (Cited on pages 6, 55, 75, 81, 85, and 91.)

[62] S. Chu, L. Hollberg, J. E. Bjorkholm, A. Cable, and A. Ashkin. Three-dimensional viscous confinement and cooling of atoms by resonance radiation pressure. *Phys. Rev. Lett.*, 55:48, 1985. (Cited on page 10.)

[63] C. J. Pethick and H. Smith. Bose Einstein Condensition in dilute gases. *Cambrigde University Press*, 2002. (Cited on pages 10, 16, 24, and 25.)

[64] E. Majorana. Atomi orientati in campo magnetico variabile. *Nuovo Cimento*, 9:43, 1932. (Cited on page 10.)

[65] David E Pritchard. Cooling neutral atoms in a magnetic trap for precision spectroscopy. *Physical Review Letters*, 51(15):1336, 1983. (Cited on page 11.)

[66] C V Sukumar and DM Brink. Spin-flip transitions in a magnetic trap. *Physical Review A*, 56(3):2451, 1997. (Cited on page 11.)

[67] J. Reichel. Microchip traps and Bose-Einstein condensation. *Appl. Phys. B*, 75:469, 2002. (Cited on page 12.)

[68] József Fortágh and Claus Zimmermann. Magnetic microtraps for ultracold atoms. *Reviews of Modern Physics*, 79(1):235, 2007. (Cited on page 12.)

[69] R. Folman, P. Krüger, J. Schmiedmayer, J. Denschlag, and C. Henkel. Microscopic atom optics: From wires to an atom chip. *Advances in Atomic, Molecular, and Optical Physics*, 48:263–356, 2002. (Cited on page 12.)

[70] T Bergeman, Gidon Erez, and Harold J Metcalf. Magnetostatic trapping fields for neutral atoms. *Physical Review A*, 35(4):1535, 1987. (Cited on page 13.)

[71] J. Reichel, W. Hänsel, and T. W. Hänsch. Atomic micromanipulation with magnetic surface traps. *Phys. Rev. Lett.*, 83:3398, 1999. (Cited on page 13.)

[72] R. Folman, P. Krüger, D. Cassettari, B. Hessmo, T. Maier, and J. Schmiedmayer. Controlling cold atoms using nanofabricated surfaces: Atom chips. *Phys. Rev. Lett.*, 84:4749, 2000. (Cited on page 13.)

[73] http://www.esrf.eu/Accelerators/Groups/InsertionDevices/Software/Radia. (Cited on page 14.)

[74] Kerson Huang. Statistical mechanics, 2nd. *Edition (New York: John Wiley & Sons)*, 1987. (Cited on page 15.)

[75] F Dalfovo, L Pitaevskii, and S Stringari. The condensate wave function of a trapped atomic gas. *Journal of Research of the National Institute of Standards and Technology*, 101(4):537, 1996. (Cited on page 16.)

[76] Fabrice Gerbier, Joseph H Thywissen, Simon Richard, Mathilde Hugbart, Philippe Bouyer, and Alain Aspect. Experimental study of the thermodynamics of an interacting trapped Bose-Einstein condensed gas. *Physical Review A*, 70(1):013607, 2004. (Cited on page 17.)

[77] P. Treutlein. Coherent manipulation of ultracold atoms on atom chips. *PhD thesis*, Ludwig-Maximilians Universität München, 2008. (Cited on pages 17, 18, 20, 22, and 105.)

[78] J. Fortágh and C. Zimmermann. Magnetic microtraps for ultracold atoms. *Rev. Mod. Phys.*, 79:235, 2007. (Cited on page 17.)

[79] D. M. Harber, H. J. Lewandowski, J. M. McGuirk, and Eric A. Cornell. Effect of cold collisions on spin coherence and resonance shifts in a magnetically trapped ultracold gas. *Physical Review A*, 66(5):053616, 2002. (Cited on page 17.)

[80] Carsten Henkel. The physics of atom-surface interactions. *arXiv preprint physics/0405084*, 2004. (Cited on page 17.)

[81] Carsten Henkel. Exploring surface interactions with atom chips. *arXiv preprint quant-ph/0512043*, 2005. (Cited on page 17.)

[82] P. Treutlein, P. Hommelhoff, T. Steinmetz, T. W. Hänsch, and J. Reichel. Coherence in microchip traps. *Phys. Rev. Lett.*, 92:203005, 2005. (Cited on page 17.)

[83] Stefan Scheel, Per-Kristian Rekdal, Peter L Knight, and Edward A Hinds. Atomic spin decoherence near conducting and superconducting films. *Physical Review A*, 72(4):042901, 2005. (Cited on page 19.)

[84] Bo-Sture K. Skagerstam, Ulrich Hohenester, Asier Eiguren, and Per Kristian Rekdal. Spin decoherence in superconducting atom chips. *Physical Review Letters*, 97(7):070401, 2006. (Cited on page 19.)

[85] D. Meschede, W. Jhe, and E. A. Hinds. Radiative properties of atoms near a conducting plane: An old problem in a new light. *Physical Review A*, 41(3):1587, 1990. (Cited on page 20.)

[86] T. A. Pasquini, Y. Shin, C. Sanner, M. Saba, A. Schirotzek, D. E. Pritchard, and W. Ketterle. Quantum reflection from a solid surface at normal incidence. *Phys. Rev. Lett.*, 93:223201, 2004. (Cited on pages 20 and 92.)

[87] Yu-ju Lin, Igor Teper, Cheng Chin, and Vladan Vuletić. Impact of the Casimir-Polder potential and Johnson noise on Bose-Einstein condensate stability near surfaces. *Physical Review Letters*, 92(5):050404, 2004. (Cited on pages 20, 22, 92, 103, and 118.)

[88] Z. Yan, A. Dalgarno, and J. F. Babb. Long-range interactions of lithium atoms. *Phys. Rev. A.*, 55:2882, 1997. (Cited on page 20.)

[89] C. Henkel, S. Pötting, and M. Wilkens. Loss and heating of particles in small and noisy traps. *Appl. Phys. B*, 69:379, 1999. (Cited on page 22.)

[90] C. Henkel, P. Krüger, R. Folman, and J. Schmiedmayer. Fundamental limits for coherent manipulation on atom chips. *Appl. Phys.B*, 76:173, 2003. (Cited on page 22.)

[91] M. P. A. Jones, C. J. Vale, D. Sahagun, B. V. Hall, and E. A. Hinds. Spin coupling between cold atoms and the thermal fluctuations of a metal surface. *Phys. Rev. Lett.*, 91:080401, 2003. (Cited on page 22.)

[92] D. M. Harber, J. M. McGuirk, J. M. Obrecht, and E. A. Cornell. Thermally induced losses in ultra-cold atoms magnetically trapped near room-temperature surfaces. *J. Low Temp. Phys.*, 133:229, 2003. (Cited on pages 22 and 93.)

[93] Carsten Henkel. Magnetostatic field noise near metallic surfaces. *The European Physical Journal D-Atomic, Molecular, Optical and Plasma Physics*, 35(1):59–67, 2005. (Cited on pages 22 and 105.)

[94] C. Henkel. Magnetostatic field noise near metallic surfaces. *Eur. Phys. J. D*, 35:59, 2005. (Cited on page 22.)

[95] J. M. Obrecht, R. J. Wild, and E. A. Cornell. Measuring electric fields from surface contaminants with neutral atoms. *Phys. Rev. A*, 75:062903, 2007. (Cited on page 23.)

[96] J. M. McGuirk, D. M. Harber, J. M. Obrecht, and E. A. Cornell. Alkali-metal adsorbate polarization on conducting and insulating surfaces probed with Bose-Einstein condensates. *Phys. Rev. A*, 69:062905, Jun 2004. (Cited on page 23.)

[97] Paul S. Julienne, F. H. Mies, Eite Tiesinga, and Carl J. Williams. Collisional stability of double Bose condensates. *Physical Review Letters*, 78(10):1880, 1997. (Cited on page 25.)

[98] E. Tiesinga, B. J. Verhaar, and H. T. C. Stoof. Threshold and resonance phenomena in ultracold ground-state collisions. *Physical Review A*, 47(5):4114, 1993. (Cited on page 25.)

[99] D. Jaksch, C. Bruder, J. I. Cirac, C. W. Gardiner, and P. Zoller. Cold bosonic atoms in optical lattices. *Phys. Rev. Lett.*, 81:3108, 1998. (Cited on pages 31 and 32.)

[100] M. P. A. Fisher, P. B. Weichman, G. Grinstein, and D. S. Fisher. Boson localization and the superfluid-insulator transition. *Phys. Rev. B*, 40:546, 1989. (Cited on page 32.)

[101] I. B. Spielman, W. D. Phillips, and J. V. Porto. Mott-insulator transition in a two-dimensional atomic bose gas. *Phys. Rev. Lett.*, 98:080404, 2007. (Cited on page 33.)

[102] I. Bloch, J. Dalibard, and W. Zwerger. Many-body physics with ultracold gases. *Rev. Mod. Phys.*, 80:885, 2008. (Cited on pages 34 and 36.)

[103] G. G. Batrouni, V. Rousseau, R. T. Scalettar, M. Rigol, A. Muramatsu, P. J. H. Denteneer, and M. Troyer. Mott domains of bosons confined on optical lattices. *Phys. Rev. Lett.*, 89:117203, 2002. (Cited on page 34.)

[104] Ruquan Wang. Approaching lithium BEC with a mini trap. *Yale University PhD Thesis*, 2006. (Cited on page 37.)

[105] M. B. Squires, J. A. Stickney, E. J. Carlson, P. M. Baker, W. R. Buchwald, S. Wentzell, and S. M. Miller. Atom chips on direct bonded copper substrates. *Rev. Sci. Instrum.*, 82:023101, 2011. (Cited on page 37.)

[106] S Groth, P Krüger, S Wildermuth, R Folman, T Fernholz, J Schmiedmayer, D Mahalu, and I Bar-Joseph. Atom chips: Fabrication and thermal properties. *Applied Physics Letters*, 85(14):2980–2982, 2004. (Cited on page 39.)

[107] I. G. Hughes, P. A. Barton, T. M. Roach, and E. A. Hinds. Atom optics with magnetic surfaces: II. microscopic analysis of the floppy disk mirror. *J. Phys. B: At. Mol. Opt. Phys.*, 30:2119, 1997. (Cited on page 42.)

[108] D. G. Stinson and S.-C. Shin. Magnetization and anisotropy of Co/Pd multilayer thin films. *J. Appl. Phys.*, 67:4459, 1990. (Cited on page 45.)

[109] http://remtec.com/. (Cited on page 52.)

[110] C. P. Pearman, C. S. Adams, S. G. Cox, P. F. Griffin, D. A. Smith, and I. G. Hughes. Polarization spectroscopy of a closed atomic transition: applications to laser frequency locking. *J. Phys. B: At. Mol. Phys.*, 35:5141, 2002. (Cited on page 58.)

[111] C. Wieman and T. W. Hänsch. Doppler-free laser polarization spectroscopy. *Phys. Rev. Lett.*, 36:1170, 1976. (Cited on page 58.)

[112] O. J. Luiten, M. W. Reynolds, and J. T. M. Walraven. Kinetic theory of the evaporative cooling of a trapped gas. *Phys. Rev. A*, 53:381, 1996. (Cited on page 72.)

[113] Wolfgang Ketterle and N.J. Van Druten. Evaporative cooling of trapped atoms. *Advances in Atomic, Molecular, and Optical Physics*, 37:181236, 1996. (Cited on page 73.)

[114] D. S. Jin, J. R. Ensher, M. R. Matthews, C. E. Wieman, and E. A. Cornell. Collective excitations of a Bose-Einstein condensate in a dilute gas. *Phys. Rev. Lett.*, 77:420, 1996. (Cited on page 75.)

[115] Y. Castin and R. Dum. Bose-Einstein condensates in time dependent traps. *Phys. Rev. Lett.*, 77:5315, 1996. (Cited on page 77.)

[116] D. A. Smith, S. Aigner, S. Hofferberth, M. Gring, M. Andersson, S. Wildermuth, P. Krüger, S. Schneider, T. Schumm, and J. Schmiedmayer. Absorption imaging of ultracold atoms on atom chips. *Opt. Express*, 19(9):8471–8485, 2011. (Cited on page 82.)

[117] E. L. Surkov, J. T. M. Walraven, and G. V. Shlyapnikov. Collisionless motion and evaporative cooling of atoms in magnetic traps. *Phys. Rev. A*, 53:3403, 1996. (Cited on page 92.)

[118] J. Märkle, A. J. Allen, P. Federsel, B. Jetter, A. Günther, J. Fortágh, N. P. Proukakis, and T. E. Judd. Evaporative cooling of cold atoms at surfaces. *Phys. Rev. A*, 90:023614, Aug 2014. (Cited on page 93.)

[119] Christian Stehle, Helmar Bender, Claus Zimmermann, Dieter Kern, Monika Fleischer, and Sebastian Slama. Plasmonically tailored micropotentials for ultracold atoms. *Nature Photonics*, 5(8):494–498, 2011. (Cited on page 106.)

[120] Stefan Wessel and Matthias Troyer. Supersolid hard-core bosons on the triangular lattice. *Phys. Rev. Lett.*, 95:127205, 2005. (Cited on page 117.)

[121] R. G. Melko, A. Paramekanti, A. A. Burkov, A. Vishwanath, D. N. Sheng, and L. Balents. Supersolid order from disorder: Hard-core bosons on the triangular lattice. *Phys. Rev. Lett.*, 95:127207, 2005. (Cited on page 117.)

[122] Tudor D. Stanescu, Victor Galitski, and S. Das Sarma. Topological states in two-dimensional optical lattices. *Phys. Rev. A*, 82:013608, Jul 2010. (Cited on page 117.)

[123] L. Santos, M. A. Baranov, J. I. Cirac, H.-U. Everts, H. Fehrmann, and M. Lewenstein. Atomic quantum gases in kagomé lattices. *Phys. Rev. Lett.*, 93:030601, Jul 2004. (Cited on page 117.)

[124] P Rosenbusch. Magnetically trapped atoms for compact atomic clocks. *Applied Physics B: Lasers and Optics*, 95(2):227–235, 2009. (Cited on page 117.)

[125] R. Szmuk, V. Dugrain, W. Maineult, J. Reichel, and P. Rosenbusch. Stability of a trapped-atom clock on a chip. *Phys. Rev. A*, 92:012106, 2015. (Cited on page 117.)

[126] T. Jacqmin, B. Fang, T. Berrada, T. Roscilde, and I. Bouchoule. Momentum distribution of one-dimensional Bose gases at the quasi-condensation crossover: Theoretical and experimental investigation. *Phys. Rev. A.*, 86:043626, 2012. (Cited on page 118.)

[127] S. Blatt, A. Mazurenko, M. F. Parsons, C. S. Chiu, F. Huber, and M. Greiner. Low-noise optical lattices for ultracold ^{6}Li. *Phys. Rev. A*, 92:021402, Aug 2015. (Cited on page 118.)

[128] D Gallego, S Hofferberth, Thorsten Schumm, Peter Krüger, and Jörg Schmiedmayer. Optical lattice on an atom chip. *Optics letters*, 34(22):3463–3465, 2009. (Cited on page 119.)

Publications

1. *Ultracold atoms in magnetic lattices*
T. Tran, Y. Wang and P. Hannaford
In preparation

2. *Trapping ultracold atoms in a sub-micron-period triangular magnetic lattice*
Y. Wang, T. Tran, P. Surendran, I. Herrera, A. Balcytis, D. Nissen, M. Albrecht, A. Sidorov and P. Hannaford
Physical Review A **96**, 013630 (2017)

3. *Magnetic lattices for ultracold atoms and degenerate quantum gases*
Y. Wang, P. Surendran, S. Jose, T. Tran, I. Herrera, S. Whitlock, R. McLean, A. Sidorov, and P. Hannaford
Science Bulletin **61**, 1097-1106 (2016)